GEORG-AUGUST-UNIVERSITÄT GÖTTINGEN

UNIVERSITÄTSMEDIZIN GÖTTINGEN UMG

Melanoma-associated brain metastasis: molecular mechanisms and therapeutic options

Dissertation

for the award of the degree

"Doctor rerum naturalium"

of the Georg-August-Universität Göttingen

within the doctoral program *Molecular Medicine*

of the Georg-August University School of Science (GAUSS)

submitted by

Ioana Todoran, née Stejerean

born in Bistrița, Romania

Göttingen, 2022

Thesis Committee

Prof. Dr. Ivan Bogeski
Molecular Physiology
Institute of Cardiovascular Physiology
University Medical Center Göttingen

Prof. Dr. Dieter Kube
Dept. of Hematology and Oncology
University Medical Center Göttingen

Prof. Dr. Jörg Wilting
Dept. of Anatomy and Cell Biology
University Medical Center Göttingen

Members of the Examination Board

Referee: Prof. Dr. Ivan Bogeski
Molecular Physiology
Institute of Cardiovascular Physiology
University Medical Center Göttingen

2nd Referee: Prof. Dr. Dieter Kube
Dept. of Hematology and Oncology
University Medical Center Göttingen

Extended Members of the Examination Board

Prof. Dr. Jörg Wilting
Dept. of Anatomy and Cell Biology
University Medical Center Göttingen

Prof. Dr. Frauke Alves
Translational Molecular Imaging
Max Planck Institute of Experimental Medicine
&
Institute of Diagnostic and Interventional Radiology
Clinic of Hematology and Medical Oncology
University Medical Center Göttingen

Prof. Dr. Volker Ellenrieder
Department of Gastroenterology, Gastrointestinal Oncology and Endocrinology
University Medical Center Göttingen

Prof. Dr. Michael Peter Schön
Department of Dermatology, Venereology and Allergology
University Medical Center Göttingen

Date of oral examination: March 31st, 2022

Supervisors:

Prof. Dr. med. Ivan Bogeski

Adina Vultur, Ph.D.

In the memory of my beloved grandparents

To my husband and my parents

TABLE OF CONTENTS

Selected publications
(manuscripts under revision or published during the doctoral studies)

The data presented in this doctoral thesis were submitted as an original research article before the thesis submission date:

Stejerean-Todoran I, Gimotty PA, Watters A, Brafford P, Krepler C, Godok T, Li H, Bonilla del Rio Z, Zieseniss A, Katschinski DM, Sertel SM, Rizzoli SO, Garman B, Nathanson KL, Lotem M, Mills GB, Davies MA, Schön MP, Bogeski I, Herlyn M and Vultur A. ***A distinct pattern of growth and RAC1 signaling in melanoma brain metastasis*** (under revision for publication at *Neuro Oncol.*).

Additional manuscripts / publications:

Zimmermann K, Stejerean-Todoran I, Vultur A, Gibhardt CS, Ickes C, Shannan B, Bonilla del Río Z, Cappello S, Sung HM, Shumanska M, Zhang X, Wölling A, Nanadikar MS, Watters A, Brafford P, Wilting J, Urlaub H, Katschinski DM, Rehling P, Lenz C, Roesch A, Schön MP, Herlyn M, Stanisz H and Bogeski I. ***MCU controls melanoma progression through a redox-controlled phenotype switch*** (under revision for publication at *EMBO Rep.*).

Zhang X, Gibhardt CS, Will T, Stanisz H, Körbel C, Mitkovski M, Stejerean I, Cappello S, Pacheu-Grau D, Dudek J, Tahbaz N, Mina L, Simmen T, Laschke MW, Menger MD, Schön MP, Helms V, Niemeyer BA, Rehling P, Vultur A, Bogeski I. ***Redox signals at the ER-mitochondria interface control melanoma progression.*** *EMBO J.* 2019; **38**(15): e100871.

Cappello S, Sung HM, Ickes C, Gibhardt CS, Vultur A, Bhat H, Hu Z, Brafford P, Denger A, Stejerean-Todoran I, Köhn RM, Lorenz V, Künzel N, Salinas G, Stanisz H, Legler T, Rehling P, Schön MP, Lang KS, Helms V, Herlyn M, Hoth M, Kummerow C, Bogeski I. ***Protein Signatures of NK Cell-Mediated Melanoma Killing Predict Response to Immunotherapies.*** *Cancer Res.* 2021; **81**(21): 5540-5554.

Gibhardt CS, Cappello S, Bhardwaj R, Schober R, Kirsch SA, Bonilla Del Rio Z, Gahbauer S, Bochicchio A, Sumanska M, Ickes C, Stejerean-Todoran I, Mitkovski M, Alansary D, Zhang X, Revazian A, Fahrner M, Lunz V, Frischauf I, Luo T, Ezerina D, Messens J, Belousov VV, Hoth M, Böckmann RA, Hediger MA, Schindl R and Bogeski I. ***Oxidative Stress-Induced STIM2 Cysteine Modifications Suppress Store-Operated Calcium Entry.*** *Cell Rep.* 2020; **33**(3): 108292.

Latif MU, Schmidt GE, Mercan S, Rehman R, Gibhardt CS, Stejerean-Todoran I, Reutlinger K, Hessmann E, Singh SK, Moeed A, Rehman A, Butt UJ, Stroebel P, Bremer S, Neesse A, Bogeski I and Ellenrieder V. ***NFATc1 signaling drives chronic ER stress responses to promote NAFLD progression***. *Gut.* 2022; gutjnl-2021-325013.

Poschmann G, Bahr J, Schrader J, Stejerean-Todoran I, Bogeski I and Stühler K. ***Secretomics—A Key to a Comprehensive Picture of Unconventional Protein Secretion.*** *Front Cell Dev Biol.* 2022; **10**: 878027

ABBREVIATIONS

2D	two-dimensional
3D	three-dimensional
4E-BP1	eukaryotic translation initiation factor 4E-binding protein 1
53BP1	tumor suppressor p53 binding protein 1
ABL	tyrosine-protein kinase
ADP	adenosine diphosphate
AKT	protein kinase B or PKB
APS	ammonium persulfate
AR	androgen receptor
Arf	ADP ribosylation factors
ATM	serine/threonine kinase
ATP	adenosine triphosphate
BBB	blood-brain barrier
BC	before Christ
BCA	bicinchoninic acid
BM	brain metastasis
BRAF	RAF kinase, isoform B
BSA	bovine serum albumin
BSO	buthionine sulfoximine
BTB	blood-tumor barrier
C	cytosine
$CaCl_2$	calcium chloride
calcein-AM	calcein-acetoxymethyl
CDC	cell division control protein
CDK	cyclin-dependent kinase
CDKN2A	cyclin-dependent kinase inhibitor 2A
cDNA	complementary DNA
CHK	checkpoint kinase
CNS	central nervous system
CO_2	carbon dioxide
CT	cycle threshold
CTL	cytotoxic T-cell
CTLA-4	cytotoxic T-lymphocyte-associated protein 4

DAPI	4′,6-diamidino-2-phenylindole
DCs	dendritic cells
ddH_2O	double-distilled water
DEPTOR	DEP domain-containing mTOR-interacting protein
DIV	days *in vitro*
DMEM	Dulbecco's Modified Eagle Medium
DMSO	dimethyl sulfoxide
DNA	deoxyribonucleic acid
dNTP	deoxyribonucleotide triphosphate
DPBS	Dulbecco's Phosphate-Buffered Saline
dT	deoxythymine
DTT	dithiothreitol
DUOX	dual oxidase
EDTA	ethylenediaminetetraacetic acid
EGTA	ethylene glycol-bis(β-aminoethyl ether)-N,N,N′,N′-tetraacetic acid
EGFR	epidermal growth factor receptor
Em	emission
EMEM	Eagle's Minimal Essential Medium
ERK	extracellular signal-regulated kinase
EthD-1	ethidium homodimer-1
Ex	excitation
FAK	focal adhesion kinase
FCS	fetal calf serum
FDA	Food and Drug Administration
GAP	GTPase-activating protein
GAPDH	glyceraldehyde-3-phosphate dehydrogenase
G-CSF	granulocyte colony-stimulating factor
GDP	guanosine diphosphate
GEF	guanine nucleotide exchange factors
GM-CSF	granulocyte-macrophage colony-stimulating factor
GST-RBD	glutathione-S-transferase-RHO binding domain of RHOtekin
GTP	guanosine triphosphate
H_2O	water
H_2O_2	hydrogen peroxide
H_3PO_4	phosphoric acid

HACM	human astrocyte conditioned medium
HBSS	Hank's Balanced Salt Solution
HCl	hydrochloric acid
HEK cells	human embryonic kidney cells
HEPES	4-(2-hydroxyethyl)-1-piperazineethanesulfonic acid
HSP	heat shock protein
IC50	half maximal inhibitory concentration
IF	immunofluorescence
IGF-1	insulin-like growth factor 1
IκB	NF-κB inhibitor
IL	interleukin
JNK	c-Jun N-terminal kinase
K	lysine
KCl	potassium chloride
KD	knockdown
KH_2PO_4	monopotassium phosphate
L	leucine
LB medium	Lysogeny Broth medium
MAP2K1	dual specificity mitogen-activated protein kinase kinase 1
MAPK	mitogen-activated protein kinase
MBM	melanoma brain metastasis
MC1R	melanocortin receptor 1
MDSC	myeloid-derived suppressor cell
MEK	mitogen-activated protein kinase kinase
$MgCl_2$	magnesium chloride
MHC	major histocompatibility complex
mLST8	mammalian lethal with SEC13 protein 8
mRNA	messenger RNA
MSH	melanocyte stimulating hormone
mSIN1	mammalian stress-activated protein kinase-interacting protein
mTEMPO	mitoTEMPO, mitochondria-targeted antioxidant
mTOR	mechanistic/mammalian target of rapamycin
mTORC1	mTOR complex 1
mTORC2	mTOR complex 2
Na_2HPO_4	disodium phosphate

Na_3VO_4	sodium orthovanadate
NAC	N-acetylcysteine
NaCl	sodium chloride
NADPH	nicotinamide adenine dinucleotide phosphate
NaF	sodium fluoride
$NaHCO_3$	sodium bicarbonate
NaOH	sodium hydroxide
NF1	neurofibromin 1
NF-κB	nuclear factor kappa-light-chain-enhancer of activated B cells
NH_4Cl	ammonium chloride
NK cells	natural killer cells
NOX	NADPH oxidase
NOXA1	NADPH oxidase activator 1
NP-40	Nonidet® P40
NRAS	RAS protein, isoform N
NSG	NOD scid gamma (mouse)
OXPHOS	oxidative phosphorylation
p70S6K	p70S6 kinase or ribosomal protein S6 kinase beta-1
PAK1	p21-activated kinase
PAR	poly (ADP-ribose) polymer
PARP	poly (ADP-ribose) polymerase
PBS	phosphate-buffered saline
PD-1	programmed cell death protein 1
PDK1	phosphoinositide-dependent kinase-1
PD-L1	programmed death-ligand 1
PDX	patient-derived xenograft
PFA	paraformaldehyde
pH	power of hydrogen
phox	phagocyte oxidase
PI3K	phosphoinositide 3-kinases
PIP_2	phosphatidylinositol-4,4-bisphosphate
PIP_3	phosphatidylinositol-3,4,5-trisphosphate
PLC	phosphatidylinositol-4,5-bisphosphate phosphodiesterase
PMSF	phenylmethylsulfonyl fluoride
PRAS40	proline-rich AKT1 substrate 1

PREX	phosphatidylinositol 3,4,5-trisphosphate-dependent RAC exchanger protein
PROTOR	protein observed with RICTOR
PTEN	phosphatase and tensin homolog
Q	glutamine
R	arginine
RT-qPCR	quantitative real-time polymerase chain reaction
RAB	RAS-related in brain protein
RAC	RAS-related C3 botulinum toxin substrate
RAF	rapidly accelerated fibrosarcoma kinase
RAN	RAS-related nuclear protein
RAS	Rat sarcoma protein
RGP	radial growth phase
Rho	RAS homologous protein
RhoA	RAS homolog family member A
RICTOR	rapamycin-insensitive companion of mammalian target of rapamycin
RIPA buffer	radioimmunoprecipitation assay buffer
RNA	ribonucleic acid
ROS	reactive oxygen species
RPPA	reverse phase protein array
RPTOR	regulatory associated protein of mTOR
RSL3	RAS synthetic lethal 3
RTK	receptor tyrosine kinase
S6	ribosomal protein S6 kinase
s.c.	subcutaneous (injection)
SDS	sodium dodecyl sulfate
SDS-PAGE	sodium dodecyl sulfate polyacrylamide gel electrophoresis
SEM	standard error of the mean
shRNA	short/small hairpin RNA
SRC	proto-oncogene tyrosine-protein kinase
SRS	stereotactic radiosurgery
STAT3	signal transducer and activator of transcription 3
T	thymine
TAM	tumor-associated macrophage
TBP	TATA-binding protein

TBS	tris-buffered saline
TEMED	tetramethylethylenediamine
TERT	telomerase reverse transcriptase
TGF-β	transforming growth factor beta
TGH buffer	buffer based on Triton X-100, glycerol and HEPES
TIAM1	T-cell lymphoma invasion and metastasis-inducing protein 1
TME	tumor microenvironment
TP53	tumor protein p53
Treg	regulatory T-cells
TRIO	triple functional domain protein
T-VEC	talimogene laherparepvec.
UV	ultraviolet
V	valine
VAV2	guanine nucleotide exchange factor VAV2
VEGF	vascular endothelial growth factor
VGP	vertical growth phase
WBRT	whole-brain radiotherapy
WB	western blot

Units

° C	degree Celsius
A	Ampere
rpm	rounds per minute
g	gram
h	hour
l	liter
m	meter
min	minute
s	second
U	units
V	volt

Prefixes

c	centi (10^{-2})
µ	micro (10^{-6})
m	milli (10^{-3})
n	nano (10^{-9})

Greek alphabet letters

α	alpha
β	beta
κ	kappa
γ	gamma

ABSTRACT

Melanoma is the deadliest of skin cancers and exhibits the highest level of brain tropism of all cancer types. Melanoma brain metastases (MBMs) are diagnosed in no less than 50 % of patients with stage IV melanoma, although these lesions are identified in an even higher number of patients *post-mortem*. While current immune-based and targeted therapies can help against brain lesions, responses are unpredictable and resistance and cancer relapses often occur. The origin and biology of MBM are not well understood; however, increasing evidence suggests that MBMs have distinct properties from other metastatic sites. Here, using a genetically heterogeneous panel of human-derived MBM cell lines, we aimed to identify brain-specific melanoma properties and molecular processes that can be targeted in the clinic. Using functional assays, we observed that MBM cells displayed a slower intrinsic growth rate *in vitro* compared to extracranial cells. Reverse phase protein array analyses highlighted MBM-specific protein expression in targets associated with proliferation, survival, adhesion and migration; these targets pointed towards RAC1 which was identified as upregulated in the MBM cells, possibly involving a distinct RAC1/PAK1/JNK1 signaling axis. Knockdown of RAC1 using shRNA or its inhibition using small molecule inhibitors (alone or together with BRAF inhibition) hindered MBM functional properties *in vitro*, while *in vivo* RAC1 knockdown resulted in reduced primary tumor growth and delayed tumor appearance. Furthermore, MBM proliferation, adhesion and migration were altered in the presence of growth factors such as insulin, brain soluble factors or neuron and glia co-cultures, pointing out the importance of the microenvironment in understanding MBM cell biology. Moreover, MBM aggressive behavior upon exposure to the brain microenvironment could be modulated by RAC1 levels, as demonstrated by our knockdown studies. Finally, although resistant to PI3K/AKT/mTOR and BRAF/MEK inhibitors, MBM cells displayed an increased sensitivity to ferroptosis inducers, opening the door to future novel anti-MBM therapeutic options. Our findings emphasize the importance of microenvironment's implication and of molecular characterization of MBM in order to achieve therapeutic efficacy.

Key words: melanoma, brain, metastasis, RAC1, microenvironment

1. INTRODUCTION

Skin cancer is the most frequent cancer worldwide (The Skin Cancer Foundation, 2022). This malignancy affects all ethnic groups and geographic regions and its frequency shows no signs of flattening. Skin cancer is commonly grouped into non-melanoma skin cancers (e.g.: basal cell carcinoma, squamous cell carcinoma) and melanoma (Gordon, 2013). Melanoma, while it constitutes only 5 % of all skin cancers, accounts for more than 75 % of skin cancer deaths; thus, it is the most lethal of all skin cancers and poses a serious health challenge (Licarete et al., 2020; Rebecca et al., 2020).

1.1. MELANOMA: an overview

1.1.1. History, definition and genesis

Melanoma is a term derived from the Greek *melas* (dark) and *oma* (tumor). Melanoma was first described in history in the 5th century BC in the works of Hippocrates of Kos, a Greek physician. The earliest physical evidence of melanoma can be found in the skeletons of pre-Colombian mummies, which displayed diffuse melanotic metastases. John Hunter is reported to be the first surgeon to successfully operate on a melanoma in the 18th century (Rebecca et al., 2012). Yet the 19th century was far more revolutionary in understanding the full extent of melanoma as disease. It was then when William Norris noted the propensity of melanoma to metastasize. He was also one of the first to believe that this disease is hereditary and to propose a link between nevi (benign moles) and melanoma. Furthermore, he noted that environmental factors may play an important role in developing the disease and made the observations that the majority of his patients were fair-skinned, had light-colored hair, and that some melanomas could be amelanotic (unpigmented or with little pigment) (Norris, 1820; Rebecca et al., 2012). In the mid-late 19th century, James Paget was the first pathologist to characterize the transformation of a melanoma from a radial growth phase (mild intraepidermal growth) to a vertical growth phase (dermal invasion); in addition, he was the first to describe melanoma in a dark-skinned patient (Paget, 1853; Rebecca et al., 2012). It was also in the 19th century when the word *melanoma* was coined by Robert Carswell; he left behind detailed drawings of melanoma metastases, including brain metastases (Carswell, 1838; Rebecca et al., 2012).

Later, in the 20th century, Wallace Clark conceived a contemporary, standard scale for assessing the prognosis of melanomas, known as *Clark's level*. This staging system divides the depth of tumor invasion into five levels, each level deadlier as the tumor cells invade deeper into the

skin (**Figure 1**). In the late 20th century, Alexander Breslow completed Clark's observations by stating the importance of not only the level of melanoma invasion, but also the tumor size, in the assessment of melanoma progression (Balch et al., 2009; Rebecca et al., 2012).

More than 30 % of melanomas are derived directly from initially benign, melanocytic nevi (Damsky and Bosenberg, 2017). Dysplastic nevi, defined as irregularly-shaped moles, can be dangerous if left to progress. These atypical nevi may acquire genetic alterations, leading to abnormal growth and dissemination, as shown in **Figure 1** (Gordon, 2013; Vultur and Herlyn, 2013).

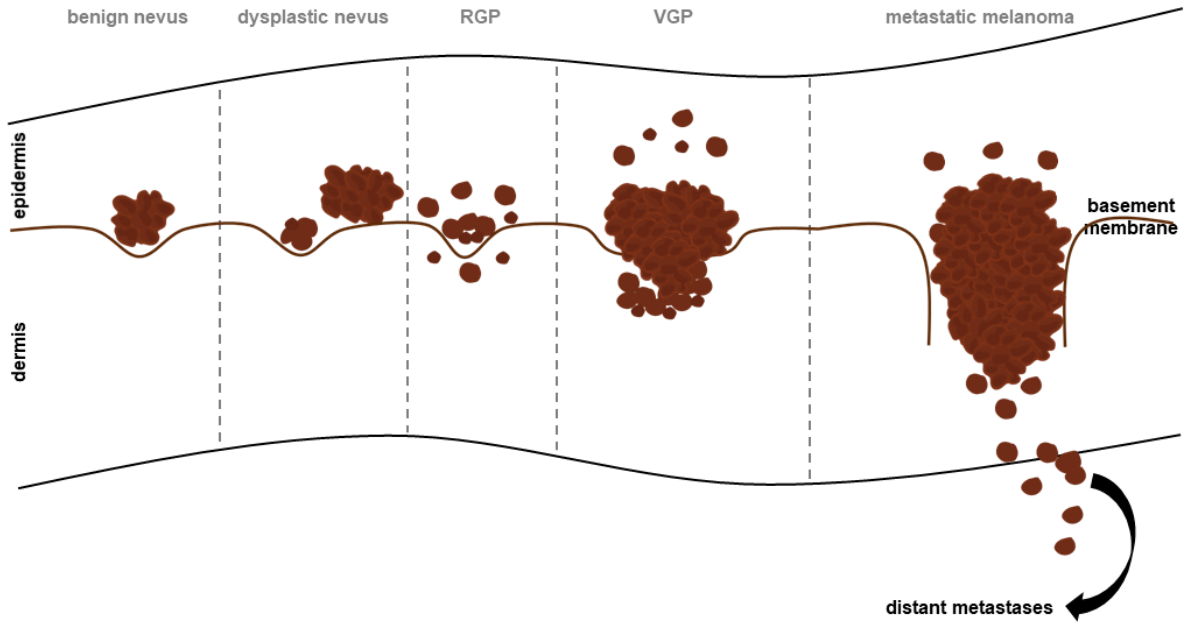

Figure 1. *An illustration of melanoma progression based on the Clark model.* The abnormal proliferation of melanocytes leads to the formation of benign nevi. The altered melanocytes generate asymmetric nevi (dysplastic). This step is followed by the radial growth phase, characterized by mild tumor spread. The vertical growth phase, characterized by deep skin penetration, precedes the aggressive malignant melanoma phase. Melanoma cells rapidly develop vasculature that provides routes for further metastases. This illustration was modified from http://www.pathophys.org/melanoma/. Abbreviations: RGP = radial growth phase; VGP = vertical growth phase.

Melanocytes are melanin-producing neural crest-derived cells that can be found in the basal epidermis. In response to UV-induced DNA damage, skin keratinocytes (primary type of cells found in the epidermis) produce melanocyte stimulating hormone (MSH) that binds to the melanocortin receptor 1 (MC1R) on melanocytes. Consequently, melanocytes produce melanin (skin pigment), which helps protect against further DNA alteration. One of the mechanisms by which UV radiation causes melanocytes' malignant transformation is through mutations that affect proto-oncogenes and/or tumor suppressor genes (such as *BRAF*, *NRAS, CDKN2A*, *NF1*, *PTEN*, *RAC1*, *TP53*, *TERT*). Another mechanism of disease progression involves the continued

transformation of melanocytes into initially benign nevi with a low mutation burden; these nevi can either remain dormant (due to immune surveillance or senescence) or UV radiation can trigger additional genetic mutations that lead to full malignant transformation (Leonardi et al., 2018). A visual representation of the melanocyte malignant transformation process is shown in **Figure 2**.

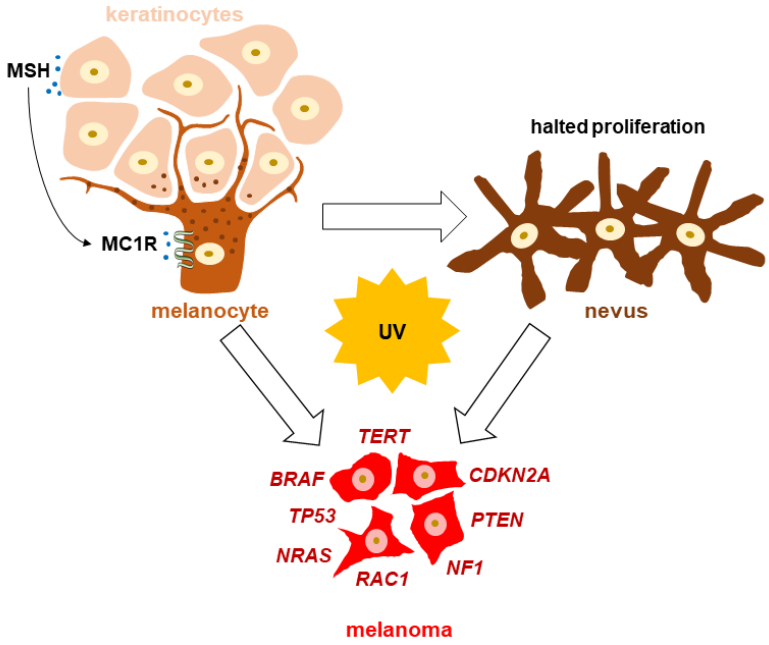

Figure 2. *Melanocyte malignant transformation.* Keratinocytes induce melanocyte growth through the production of MSH and its binding to MC1R. UV radiation can cause the direct transformation of normal melanocytes into melanoma cells through the accumulation of mutations in key cancer genes such as those shown in dark red. UV radiation can also cause a two-step malignant transformation of melanocytes; this involves the melanocyte transformation into benign nevi which can later acquire additional genetic mutations that cause melanoma. This illustration was modified from Leonardi et al., 2018. Abbreviations: *BRAF* = RAF kinase, isoform B; *CDKN2A* = cyclin-dependent kinase inhibitor 2A; *MC1R* = melanocortin 1 receptor; *MSH* = melanocyte-stimulating hormone; *NF1* = neurofibromin 1; *NRAS* = rat sarcoma protein, isoform N; *PTEN* = phosphatase and tensin homolog; *RAC1* = Ras-related C3 botulinum toxin substrate 1; *TERT* = telomerase reverse transcriptase; *TP53* = tumor protein p53.

Moreover, UV radiation leads to reactive oxygen species (ROS) production which also results in DNA damage (Wölfle et al., 2014). In comparison to normal melanocytes, dysplastic nevi exhibit increased ROS levels, implying that ROS accumulation also plays a role in melanomagenesis (Sample and He, 2018).

1.1.2. Epidemiology and risk factors for primary melanoma

In addition to UV radiation, there are other factors that can increase the risk of developing melanoma. According to The Skin Cancer Foundation and Gordon, 2013, these include:

- *Genetic factors.* Up to 10 % of melanoma patients have a first-degree relative with the disease and can carry underlying mutations.
- *Phenotypic factors.* People with fair skin, freckles, light-colored eyes/hair and who produce low levels of melanin are more prone to develop melanoma. The incidence of melanoma in white people is 20 times higher than in African Americans (**Figure 3**); however, the five-year survival rate is lower for black patients with advanced disease.
- *Dysplastic nevi.* Individuals with dysplastic nevi that are not removed can be at greater risk of melanoma following additional UV exposure.
- *Pre-cancers.* People who previously had a non-melanoma skin cancer are more likely to develop melanoma than the general population.
- *Socio-economic factors*, such as awareness of melanoma prevention, early detection or access to healthcare.

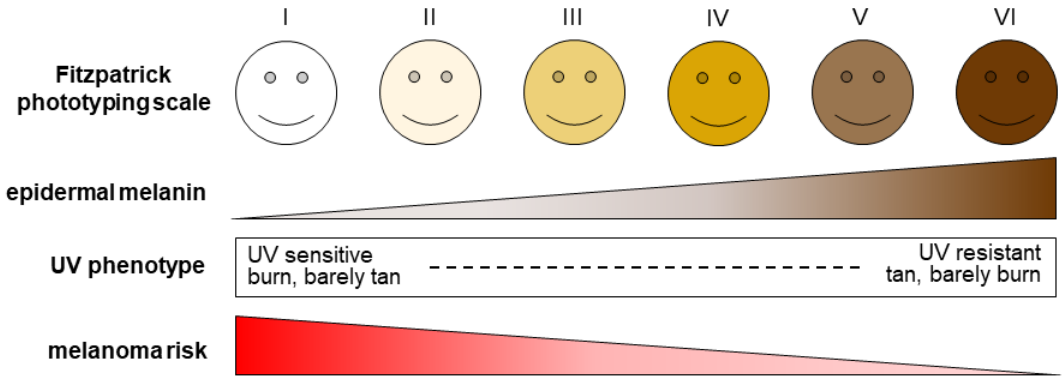

Figure 3. *Melanoma risk based on skin pigmentation.* Skin pigmentation can be assessed by the Fitzpatrick scale, wherein the higher the type number the more pigmented the skin is (types I-III: Europeans, white Americans, type IV: Asians and Latin Americans, types V-VI: Indians, Native Africans, African Americans). Black individuals are more UV resistant, i.e. they tan easily and their skin does not commonly burn upon UV exposure. Cutaneous melanoma risk is the highest in fair-skinned people. The design and content of the illustration was modified from D'Orazio et al., 2013.

More than 90 % of all melanoma cases are cutaneous melanomas, while less than 10 % are acral (a type of melanoma that appears on the palms of the hands, the soles of the feet or under the nails), mucosal (a type of melanoma that occurs on mucosal surfaces) or uveal (ocular) (Melanoma Research Alliance; Vultur and Herlyn, 2013).

This study is focused on cutaneous and cutaneous-associated metastatic melanoma.

1.1.3. Malignant melanoma

Over the last decade, melanoma cases have doubled to over 287,000 per year worldwide; more than 20 % of these cases are fatal (Euromelanoma & Global Coalition for Melanoma Patient

Advocacy, 2020). In Europe, melanoma claims over 20,000 lives each year, 2,500 of which in Germany alone (Forsea, 2020; Zentrum für Krebsregisterdaten, 2017). Melanoma is the deadliest of skin cancers due to its strong capacity to metastasize (Kodet et al., 2020). The five-year survival rate of patients with localized melanoma (stages 0-II) is higher than 98 % provided that the primary melanoma is surgically removed; however, the five-year survival rate drops to less than 64 % in patients with regional disease (stage III) and to less than 23 % in patients with metastatic melanoma (stage IV) (Melanoma Research Alliance; Rebecca et al., 2020). Melanoma is known to spread and form lymph node (stage III) and distant visceral metastases (stage IV) and the organs that are most frequently affected are the lungs, the liver and the brain (Kodet et al., 2020; Stahl et al., 2003).

1.1.4. Driver mutations and commonly deregulated signaling pathways

The realization that tumors arise due to the acquisition of genetic mutations was a major breakthrough in melanoma research (Rebecca et al., 2012). Of all human cancers, melanomas are associated with one of the highest tumor somatic mutation burden and chronic sun-exposure is believed to be the major cause of this (Davis et al., 2018). The most common somatic mutations in chronically sun-exposed skin melanoma alter genes that regulate cell proliferation and motility (e.g.: *BRAF*, *NRAS*, *NF1*, *RAC1*), metabolism (e.g.: *PTEN*), cell cycle control (*CDKN2A*), replicative lifespan (e.g.: *TERT*) or apoptosis (e.g.: *TP53*), also shown above in **Figure 2**. These alterations commonly lead to the deregulation of two key signaling cascades in melanoma: the mitogen-activated protein kinase (MAPK) pathway and the phosphoinositol-3-kinase/protein kinase B/mechanistic target of rapamycin (PI3K/AKT/mTOR) pathway (Leonardi et al., 2018). These pathways are described in detail below.

1.1.4.1. MAPK signaling

The mitogen-activated protein kinase (MAPK) pathway is involved in the transduction of extracellular signals (e.g.: hormones, growth factors) to the nucleus, ultimately leading to the expression of genes that are key drivers of cell proliferation and survival (Leonardi et al., 2018). The MAPK pathway is also the best characterized and the most commonly aberrantly activated signaling pathway in melanoma (Leonardi et al., 2018; Smalley, 2010). As a matter of fact, mutations predicted to constitutively activate MAPK are present in all melanoma patients, irrespective of their progression stage (Shain et al., 2018).

The identification of the rat sarcoma protein (RAS) superfamily of oncogenes in the 1980s was essential for understanding melanoma biology. RAS proteins are small GTPases, molecular switches that link receptor tyrosine kinases (RTKs) to downstream signaling molecules and are divided into five families: RAS, RHO, RAN, RAB and ARF; this study mostly focuses on the RAS and RHO families.

Three RAS proteins are clinically eminent, HRAS, KRAS and NRAS, mutated in approx. 1, 2, and 20 % of melanomas, respectively (Rebecca et al., 2012). NRAS was in fact the first oncogene described in melanoma (Albino et al., 1984). The most frequent NRAS mutations in melanoma are *Q61K*, *Q61R* and *Q61L*, in which glutamine is substituted at aminoacid 61 by lysine, arginine and leucine, respectively; it is hypothesized that this is due to the formation of dicyclobutane at the Q61 site upon UV exposure (Fernández-Medarde and Santos, 2011). NRAS mutations occur at early stages of melanoma progression and have been detected even at the nevi stage. Despite their early appearance, these mutations contribute to the aggressive nature of the disease and are therefore important yet difficult therapeutic targets. For example, the use of the farnesyltransferase inhibitor tipifarnib as an anti-melanoma therapy for NRAS-mutant patients was explored but has not yielded any beneficial clinical response thus far (Fernández-Medarde and Santos, 2011; Gajewski et al., 2012).

The downstream effectors of RAS are the rapidly accelerated fibrosarcoma (RAF) kinases, a family of three serine/threonine-specific protein kinases (ARAF, BRAF, CRAF) that, together with RAS proteins, participate in the MAPK cascade (Matallanas et al., 2011). The importance of RAF in melanoma was first shown in 2002, when a systematic genetic screen identified activating BRAF mutations in more than 50 % of cutaneous melanomas (Davies et al., 2002). Indeed, BRAF mutations are known to now occur in up to 60 % of melanomas, making them by far the most frequent genetic abnormalities in melanoma (Leonardi et al., 2018; Vultur and Herlyn, 2013). "*Guilty as charged"*, as Garnett and Marais referred to the BRAF oncogene (Garnett and Marais, 2004). Additionally, BRAF is mutated in up to 80 % of benign nevi which remain dormant for decades (or are controlled through immune surveillance), suggesting that the acquisition of BRAF mutations is an early and priming event in melanoma development, but also that mutant BRAF alone is not sufficient for melanomagenesis (Leonardi et al., 2018; Smalley, 2010).

More than 50 different BRAF mutations have been identified so far (Cheng et al., 2018). Of these, the BRAF*V600E* mutation, in which valine is substituted by glutamic acid at aminoacid 600, is the most frequent BRAF mutation (accounting for more than 80 % of all reported BRAF mutations) (Czarnecka et al., 2020). Other BRAF mutations include valine to lysine (*V600K*),

valine to aspartic acid (*V600D*) or valine to arginine (*V600R*) substitutions (Leonardi et al., 2018).

The identification of BRAF as an oncogene in 2002 was the foundation for successful anti-melanoma targeted therapies. Notably, less than 10 years later, the United States Food and Drug Administration (FDA) approved vemurafenib (a mutant BRAF inhibitor) for the treatment of patients with advanced melanoma that harbor the BRAF*V600E* mutation. Additionally, the observation that BRAF and NRAS activating mutations are generally mutually exclusive in melanoma points out once more the importance and strength of mutating single elements of the MAPK pathway in triggering melanomagenesis (Davies et al., 2002; Fernández-Medarde and Santos, 2011; Sensi et al., 2006).

Following their activation, RAF kinases trigger the MAPK cascade, leading to the phosphorylation and subsequent activation of mitogen-activated protein kinase kinases (MEK) proteins which consecutively activate extracellular signal-regulated kinase (ERK). Once stimulated, ERK either activates cytoplasmic proteins or travels to the nucleus where it phosphorylates transcription factors with key roles in melanoma progression and survival (**Figure 4**) (Smalley, 2010).

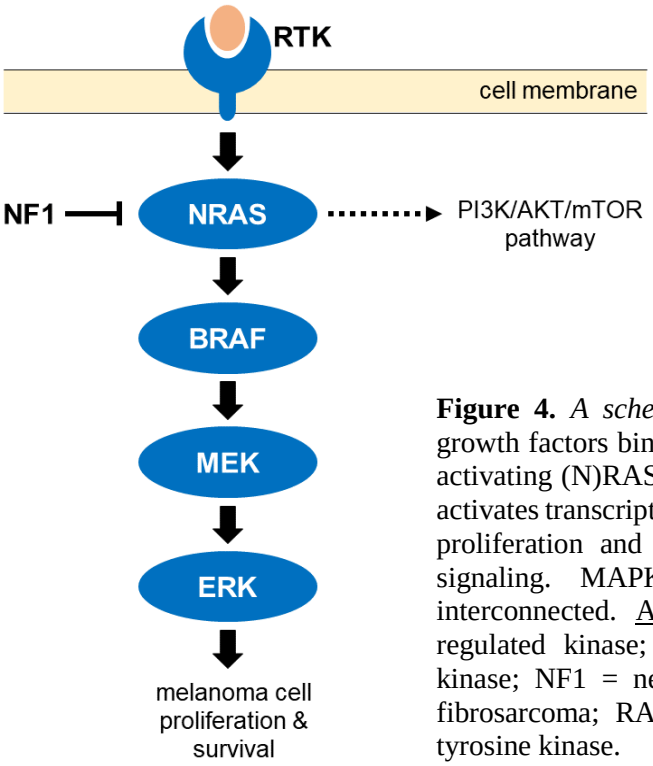

Figure 4. *A schematic of the MAPK pathway*. Extracellular growth factors bind to RTK and initiate the MAPK cascade by activating (N)RAS, (B)RAF, MEK and ultimately ERK, which activates transcription factors that regulate genes involved in cell proliferation and survival. NF1 inhibits NRAS downstream signaling. MAPK and PI3K/AKT/mTOR pathways are interconnected. Abbreviations: ERK = extracellular signal-regulated kinase; MEK = mitogen-activated protein kinase kinase; NF1 = neurofibromin 1; RAF = rapidly accelerated fibrosarcoma; RAS = rat sarcoma protein; RTK = receptor tyrosine kinase.

Another important oncogene (indirectly) involved in the MAPK pathway is neurofibromin 1 (NF1), mutated in 10-15 % of melanomas. NF1 regulates the RAS family of proteins by inhibiting downstream RAS signaling, i.e. it converts active RAS-guanosine triphosphate

(RAS-GTP) to inactive RAS-guanosine diphosphate (RAS-GDP). Hence, NF1 loss-of-function in melanoma leads to increased MAPK signaling by hyperactivating NRAS (Leonardi et al., 2018).

MAPK signaling plays an indubitable key role in melanoma biology. Its blockade has shown positive outcomes in patients, resulting in the development and approval of vemurafenib, dabrafenib (both BRAF inhibitors) or trametinib (MEK inhibitor) for the treatment of melanoma patients that harbor BRAF mutations (Chapman et al., 2011; Dummer et al., 2020; Shannan et al., 2016). Unfortunately, these drugs (administered as single agents or in combination with other kinase inhibitors) are by no means equally effective in all BRAF-mutant patients. BRAF/MEK inhibitor resistance for example can occur as a result of the activation of the phosphoinositide 3-kinase (PI3K) cascade following signaling rewiring or through additional genetic mutations (Shannan et al., 2016; Villanueva et al., 2010; Villanueva et al., 2013). Mutations in MEK can also lead to the reactivation of the MAPK pathway (Villanueva et al., 2013).

1.1.4.2. PI3K/AKT/mTOR signaling

The phosphoinositol-3-kinase / protein kinase B / mechanistic target of rapamycin (PI3K/AKT/mTOR) pathway is important for cell cycle regulation, immunity or homeostasis. This pathway is involved in many cancer types, including melanoma, where it is the second most commonly activated pathway (Leonardi et al., 2018).

Under normal conditions, once the pathway is activated upstream, PI3K is recruited to the plasma membrane, where it phosphorylates phosphatidylinositol-4,4-bisphosphate (PIP_2) to phosphatidylinositol-3,4,5-trisphosphate (PIP_3). Following this, PIP_3 recruits phosphoinositide-dependent kinase-1 (PDK1) and AKT, the latter regulating cell cycle progression and survival processes on its own (Hoxhaj and Manning, 2020; Porta et al., 2014). Events that can instigate the abnormal activation of the PI3K/AKT/mTOR cascade in melanoma include increased growth factor binding to RTK receptors, mutations in pathway effectors or the loss of negative pathway regulators.

Alterations in *PI3K* genes are not that common in melanoma; despite this, the activity of the PI3K/AKT/mTOR cascade is elevated, frequently due to genetic mutations in the phosphatase and tensin homolog (*PTEN*) which negatively regulates PI3K activity (Kwong and Davies, 2013; Shannan et al., 2016). The tumor suppressor PTEN is one of the most important regulators of PI3K and its expression is lost in up to 30 % of melanomas (Smalley, 2010). Notably, nearly

all melanomas with *PTEN* alterations carry additional key genetic modifications in other pathways such as MAPK (Aguissa-Touré and Li, 2012; Stahl et al., 2003).

AKT, a serine-threonine kinase, is an essential downstream effector of PI3K. Mutations in the *AKT* gene have been described as well; when expressed in melanoma, these can lead to the permanent activation of AKT (Davies et al., 2008). AKT, in turn, has multiple downstream effectors that regulate cell metabolism and survival, such as the mTOR complex (Kong et al., 2016).

A simplified representation of the PI3K/AKT/mTOR cascade is shown below (**Figure 5**).

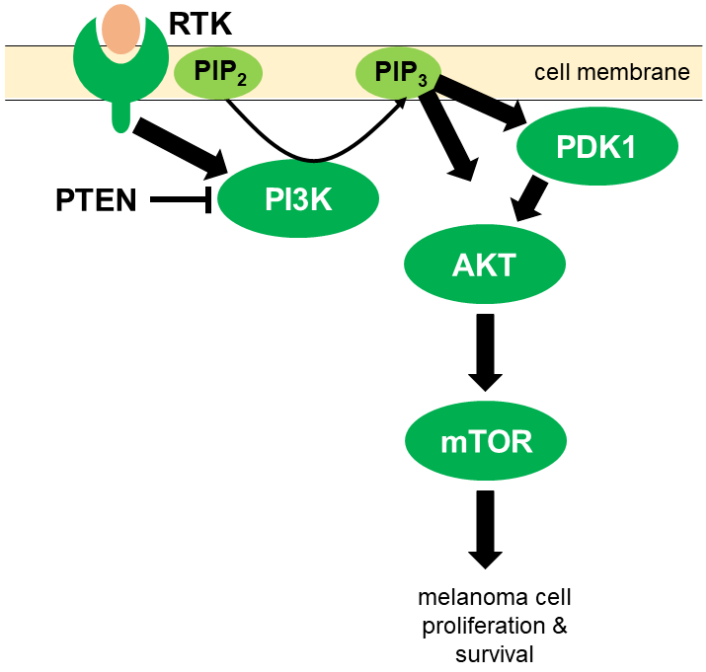

Figure 5. *Schematic of the PI3K/AKT/mTOR pathway*. Extracellular growth factors bind to RTK and initiate the cascade by activating PI3K which phosphorylates PIP_2 to PIP_3. PIP_3 recruits PDK1 and AKT, the latter activates mTOR, which ultimately regulates cell proliferation and survival. The PI3K/AKT/mTOR cascade is inhibited by PTEN. Abbreviations: AKT = protein kinase B; mTOR = mechanistic/mammalian target of rapamycin; PDK1 = phosphoinositide-dependent kinase-1; PI3K = phosphoinositol-3-kinase; PIP_2 = phosphatidylinositol-4,4-bisphosphate; PIP_3 = phosphatidylinositol-3,4,5-trisphosphate; PTEN = phosphatase and tensin homolog; RTK = receptor tyrosine kinase.

mTOR comprises two functionally distinct protein complexes: mTORC1 and mTORC2. Structurally, the mTORC1 complex consists of mTOR and the regulatory proteins RPTOR, mLST8, PRAS40 and DEPTOR. RPTOR is a scaffold protein that controls mTOR activity by recruiting mTORC1 substrates. Activation of the mTORC1 complex results in the phosphorylation of p70S6K and 4E-BP1. Elevated activity in these two signaling molecules leads to abnormal cell proliferation. mTORC2 consists of mTOR and the regulators RICTOR, mLST8, mSIN1, PROTOR, HSP70 and DEPTOR (Pópulo et al., 2012). RICTOR, a protein that is exclusive to mTORC2, is a key regulator of the PI3K/AKT/mTOR pathway, which plays

a crucial role in tumors driven by RTK alterations (Jebali and Dumaz, 2018; Pópulo et al., 2012). The two mTOR complexes have antagonistic effects on AKT signaling, with mTORC1 inhibiting AKT and mTORC2 stimulating it (Kim et al., 2017).

A schematic representation of the mTOR complexes is presented below (**Figure 6**).

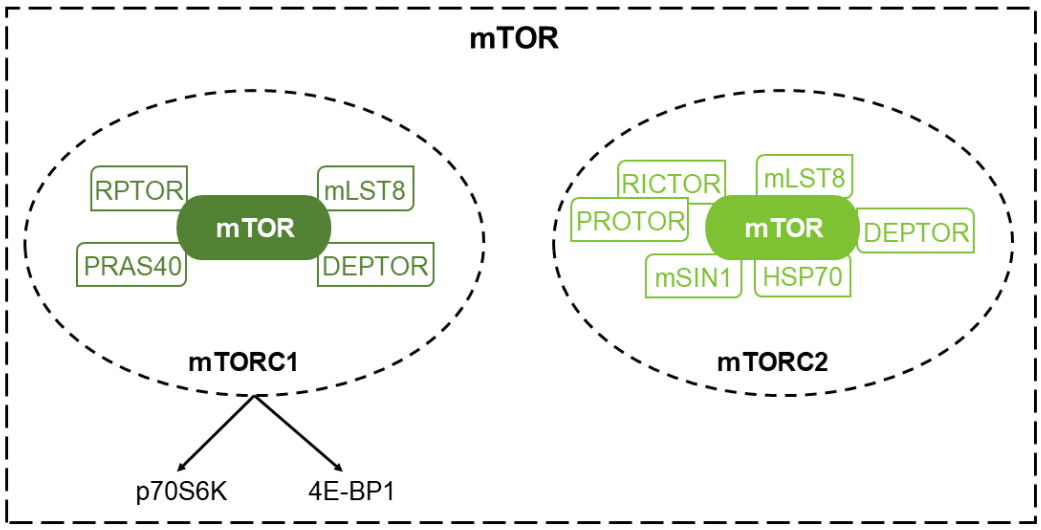

Figure 6. *The structure of the mTOR complexes.* mTOR consists of two protein complexes: mTORC1 and mTORC2. The mTORC1 complex comprises mTOR, RPTOR, mLST8, PRAS40 and DEPTOR. mTORC2 consists of mTOR, RICTOR, mLST8, mSIN1, PROTOR, HSP70 and DEPTOR. Abbreviations: 4E-BP1 = 4E-binding protein 1; DEPTOR = DEP domain-containing mTOR-interacting; HSP70 = 70 kilodalton heat shock protein; mLST8 = mammalian lethal with SEC13 protein 8; mSIN1 = mammalian stress-activated protein kinase-interacting protein; mTOR = mechanistic/mammalian target of rapamycin; mTORC1/2 = mTOR complex 1/2; p70S6K = ribosomal protein S6 kinase beta-1; PRAS40 = 40 kilodalton proline-rich AKT1 substrate 1; PROTOR = protein observed with RICTOR; RICTOR = rapamycin-insensitive companion of mammalian target of rapamycin; RPTOR = regulatory associated protein of mTOR.

With regard to therapeutic approaches, inhibitors of the PI3K/AKT/mTOR pathway and its members were investigated clinically (e.g.: BKM120, GDC-0941, MK-2206, rapamycin) but, for melanoma, they are not currently considered frontline therapeutic options (Hanker et al., 2019).

1.1.4.3. RAC1 signaling

RAS-related C3 botulinum toxin substrate 1 (RAC1) is a highly conserved member of the RAS superfamily of proteins. More specifically, RAC1 is one of the members of the RAS homologous protein (RHO) family of small GTPases, which contains the other two RAC isoforms (RAC2 and RAC3), cell division control protein 42 homolog (CDC42) and the Rho and Rnd subgroups (Cannon et al., 2020). RhoA, RAC1 and CDC42 are known to coordinate

in a spatio-temporal manner in order to modulate cellular functions such as cytoskeletal dynamics and adhesion processes (Martin et al., 2016).

RAC1 can transduce extracellular signals from integrins or growth factors and can be activated by other proteins such as the focal adhesion kinase (FAK) or the proto-oncogene tyrosine-protein kinase SRC (Chang et al., 2007; Feng et al., 2011; Watson et al., 2018). Just like all the other proteins of the RHO family, it is inactive when bound to guanosine diphosphate (GDP) and active when bound to guanosine triphosphate (GTP) (Cannon et al., 2020). When in its active state, RAC1 binds to and activates a variety of effector proteins; among the best understood and characterized targets downstream of RAC1 are the p21-activated protein kinases (PAK1/2/3), which are also currently druggable (Araiza-Olivera et al., 2017; Cannon et al., 2020). PAK proteins stimulate cell proliferation by phosphorylating proteins of the MAPK pathway, but also membrane-cytoskeleton proteins such as Merlin (Cannon et al., 2020). On the other hand, RAC1 has been reported to have scaffolding functions in its inactive form too. For instance, Saci and colleagues demonstrated that RAC1 directly binds to mTOR and that this interaction is independent of the GTP/GDP-binding state of RAC1 (Saci et al., 2011).

Along with its downstream effectors, RAC1 plays crucial roles in proliferation, differentiation, survival, cell shape, motility, migration, ROS production, as well as in inflammatory responses (Cannon et al., 2020; Vu et al., 2015). Thus, RAC1 regulates signaling pathways such as MAPK, PI3K/AKT/mTOR, c-Jun N-terminal kinase (JNK), nuclear factor kappa-light-chain-enhancer of activated B cells (NF-κB) and processes related to redox regulation (Bosco et al., 2009). RAC1 was also proven essential for the oncogenic activity of RAS in a focus-forming assay in fibroblasts (Qiu et al., 1995). Hence, RAC1 is considered a central signaling hub that is required for transformation by numerous oncogenes and with multiple downstream effects (Cannon et al., 2020).

The discovery of activating mutations in the RAC1 gene points to a previously unknown melanoma driver (Cannon et al., 2020). RAC1 genetic alterations occur in approximately 10 % of melanoma patients (Davis et al., 2018). Of these, RAC1*P29S* is the most studied as it was identified as the third most common driver mutation in sun-exposed melanomas after BRAF*V600E* and NRAS*Q61K* (Hodis et al., 2012). Of note, the proline to serine substitution at codon 29 is a C>T transition (CCT>TCT), a molecular signature of UV radiation damage (Krauthammer et al., 2012).

RAC1 mutations tend to co-occur with gain-of-function (e.g.: NRAS or BRAF) and/or loss-of-function mutations (e.g.: PTEN, NF1, TP53), suggesting that RAC1 alterations alone do not cause melanomagenesis (Cannon et al., 2020; Davis et al., 2018). Additionally, the co-

occurrence of RAC1 mutations with BRAF mutations results in resistance to BRAF/MEK inhibition and, therefore, to poorer patient prognosis (Cannon et al., 2020; Watson et al., 2014). In the absence of RAC1 mutations, upstream proteins of the RAC1 pathway are frequently mutated and/or overexpressed in a variety of cancers including melanoma (Berger et al., 2012; Kaneto et al., 2014; Wertheimer et al., 2012). For instance, the phosphatidylinositol 3,4,5-trisphosphate-dependent RAC exchanger protein (PREX), a guanine nucleotide exchange factor (GEF), regulates RAC1 activity and melanoma invasion when aberrantly upregulated *in vitro* (Cannon et al., 2020; Ryan et al., 2016). Other relevant GEFs and their inhibitory compounds are shown in **Figure 7**.

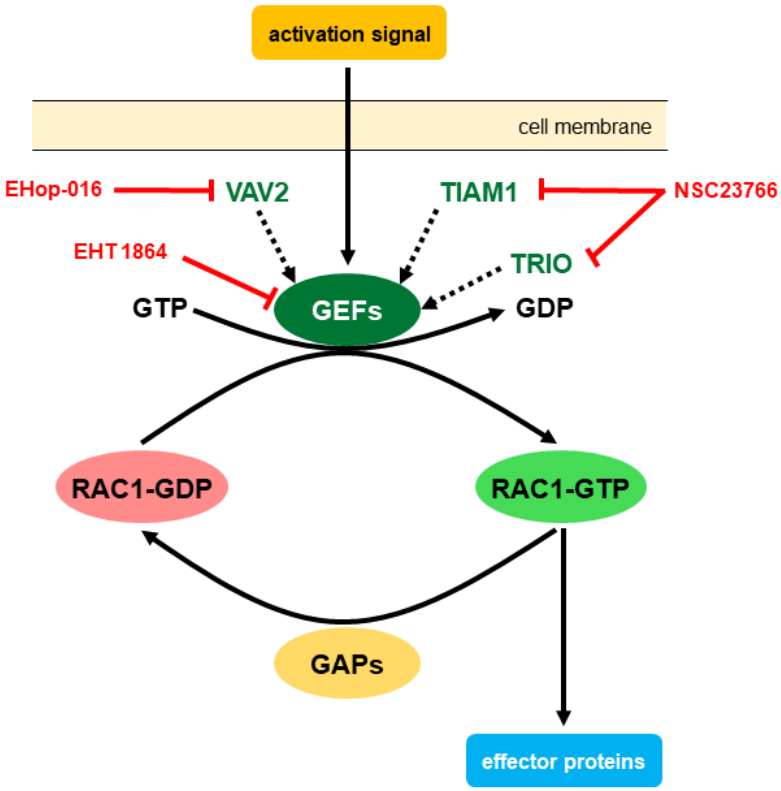

Figure 7. *RAC1 activation and regulation.* GEFs are activated through extracellular signals. The cycling between the inactive (GDP-bound) and active (GTP-bound) RAC1 form is mediated by GEFs and GAPs. Inhibitory compounds such as EHop-016, EHT 1864 and NSC23766 suppress RAC by blocking GEF activity. Active RAC1-GTP interacts with effector proteins to regulate cellular response. Abbreviations: GAPs = GTPase-activating proteins; GDP = guanosine diphosphate; GEFs = guanine nucleotide exchange factors; GTP = guanosine triphosphate; RAC1 = RAS-related C3 botulinum toxin substrate 1; TIAM1 = T-cell lymphoma invasion and metastasis-inducing protein 1; TRIO = triple functional domain protein.

RAC1 can be inhibited by various compounds such as EHop-016, EHT 1864 or NSC23766; however, these are not yet approved for use in the clinics. NSC23766 prevents RAC1 activation by inhibiting TIAM1 and TRIO-regulated cell proliferation, without affecting RhoA or CDC42 activation. As opposed to the other two aforementioned RAC1 inhibitors, NSC23766 is a

selective inhibitor of RAC1 (Gao et al., 2004). However, this compound has a very low efficacy and an excessively high IC50 (Cannon et al., 2020; Liang et al., 2021). EHop-016 on the other hand, which blocks VAV2, is a more potent compound that was shown to be efficient for long treatments *in vivo;* thus, it is a lead for potential non-toxic anti-cancer therapeutics (Montalvo-Ortiz et al., 2012). Nonetheless, EHop-016 is not a selective RAC1 inhibitor (it targets RAC3 as well; plus, at high concentrations, it can target CDC42), therefore additional studies are needed to dissect essential inhibiting properties (Cannon et al., 2020). EHT 1864 is an inhibitor that binds to all RAC isoforms by preventing GEF-mediated nucleotide exchange (Onesto et al., 2008). However, this compound has significant off-target effects in wild-type cells (Cannon et al., 2020). Prior to a significant effort to develop better RAC inhibitors, immunotherapies took center stage in melanoma therapy; thus, there is still space for improved RAC-associated drug development.

1.1.4.4. Crosstalk between melanoma signaling pathways

Unfortunately, melanomas do not harbor mutations in only one pathway which could be "easily" targeted, but they hold a heavy mutation burden instead. The main signaling cascades deregulated in melanoma (described above in sections **1.1.4.1**, **1.1.4.2** and **1.1.4.3**) are interconnected via regulatory feedback loops. Thus, the inhibition of one pathway can lead to the activation of another in a compensatory way (Smalley, 2010).

Furthermore, preclinical studies have shown that MAPK and PI3K/AKT/mTOR pathways have overlapping functions in melanoma (Tsao et al., 2000; Smalley, 2010). Since gain-of-function mutations in NRAS can stimulate both pathways, seldom one tumor carries BRAF and NRAS mutations simultaneously (Smalley, 2010). Similarly, BRAF genetic alterations are regularly found in combination with PTEN loss or activating AKT mutations, demonstrating again the complementary activity of the PI3K/AKT/mTOR and MAPK cascades (Davies et al., 2008; Smalley, 2010).

In vivo mouse studies have proven that melanocyte-specific BRAF*V600E* mutations lead to benign melanocytic hyperplasia but not to melanoma; melanomagenesis arose only when the BRAF*V600E* mutation was triggered in the presence of PI3K/AKT/mTOR activity after the inhibition of PTEN expression (Dankort et al., 2009; Smalley, 2010).

RAC1 can also contribute to melanomagenesis by activating PAK and AKT (Dorard et al., 2017; Lionarons et al., 2019). RAC1*P29S* hotspot mutation was shown to cooperate with BRAF or NF1 loss to promote melanocyte malignant transformation; moreover, the presence of this mutation led to BRAF inhibitor resistance in mice (Lionarons et al., 2019). In addition, the

RAC1 direct effector PAK1 is overexpressed in a subset of BRAF wild-type melanomas (Ong et al., 2013). Furthermore, CRAF and MEK1 are two of the most established PAK1 substrates that lose their activity when PAK1 is inactive, emphasizing the importance of PAK/MEK/ERK signaling in melanoma biology (Araiza-Olivera et al., 2017). Moreover, PAK can become activated in acquired MAPK inhibitor-resistant melanoma cells (Lu et al., 2017). Of note, studies suggest that the RAC*P29S* mutation might regulate PD-L1 expression and mediate resistance to targeted- and immunotherapies (Vu et al., 2015; Watson et al., 2014).

Melanomas exhibit activity in multiple other pathways that contribute to its aggressive nature, such as the signal transducer and activator of transcription 3 (STAT3), SRC/FAK, NF-κB, among others; therefore, the identification of effective anti-melanoma therapies requires careful tumor characterization and multiple or sequential approaches, as melanoma is a highly heterogeneous (from both genetic and biological points of view) and adaptable skin cancer (Grzywa et al., 2017; Rebecca et al., 2012; Roesch et al., 2013; Smalley, 2010).

A schematic representation of signaling networks relevant to this study is shown in **Figure 8**.

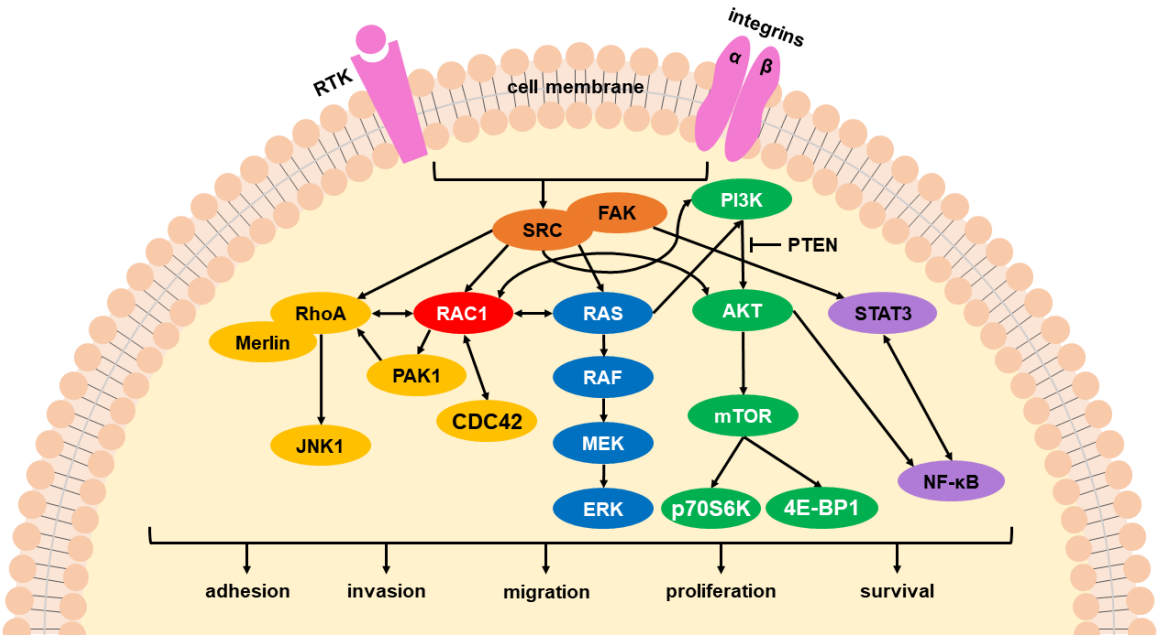

Figure 8. *Key melanoma signaling cascades and therapeutic targets.* Extracellular signals from RTKs or integrins trigger the activation of SRC/FAK, which stimulate downstream signaling cascades, including RAC1/RhoA/CDC42, MAPK, PI3K/AKT/mTOR, STAT3 and NF-κB, ultimately leading to the regulation of cellular processes crucial for melanoma progression, such as adhesion, invasion, migration, proliferation or survival. Abbreviations: 4E-BP1 = eukaryotic translation initiation factor 4E (eIF4E)-binding protein 1; AKT = protein kinase B; CDC42 = cell division control protein 42 homolog; ERK = extracellular signal-regulated kinase; FAK = focal adhesion kinase; JNK1 = c-Jun N-terminal kinase 1; MEK = mitogen-activated protein kinase kinase; mTOR = mechanistic/mammalian target of rapamycin; NF-κB = nuclear factor kappa-light-chain-enhancer of activated B cells; p70S6K = ribosomal protein S6 kinase beta-1; PAK1 = P21-activated kinase 1; PI3K = phosphatidylinositol 3-kinase; PTEN = phosphatase and tensin homolog; RAC1 = RAS-related C3 botulinum toxin substrate 1; RAF = rapidly accelerated fibrosarcoma; RAS = rat sarcoma protein; RhoA = RAS homolog family

member A; RTK = receptor tyrosine kinase; SRC = proto-oncogene tyrosine-protein kinase; STAT3 = signal transducer and activator of transcription 3.

1.1.5. Reactive oxygen species in melanoma progression

Oxidative phosphorylation (OXPHOS) in the mitochondria is an essential ATP-producing process for eukaryotic cells. Within the electron transfer chain of mitochondria, oxygen is the final electron acceptor and is thus reduced to water, which is harmless; the electron transfer might be nonetheless not entirely efficient and can result in the production of reactive oxygen species (ROS) (Murphy, 2009; Wittgen and van Kempen, 2007). Low ROS amounts are essential for the regulation of signaling cascades in healthy cells; however, excessively generated ROS can provoke cell damage and, implicitly, cell death (Sies et al., 2017; Wittgen and van Kempen, 2007). Hence, cells have developed antioxidant networks to scavenge excessive ROS. A balance between production and scavenging of ROS leads to homeostasis, but normal cellular processes can be altered if this balance is disturbed and this occurs frequently in cancer cells (Stafford et al., 2018; Wittgen and van Kempen, 2007).

ROS are emerging as important drivers of tumor cell growth, metastatic spread, metabolism and drug resistance (Chio and Tuveson, 2017; Zhang et al., 2019). Studies have demonstrated that cancer cells, including melanoma cells, display high levels of ROS (Fruehauf and Meyskens Jr., 2007; Liu-Smith et al., 2014; Meyskens Jr. et al., 2001). Melanoma is a ROS-driven type of cancer, as ROS was shown to be involved in multiple stages and aspects of melanomagenesis (Liu-Smith et al., 2014; Roesch et al., 2013; Wittgen and van Kempen, 2007). Glutathione and thioredoxin systems, the two main cellular antioxidant systems, are also upregulated in melanoma cells compared to melanocytes (Cassidy et al., 2015; Estrela et al., 2006). Therefore, elevated ROS levels and a more powerful antioxidant system form together an equilibrium in tumor cells with the purpose of maintaining ROS levels in non-toxic ranges (Liu-Smith et al., 2014).

In addition to mitochondria, ROS can also be generated as byproducts of biochemical processes such as melanogenesis (production of melanin pigments), as well as of specialized ROS-producing enzymes such as the membrane-bound enzyme complex NADPH oxidases (NOXs). The NOX family of enzymes consists of 7 members (NOX1, NOX2, NOX3, NOX4, NOX5, DUOX1 and DUOX2) which play key roles in melanoma development (Liu-Smith et al., 2014). Of these, NOX1, NOX2 and NOX3 were shown to be regulated by RAC proteins (and not CDC42 or RhoA). NOX1 is activated by RAC and NOXA1 (member of the NOX1 complex) together. RAC also binds to the oxidase activator p67-phox, which interacts with NOX2, culminating in ROS production. Moreover, RAC facilitates ROS generation by NOX3 in the

presence of either NOXA1 or p67-phox (Hordijk, 2006; Miyano and Sumimoto, 2012; Raz et al., 2010).

Antioxidants are broadly used to protect cells from ROS-induced damage. The conception that antioxidants have an anti-cancer effect, supported by some scientific studies and highly promoted by the food supplement industry, has taken deep roots in society. However, preclinical studies as well as clinical trials have reported conflicting results (Watson, 2013). For instance, it has been demonstrated that in lung cancer mouse models the antioxidants vitamin E and N-acetylcysteine (NAC) actually promoted tumor progression and decreased survival by reducing ROS, DNA damage and p53 expression (Sayin et al., 2014). Moreover, in a patient-derived xenograft (PDX) melanoma model, antioxidants were shown to promote distant metastasis (Piskounova et al., 2015). Taken together, ROS and antioxidants have important yet not fully understood functions in melanoma and additional studies are needed to explore their therapeutic potential.

1.1.6. Ferroptosis in melanoma

Ferroptosis, first coined in 2012, is a form of regulated cell death that arises from iron-dependent lipid peroxidation (Dixon et al., 2012; Stockwell et al., 2017). Ferroptosis was observed as different from other known forms of regulated cell death such as apoptosis, necrosis or autophagy-dependent-cell death in terms of cell morphology and function (Conrad et al., 2021; Galluzzi et al., 2018; Li et al., 2020). Furthermore, unlike apoptosis, ferroptosis has not yet been shown to require the expression or post-translational activation of pro-death proteins (Dixon, 2017).

The best characterized key regulator of ferroptotic cell death is glutathione peroxidase-4 (GPX4). GPX4 protects cells from this iron-dependent-cell death using glutathione that removes phospholipid peroxides. Ferroptosis is augmented under conditions of GPX inactivation, under dysregulated cysteine trafficking or under chronic oxidative stress, i.e. lipid peroxidation (Stockwell et al., 2020).

Small-molecule compounds can block the cystine/glutamate antiporter (e.g.: erastin) or GPX4 activity (e.g.: RSL3) and can therefore trigger ferroptosis. RSL3 and erastin were first observed to kill RAS-mutated tumor cells *in vitro,* but the mechanism for ferroptotic susceptibility in these cells is unclear (Dolma et al., 2003; Yang and Stockwell, 2008; Ye et al., 2020). Another ferroptosis inducer which deprives cells of glutathione is buthionine sulfoximine (BSO), heretofore used in preclinical *in vitro* models as an antioxidant inhibitor (Cen et al., 2002; Wittgen and van Kempen, 2007).

Cancer cells exhibit an increased iron demand in order to enable tumor growth; this iron dependency might render tumor cells more vulnerable to ferroptosis (Hassannia et al., 2019). Ferroptosis may thus be fatal to many cancer cells (including drug-resistant cells), unlike apoptosis, which many cancer cells can evade or delay (Feng et al., 2020). Accordingly, ferroptosis has emerged as a promising approach in overcoming apoptosis-resistant chemotherapeutic agents (Xu et al., 2019). On the other hand, certain cancer cell lines are resistant to ferroptosis inducers, indicating that there are further unknown factors that regulate this process (Ye et al., 2020). A recent study reported that the less oxidizing environment of the lymphatic system, compared to the blood system, protects metastatic melanoma cells from ferroptosis, granting them a growth and dissemination advantage (Ubellacker et al., 2020). Moreover, it has been shown that melanoma dedifferentiation enhances tumor cell sensitivity to ferroptosis and that this can be blocked by combining ferroptosis inducers with targeted anti-melanoma therapy (Tsoi et al., 2018). Despite these findings, many aspects regarding the role of ferroptosis in melanoma biology and therapeutic sensitivity are still not fully understood and are now gaining momentum.

1.1.7. The immunogenicity of melanoma

Melanoma is a highly immunogenic tumor whose relationship with immune cells impacts cancer cell proliferation and dissemination. During melanoma development, both melanoma and immune cells undergo immunoediting. This dynamic process involves (1) the elimination of cancer cells by immunosurveillance, (2) an equilibrium between tumor and immune cells and (3) an immune escape or a strategy used by cancer cells to evade immune response (Passarelli et al., 2017; Tucci et al., 2019). The elimination step is based on consecutive events that lead to anti-melanoma cytotoxicity by natural killer (NK) cells, dendritic cells (DCs), T- and B- cells. These events occur broadly in peripheral tissues or more precisely within the tumor microenvironment. The equilibrium phase is defined as a quiescent state wherein cancer cell proliferation is equally balanced by tumor cell eradication by the adaptive immune system (mostly T-cells). The immune escape relies mainly on the antigen processing machinery of extra- and intracellular signals that hinder $CD8^+$ T-cell recognition of target antigens on tumor cells (Passarelli et al., 2017).

NK cells recognize and attack melanoma cells that express low major histocompatibility complex (MHC) class-I molecules (Passarelli et al., 2017). In addition, NK cells might contribute to immunosurveillance by promoting the maturation of DCs or by stimulating the secretion of cytokines within the tumor microenvironment (Passarelli et al., 2017; Wehner et

al., 2011). Mature DCs equilibrate immune response efficacy and the capacity of T-cells to induce a cytotoxic effect (Passarelli et al., 2017). Other immune cells that interact with melanoma cells are tumor-associated macrophages (TAMs), T-regulatory (Treg) cells and myeloid-derived suppressor cells (MDSCs) (Tucci et al., 2019).

Remarkable advances in the immunology research field have led to the development of anti-melanoma immunotherapies vastly used nowadays in the clinics. Three components of the immune system are particularly relevant for the treatment of melanoma; these are: the cytotoxic T-lymphocyte-associated protein 4 (CTLA-4), the programmed cell death protein 1 (PD-1) and the programmed death-ligand 1 (PD-L1). CTLA-4 and PD-1 are members of a family of immunoglobulin-related receptors that inhibit T-cell function and hence immune responses (Han et al., 2020; Rowshanravan et al., 2018). PD-L1 is one of the ligands of PD-1 and is considered a co-inhibitory factor of the immune response (Han et al., 2020; Sharpe and Pauken, 2017).

1.1.8. The tumor microenvironment

Malignant melanoma is challenging to treat due to therapy resistance supported by both tumor cells and the tumor microenvironment (TME) (Licarete et al., 2020). Melanoma cells are able to adapt and utilize a variety of methods that stimulate tumor progression and metastatic spread. They form a pro-neoplastic TME or a "premetastatic niche" comprised of immune cells of hematopoetic origin (e.g.: Treg cells, TAMs, DCs, MDSCs, NK cells) and cells of mesenchymal origin (fibroblasts and pericytes) (Fischer et al., 2017; Gener Lahav et al., 2019; Kerkar and Restifo, 2012), as depicted in **Figure 9**.

Cell infiltrates within the TME provide optimal cytokine secretion that stimulates cancer cell growth and helps establish an environment that fosters neo-angiogenesis. These TME cells become alternatively activated and can change their phenotype; these events can also alter normal T-cell functions (Kerkar and Restifo, 2012). Tumor cells can selectively recruit Treg cells (immune response suppressors) and polarize TAMs to a pro-tumorigenic phenotype (M2 macrophages) (Licarete et al., 2020). Additionally, MDSCs can overproduce ROS that promote tumor cell proliferation and DCs can activate Treg cells which in turn secrete suppressive cytokines of the immune system (e.g.: TGF-β, IL-10). Melanoma cells can also lose normal MHC class I expression and secrete pro-angiogenic growth factors (e.g.: VEGF, GM-CSF, G-CSF) which allows them to grow and disseminate (Kerkar and Restifo, 2012). Finally, cancer-associated fibroblasts also contribute to the aggressive behavior of melanoma cells, according to *in vitro* (Jobe et al., 2016) and *in vivo* studies (Hutchenreuther et al., 2018).

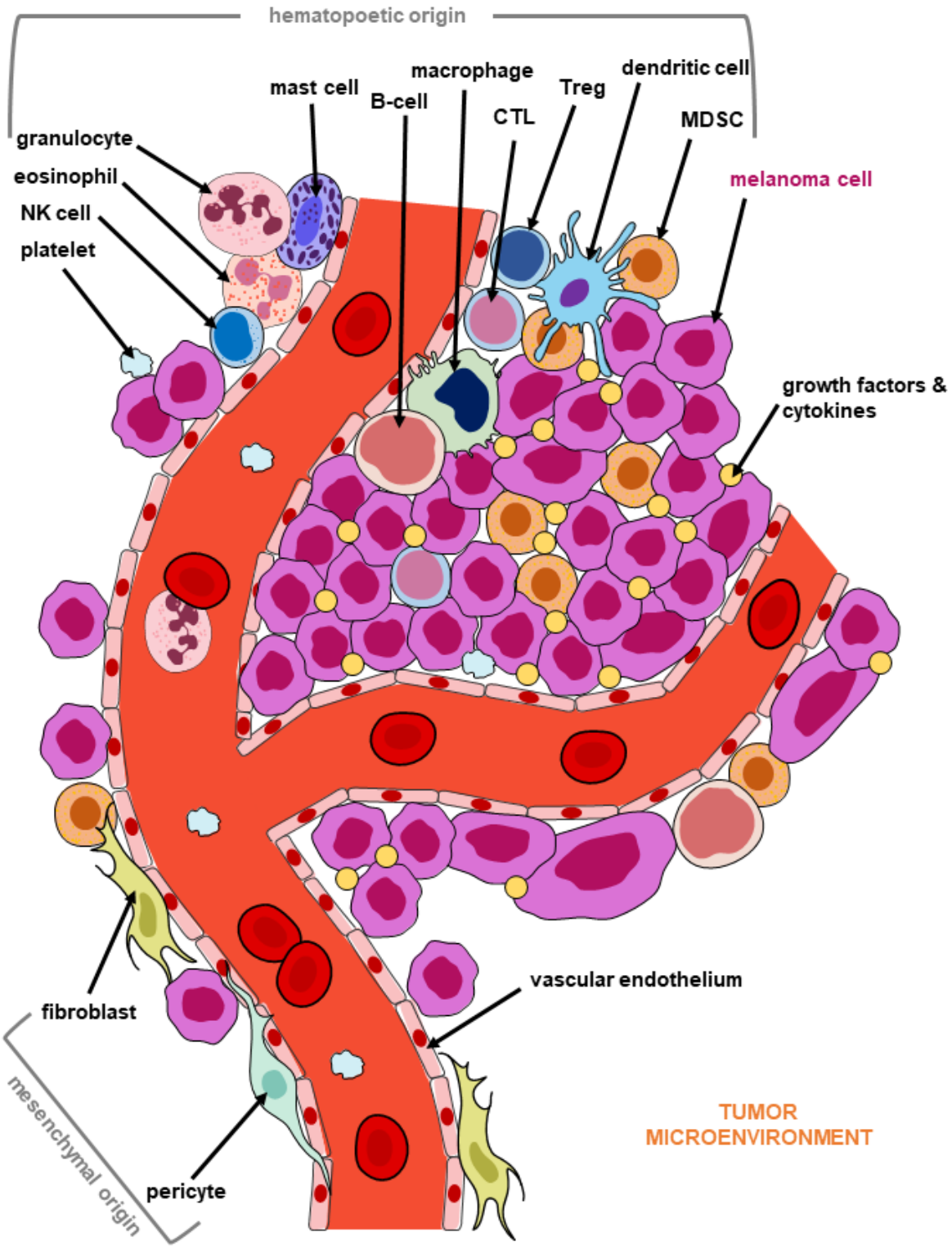

Figure 9. *The tumor microenvironment and associated cell types.* Melanoma cells form a "premetastatic niche" that helps them grow and later disseminate. Melanoma cells evolve to interact with or evade TME cell types for an advantageous outcome. This image was adapted from Kerkar and Restifo, 2012. This figure was generated by using images modified from *Servier Medical Art* (https://smart.servier.com/). Abbreviations: CTL = cytotoxic T-cell; MDSC = myeloid-derived suppressor cell; NK cell = natural killer cell; Treg = T-regulatory cell.

1.2. THERAPEUTIC STRATEGIES AGAINST MELANOMA

Most patients with newly-diagnosed melanoma lesions have early-stage disease. Luckily, surgical removal of the primary tumor is curative in most cases (Ross and Gershenwald, 2011). However, a significant number of patients suffer from cancer recurrence months or years later. Moreover, approximately 10 % of melanomas are diagnosed at an advanced (already metastatic) stage which cannot be fully surgically resected. One third of patients with stage IV melanoma have visceral and brain involvement at diagnosis, with a poor prognosis and low probability of sustained treatment response (Leonardi et al., 2018).

Melanoma is known for its resistance to traditional cancer treatments such as chemotherapy and radiotherapy; however, before 1995, patients with metastatic melanoma had no other treatment options. In 1995, interferon treatment was approved but only as adjuvant therapy for patients who underwent surgery to remove advanced melanoma tumors. Three years later, the FDA certified interleukin-2 (IL-2) as systemic therapy to treat patients with stage III-IV melanoma. The approval of IL-2 provided improved results but had less than 15 % 5-year survival rates following treatment initiation (Ko, 2017). Luckily, advanced melanoma treatment has significantly improved since 2011, following decades of unfavorable clinical trials and failed therapy attempts with traditional surgical and chemotherapeutic approaches (Ko, 2017; Leonardi et al., 2018).

Vemurafenib was FDA-approved in 2011 as the first 'mutation-specific' treatment for melanoma, with an impressive objective response rate of over 50 % in BRAF-mutant patients (Chapman et al., 2011). The anti-CTLA4 antibody Ipilimumab was approved by the FDA in the same year; patients with previously treated, unresectable advanced melanomas displayed an overall response rate of up to 25 % two years after receiving Ipilimumab treatment (Fellner, 2012). In 2013, trametinib (a MEK inhibitor) and dabrafenib (a BRAF*V600* inhibitor) were approved in the clinics for patients with stage III-IV melanoma. Since proven more effective together, dabrafenib and trametinib were certified by the FDA one year later to be administered as a combination therapy. In 2014, two more anti-melanoma therapies, Nivolumab and Pembrolizumab (both anti-PD-1 inhibitors), were approved. One year later, more tools were added to the anti-melanoma fight with the combination treatment of vemurafenib and cobimetinib (BRAF*V600E* + MEK inhibitor therapy). In the same year, the combination therapy of Nivolumab and Ipilimumab as well as T-VEC (local immunotherapy treatment) were FDA-approved, with the latter allowed to be used only for early-stage melanomas. In 2018, Encorafenib (BRAF inhibitor) and Binimetinib (MEK inhibitor) were certified to be administered together in patients with BRAF*V600E* and -*V600K* mutant melanomas. Recently,

the drug trio of Atezolizumab + Vemurafenib + Cobimetinib, based on the combination of anti-PD-1/PD-L1 immunotherapy along with BRAF*V600E* and MEK inhibitor therapy were authorized for the treatment of melanoma patients with advanced disease (Dimitriou et al., 2021; Melanoma Research Alliance, 2021). A timeline of the evolution of melanoma treatment is displayed in **Figure 10.**

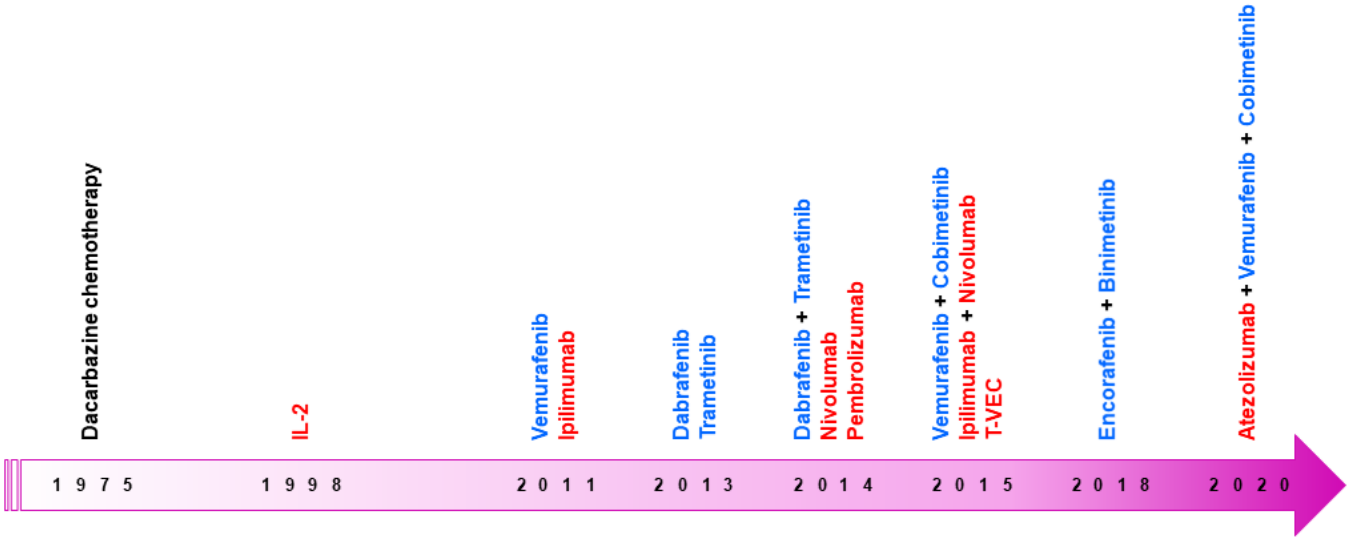

Figure 10. *The evolution of anti-melanoma therapy for advanced disease.* Before 1998, when IL-2 was approved as anti-melanoma treatment in the clinics, patients were administered chemotherapy. Following a gap of 13 years without any new anti-melanoma therapy approval, in 2011 vemurafenib was certified by the FDA as the first targeted therapy drug. Continuous research and clinical trials led to the spike in approvals of numerous targeted- and immunotherapies thereafter. Immunotherapy treatments are shown in red and targeted therapy drugs in blue. Abbreviations: IL-2 = interleukin-2; T-VEC = talimogene laherparepvec.

Compared to kinase inhibitor therapies, anti-PD-1 antibodies and, to a lower degree anti-CTLA4 agents, provide more durable response rates, but this does not apply to all melanoma patients (Leonardi et al., 2018). James P. Allison and Tasuku Honjo won the 2018 Nobel Prize of Physiology or Medicine for this impactful research on PD-1 and CTLA-4 immune checkpoints (Han et al., 2020). Based on their discoveries, new therapeutic strategies (mentioned above) now help more melanoma patients survive long-term (Passarelli et al., 2017). Neo-adjuvant immunotherapies (in which therapy is administered before surgery) managing bulky but resectable melanomas are also emerging and have shown favorable response rates (Versluis et al., 2020).

In BRAF-mutant melanomas, a justifiable approach has been taken to use BRAF/MEK inhibitors in combination (Leonardi et al., 2018). This approach targets the MAPK pathway at multiple levels, reducing chances of pathway reactivation (Broman et al., 2019; Smalley, 2010).

However, patients treated with such inhibitors can suffer from cancer relapses due to intrinsic or acquired resistance (Watson et al., 2018).

Due to advances in melanoma research over the past two decades, chemo- and radiotherapy are now considered second-line treatment options, making immunotherapy and kinase inhibitors the backbone of systemic therapy for melanoma patients with advanced disease (Leonardi et al., 2018). However, metastatic melanoma remains a deadly disease for many patients and treatment resistance can occur regardless of the treatment strategy for some patients (Lionarons et al., 2019). Furthermore, to this day, there is no clear clinical therapeutic approach for certain melanoma subtypes such as patients with mutant NRAS melanomas for instance (Randic et al., 2021).

1.3. BRAIN METASTASES

Brain metastasis (BM), i.e. the spread of cancer to the brain, can occur in the brain parenchyma or the meninges and is most prevalent in melanoma, lung and breast cancer patients (Steeg et al., 2011; Valiente et al., 2020). Nearly 20 % of cancer patients will develop BMs, which can be indicated by symptoms such as cognitive impairment, cranial neuropathy, loss of motor and sensory function and seizures (Brown et al., 2017; Steeg et al., 2011). The development of BM worsens patient quality of life and survival; additionally, it is lethal in up to 50 % of the cases. The incidence of BMs has increased in the past years, partially due to improved imaging technology (Valiente et al., 2020).

Tumor cells about to invade the brain must traverse the blood-brain barrier (BBB) first. The BBB protects the brain by hampering the inflow of harmful compounds from the blood; however, cancer cells compromise its integrity by modifying it to a blood-tumor barrier (BTB) with non-uniform permeability. Hence, metastatic tumor cells colonize the brain where they cooperate with activated astrocytes, microglia and other brain cells (Valiente et al., 2020). The tumor cells that migrate through the BBB typically settle alongside the blood vessels where they start proliferating; however, some individual cells stay dormant and adapt the brain microenvironment to their needs before they grow into full BMs (Abate-Daga et al., 2018).

The brain TME consists of cell types that contribute to the brain tumor biology in unique ways. These cells include TAMs, microglia (macrophage-like cells that are the primary immune cells of the central nervous system), DCs, neutrophils, lymphocytes (including Treg cells), oligodendrocytes (the myelinating cells of the central nervous system) and astrocytes (Quail and Joyce, 2017). Astrocytes, unique players of the central nervous system (CNS), are specialized glial cells that provide structural support for neurons (Quail and Joyce, 2017; Steeg

et al., 2011). These brain cells are particularly important because they form functional gap junctions with tumor cells through which they transfer ions and signaling molecules that stimulate cancer cell survival and growth (Quail and Joyce, 2017). A simplified illustration of the brain TME is shown in **Figure 11**.

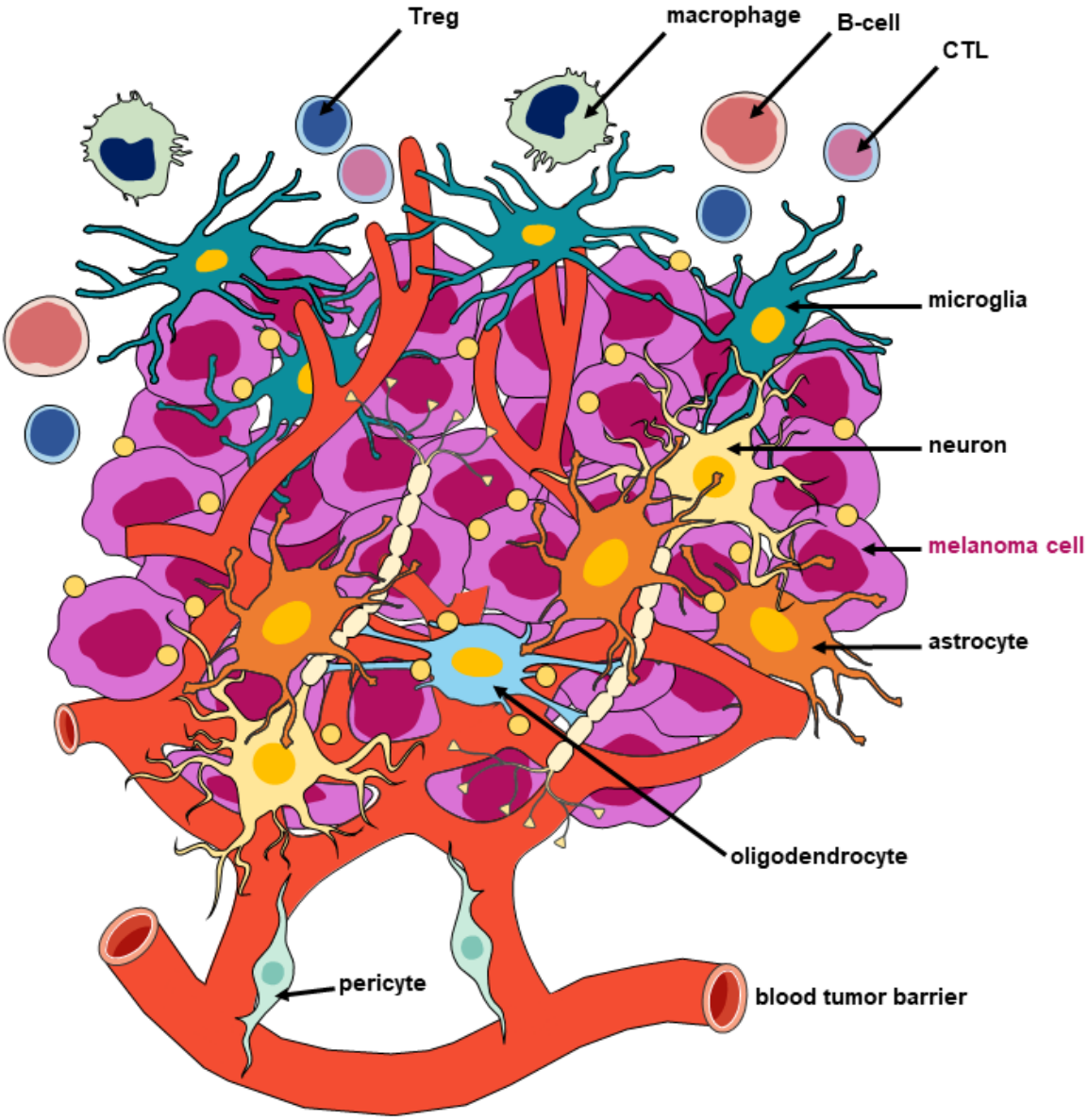

Figure 11. *The brain tumor microenvironment.* Tumor cells grow within the normal brain parenchyma. Cancer cells interact with various brain cells, including astrocytes, neurons, oligodendrocytes or microglia. Growth factors released by these cells are drawn as small circles. This image was adapted from Khamis et al., 2021 and was generated by using images modified from *Servier Medical Art* (https://smart.servier.com/). Abbreviations: CTL = cytotoxic T-cell; Treg = T-regulatory cell.

BM therapy includes surgery, stereotactic radiotherapy and whole-brain radiotherapy (Valiente et al., 2020). These anti-BM treatments unfortunately are mostly palliative. Surgery is a viable option only when the lesions are few, localized and in accessible parts of the brain (Steeg et al., 2011). Since the 1950s, whole-brain radiotherapy (WBRT) has been extensively used for

treating advanced BMs. Previously, the toxicities caused by WBRT were given little attention because patients suffering from BM had an unfavorable prognosis. But nowadays, due to improvements in BM detection and therapy, there have been rising concerns about toxicities associated with WBRT, such as cognitive deterioration (Brown et al., 2017). Stereotactic radiosurgery (SRS) on the other hand is an alternative to traditional surgery in which selected areas of tissue are destroyed using ionizing radiation. SRS can be used to treat lesions located in surgically inaccessible regions; however, retrospectively, SRS has a comparable outcome to traditional surgery (Steeg et al., 2011).

Although not a research focus in the past, nowadays the BM field has become more attractive for basic and clinical scientists since systemic disease is more manageable (Valiente et al., 2020). Extended studies that take into account the unique biological identity of BM could divulge novel therapeutic approaches and improve patients' outcome and quality of life (Boire et al., 2020; Valiente et al., 2020).

1.4. MELANOMA BRAIN METASTASIS

1.4.1. Epidemiology and molecular characteristics

Cutaneous melanoma is one of the leading causes of cancer-related deaths due to its metastatic capacity (Gener Lahav et al., 2019; Leonardi et al., 2018). One of the deadliest and most frequent complications of stage IV melanoma is metastasis to the brain, identified in up to 80 % of patients at autopsy; only two thirds of these patients will have been diagnosed with melanoma-associated brain metastasis (MBM) before death (Rebecca et al., 2020; Steeg et al., 2011).

Melanoma has the ability to metastasize to any part of the brain, with the cerebrum, cerebellum, and pons being the most prevalent regions (Cohen et al., 2019). There are multiple theories describing the route of the skin malignancy up to the brain. Most likely, MBMs originate from tumor cells from the primary tumor or from extracranial metastases which manage to penetrate the BBB and circulate in the brain microvasculature (Achrol et al., 2019; Chen and Davies, 2012).

Similar to other metastatic cancer cells, melanoma cells acquire a distinctive phenotype in order to propagate to the brain and thrivingly grow there (Haueis et al., 2017; Redmer, 2018). This change in phenotype is not necessarily due to genetic alterations but rather due to the interplay between melanoma metastatic cells and the brain microenvironment (Redmer, 2018). However, there are studies that showed that MBM-specific genetic prerequisites include BRAF or RAS mutations and loss of PTEN (Adler et al., 2017; Bucheit et al., 2014). Interestingly, another

study reported that, while PTEN is expressed at normal levels in primary tumor cells, its expression is lost after spreading to the brain, but not to other organs, and that this is a reversible mechanism that relies on the interaction between metastatic cells and astrocytes (Zhang et al., 2015). Such findings are not confirmed yet and insufficient samples have been interrogated so far to confirm the presence or absence of clear MBM-specific genes.

The high impact of the brain microenvironment on cancer biology was previously demonstrated in a study by Kim and colleagues; analyses of gene expression data revealed that the brain microenvironment induces complete gene expression reprogramming of metastasized lung and breast cancer cells, culminating in a gain of neuronal cell characteristics and neurogenesis mimicking (Kim et al., 2011). Additionally, another study showed that breast cancer cells acquired a neuronal-like phenotype when they metastasized to the brain (Neman et al., 2014). Melanoma cells could be prone to homing to the brain, which is no surprise given that melanocytes, the precursors of melanoma cells, are ancestrally related to neurons (Redmer, 2018).

Astrocytes, key cellular components of the brain TME, were shown to exert a pro-metastatic effect when they interacted with MBM cells (Zou et al., 2019). In addition, *in vivo* studies using PDX models showed that the ability of human-derived MBM cells to metastasize to the brain in immunocompromised mice is diminished following long-term *in vitro* culture, suggesting once again the importance of the interplay between cancer cells and the brain TME in maintaining the pro-brain metastatic ability (Valiente et al., 2020).

The PI3K/AKT/mTOR pathway is reportedly one of the signaling pathways most commonly involved in MBM development (Westphal et al., 2017). This was first observed by Davies and colleagues, who reported high phosphorylated AKT and lower PTEN expression in MBMs compared with metastases of the lung and liver (Davies et al., 2009). Similar to this, another study demonstrated that in MBM patient samples, compared to extracranial melanoma metastases from the same patients, phosphorylated AKT was overexpressed (Niessner et al., 2013). Additionally, MBM development was noticed in 80 % of mice when AKT1 was overexpressed and PTEN was silenced (Cho et al., 2015). Further supporting this point, another *in vivo* study demonstrated that mice harboring AKT1*E17K* mutated tumors (that can cause constant AKT activation) had the highest incidence of MBMs; these tumors also displayed enhanced levels of phosphorylated FAK (Kircher et al., 2019).

Other studies have shown that the MAPK pathway is also involved in MBM development. When comparing paired tissue samples from primary tumors and MBMs in 132 patients, the latter harbored higher BRAF and NRAS mutational burdens (Colombino et al., 2012). Moreover, the brain is hypothesized to be the most frequent new site of disease evolution in

BRAF-mutant patients without CNS involvement at baseline after receiving dabrafenib and trametinib as combination therapy (Long et al., 2016).

MBMs were proven to have other unique molecular characteristics as well. In a study where RNA sequencing of 88 MBMs and 42 patient-matched extracranial metastases was performed, significant immunosuppression and enrichment of OXPHOS in MBMs was identified; the authors suggest that the enrichment of OXPHOS in MBMs might contribute to their resistance to kinase inhibitor therapies (Fischer et al., 2019). Another research group who analyzed MBMs and primary cutaneous melanomas using next generation sequencing showed that MBMs display higher PD-L1 expression; interestingly, they also observed no difference in tumor mutation burden between lesion sites (In et al., 2020). Supporting this, RNA sequencing analyses performed by Garman and colleagues using MBM cells as well as other extracranial cells did not reveal MBM-specific genetic characteristics (Garman et al., 2017).

Taken all together, there is emerging information about the distinct biology and genetics of MBM, but also a considerable number of contradictory studies, pointing out the need for more attention to preclinical as well as clinical research in this field.

1.4.2. Therapeutic strategies against melanoma brain metastasis

Melanoma patients with BMs have a poor prognosis, with a median overall survival of 2.5-6 months (Redmer, 2018). Similar to other cancer types, first-line anti-MBM therapies include surgery and radiotherapy, while chemotherapy has demonstrated low efficacy in MBM patients (Glitza et al., 2016). Traditional surgery is an option only in cases of single lesions or multiple lesions localized in close proximity to one another. For a long time WBRT and corticosteroids were the standard treatment for patients with advanced MBM; currently, SRS is gradually replacing WBRT (Glitza Oliva et al., 2017).

Although the above-mentioned therapies remain important for the management of MBM, immunotherapies offer strong responses and come at a lower cost of neurocognitive impairment (Tawbi et al., 2018). Similar to extracranial melanomas, the first immunotherapeutic agent that showed efficacy in MBM patients was IL-2; however, the response rate was still lower in MBM patients than in patients with extracranial disease (Glitza Oliva et al., 2017). In addition, Ipilimumab administration in MBM patients showed positive response rates, comparable to its administration in patients suffering from extracranial lesions. Anti-PD-1 therapy showed durable response rates of nearly 20 % in MBM patients. Importantly, the combination of anti-CTLA-4 and anti-PD-1 therapy induced responses at a remarkable rate of 55 % (26 % of patients had a complete response and 30 % a partial response in the brain) (Tawbi et al., 2018).

Among patients with BRAF-mutant MBM, treatment with vemurafenib or dabrafenib as monotherapies led to response rates of 20 % and up to 40 %, respectively (Long et al., 2012; McArthur et al., 2017). Moreover, the combination treatment of dabrafenib and trametinib showed an improved response rate of nearly 55 %, compared to monotherapy administration (Davies et al., 2017; Suh et al., 2020). While BRAF/MEK inhibitors rapidly achieve disease control in most patients, most of them ultimately develop resistance to these drugs. Furthermore, some MBM patients do not respond to targeted therapy or immunotherapies, one reason being the potential difficulty of therapeutics to penetrate the modified BTB (Redmer, 2018).

Finally, because the PI3K/AKT/mTOR pathway appears to play a major role in the development of MBM (see section **1.1.4.2.**), inhibitors of this pathway, such as BKM120 or MK-2206, are also being investigated in clinical trials for MBM (Westphal et al., 2017).

Even though research on the topic of MBM is ongoing, our understanding of MBM is still incomplete and many patients still succumb to the disease even if they initially respond to current therapies. Accordingly, studies taking into consideration both melanoma and brain biology are needed to overcome therapeutic gaps.

1.5. AIMS OF THESIS

Melanoma is a highly heterogeneous type of skin cancer that has a great propensity to metastasize to the brain with serious consequences for patients. Current therapies have shown some intracranial activity, but responses in the brain are still below that observed for extracranial lesions and many patients still succumb to advanced disease. Clinically, there is a pressing need for new therapeutic approaches and a better understanding of MBMs. Few human-based preclinical models are available for such scientific studies; thus, the development and characterization of new MBM research models is highly needed.

The main goal of this study was to identify melanoma brain lesion-specific biological processes and novel therapeutic targets to improve melanoma patients' survival and quality of life. To achieve this, the following specific aims were addressed:

1) *Identify novel signaling mechanisms specific to MBM*;

2) *Determine the functional role of brain-specific melanoma signals and their therapeutic potential*;

3) *Understand the plasticity of MBM cells in different microenvironments, including the brain.*

2. MATERIALS & METHODS

2.1. MATERIALS

2.1.1. Chemicals

Table 1. Inhibitors, activators, growth factors, chemicals, redox and ferroptosis agents

Chemical	Company	Product number	Purpose/function
BSA	Sigma-Aldrich	SLBV4989	protein concentration standard; membrane blocking solution (WB)
BSO	Sigma-Aldrich	B2515	ferroptosis activator
BKM120	Selleckchem	SEL-S2247-10MG	PI3K inhibitor
Crystal violet	Sigma-Aldrich	61135-25G	for cell staining
DMSO	Sigma-Aldrich	D2650-100ML	drug preparation
DTT	Sigma-Aldrich	D 0632	redox agent
EDTA	Applichem	A2937,0500	chelation, protease inhibitor
EHop-016	Tocris Bioscience	6248	RAC inhibitor
EHT 1864	Selleckchem	S7482	RAC inhibitor
Erastin	Sigma-Aldrich	E7781	ferroptosis activator
Ferrostatin-1	Selleckchem	S7243	ferroptosis inhibitor
Glucose	Applichem	A1422	media supplement
Glutamine	Applichem/ Sigma-Aldrich	A-3704/G7513	media supplement
H_2O_2 30 %	Sigma-Aldrich	H1009-500ML	redox agent
IGF-1	Sigma-Aldrich	I3769-50UG	hormone
Insulin, human	Sigma-Aldrich	I9278	hormone
Lipofectamine® 2000	Invitrogen	11668027	transfection reagent
MitoTEMPO	Sigma-Aldrich	SML0737	redox agent
$NaHCO_3$ 7.5 %	Sigma-Aldrich	S8761-100ML	pH adjustment of collagen I mix
NAC	Sigma-Aldrich	A9165/A0150000	redox agent
NSC23766	Selleckchem	SEL-S8031-10MM	RAC1 inhibitor
NP-40	Sigma-Aldrich	74385-1L	nonionic detergent used for WB
PFA	Sigma-Aldrich	P6148	for cell fixation
GDC-0941	Selleckchem	SEL-S1065-10MM	PI3K inhibitor
Polybrene	Sigma-Aldrich	TR-1003	infection/transfection reagent
Puromycin dihydrochloride	Millipore®	540411-25	antibiotic, protein synthesis inhibitor; used for selection and maintenance of RAC1 knockdown cells
Rapamycin	Selleckchem	SEL-S1039-10MM	mTOR inhibitor
RSL3	Selleckchem	S8155	ferroptosis activator
Trametinib	Selleckchem	S2673	MEK inhibitor
Vemurafenib	Selleckchem	SEL-S1267-10MM	BRAF*V600E* inhibitor

2.1.2. Solutions

2.1.2.1. SDS-PAGE and western blot solutions

- **Lysis buffer**

Table 2. Stock TGH buffer recipe

Chemical	Concentration	Company	Product number
Triton X-100	1 %	Carl Roth	3051.2
Glycerol	10 %	Sigma-Aldrich	G2025-500ML
NaCl	50 mM	AppliChem	A2942
HEPES	50 mM	Sigma-Aldrich	H-7523
EGTA	1 mM	Sigma-Aldrich	E3889-25G
Sodium deoxycholate	1 %	Sigma-Aldrich	30970-100G
ddH_2O	-	-	-

- **Lysis buffer**

Table 3. Same-day additives to the TGH lysis buffer

Chemical	Concentration	Company	Product number
Na_3VO_4	1 mM	Sigma-Aldrich	S6508-50G
PMSF	1 mM	Sigma-Aldrich	P7626
NaF	1 mM	Sigma-Aldrich	S7920-100G
PI[*]	1 X	Roche	1183617001

[*] PI: 10 X protease inhibitor (cOmplete™, Mini, EDTA-free Protease Inhibitor Cocktail)

- **Bradford reagent for protein determination**

Table 4. Bradford reagent recipe

Chemical	Concentration	Company	Product number
COOMASSIE® Brilliant Blue G 250	339 µM	Serva	35050
Ethanol	19.2 %	Carl Roth	P075.4
H_3PO_4	34 %	Carl Roth	9079.1
ddH_2O	-	-	-

- **SDS gel running buffer** (pH = 8.3)

Table 5. Running buffer recipe

Chemical	Concentration	Company	Product number
Tris	25 mM	Carl Roth	5429.3
Glycine	192 mM	AppliChem	A1067
SDS	0.1 %	Sigma-Aldrich	L-4509
ddH_2O	-	-	-

▪ **Protein transfer buffer**

Table 6. Transfer buffer recipe

Chemical	Concentration	Company	Product number
5 X transfer buffer[*]	1 X	Bio-Rad	1704270
Ethanol	20 %	Carl Roth	9065.2
ddH_2O	-	-	-

[*] Part of the Trans-Blot® Turbo™ RTA mini 0.2 µm nitrocellulose transfer kit, Bio-Rad, # 1704270.

▪ **Tris-buffered saline (TBS) (**pH = 7.6)

Table 7. TBS recipe

Chemical	Concentration	Company	Product number
Tris	50 mM	Carl Roth	5429.3
NaCl	150 mM	AppliChem	A2942
ddH_2O	-	-	-

The pH was adjusted with NaOH 2 M (Merck, # 109136) and HCl 1 M (Carl Roth, # K025.1).

▪ **TBS-T**

Table 8. TBS-T recipe

Chemical	Concentration	Company	Product number
Tris	50 mM	Carl Roth	5429.3
NaCl	150 mM	AppliChem	A2942
Tween® 20	0.1 %	Carl Roth	9127.1
ddH_2O	-	-	-

▪ **Stacking gel buffer** (pH = 6.8)

Table 9. Stacking gel buffer recipe

Chemical	Concentration	Company	Product number
Tris	0.5 M	Carl Roth	5429.3
SDS	0.4 %	Sigma-Aldrich	L-4509
ddH_2O	-	-	-

The pH was adjusted with NaOH 2 M (Merck, # 109136) or HCl 1 M (Carl Roth, # K025.1).

▪ **Separation gel buffer** (pH = 8.8)

Table 10. Separation gel buffer recipe

Chemical	Concentration	Company	Product number
Tris	1.5 M	Carl Roth	5429.3
SDS	0.4 %	Sigma-Aldrich	L-4509
ddH_2O	-	-	-

The pH was adjusted with NaOH 2 M (Merck, # 109136) or HCl 1 M (Carl Roth, # K025.1).

▪ **Stacking gel**

Table 11. Stacking gel recipe

Chemical	Concentration	Company	Product number
SG buffer	3 X	-	-
Acrylamide	5 %	Carl Roth	248272357
APS	0.075 %	Sigma-Aldrich	A3678
TEMED	6.67 M	Sigma-Aldrich	T7024
ddH_2O	-	-	-

▪ **Separation gel**

Table 12 A. Separation gel recipe for high molecular weight proteins

Chemical	Concentration	Company	Product number
SG buffer	3 X	-	-
Acrylamide	7 %	Carl Roth	248272357
APS	0.075 %	Sigma-Aldrich	A3678
TEMED	6.67 M	Sigma-Aldrich	T7024
ddH_2O	-	-	-

Table 12 B. Separation gel recipe for mixed molecular weight proteins

Chemical	Concentration	Company	Product number
SG buffer	3 X	-	-
Acrylamide	10 %	Carl Roth	248272357
APS	0.075 %	Sigma-Aldrich	A3678
TEMED	6.67 M	Sigma-Aldrich	T7024
ddH_2O	-	-	-

Table 12 C. Separation gel recipe for low molecular weight proteins

Chemical	Concentration	Company	Product number
SG buffer	3 X	-	-
Acrylamide	12 %	Carl Roth	248272357
APS	0.075 %	Sigma-Aldrich	A3678
TEMED	6.67 M	Sigma-Aldrich	T7024
ddH_2O	-	-	-

▪ **4 X Lämmli buffer** (Bio-Rad, # 1610747), mixed 1:10 with **β-mercaptoethanol** (Gibco, # 1985-023)

▪ **Blocking buffer** = 5 % BSA (Sigma-Aldrich, # SLBV4989) in TBS

▪ **Ready-to-use 1 X DPBS** (Gibco, # 14190-094)

▪ **Size standards**: *Precision Plus Protein™ Dual Color Standard* (Bio-Rad, # 161-0374).

2.1.2.2. Immunofluorescence solutions and media

Table 13. Solutions and media used for immunofluorescence

Solution	Composition	Purpose	Company and product number
10 X PBS (pH = 7.4)	NaCl 1.37 M KCl 27 mM Na_2HPO_4 100 mM KH_2PO_4 18 mM	stock solution	NaCl (AppliChem, # A2942) KCl (AppliChem, # A2939,0500) Na_2HPO_4 (Merck, # 6580) KH_2PO_4 (Merck, # 104877)
PBS^{++}	PBS 1 mM $MgCl_2$ 0.1 mM $CaCl_2$	washing	$MgCl_2$ (AppliChem, # A1036) $CaCl_2$ (Carl Roth, # 5239.1)
4 % PFA	PBS^{++} 4 % PFA	fixation	PFA (Sigma-Aldrich, # P6148)
50 mM NH_4Cl	PBS^{++} 50 mM NH_4Cl	quenching	NH_4Cl (AppliChem, # A3661)
PBS^{T++}	PBS^{++} 0.1 % Triton X-100	permeabilization; washing	Triton X-100 (Carl Roth, # 3051.2)
1 % BSA	PBS^{T++} 1 % BSA	blocking	BSA (Sigma-Aldrich, # SLBV4989)
0.2 % BSA	PBS^{T++} 0.2 % BSA	antibody dilution	
VECTASHIELD®	1.5 µg/ml DAPI	mounting medium	Vector Laboratories, # H-1200-10

The pH was adjusted with NaOH 2 M (Merck, # 109136) or HCl 1 M (Carl Roth, # K025.1).

2.1.2.3. Solutions used for cell washing, fixing and staining

2.1.2.3.1. Solutions used for cell washing

▪ **10 X PBS stock solution**

Diluted before use to 1 X PBS with ddH_2O.

Table 14. 10 X PBS recipe

Chemical	Concentration	Company	Product number
NaCl	1.37 M	AppliChem	A2942
KCl	27 mM	AppliChem	A2939,0500
Na_2HPO_4	100 mM	Merck	6580
KH_2PO_4	18 mM	Merck	104877
ddH_2O	-	-	-

The pH was adjusted to 7.4 with HCl 1 M (Carl Roth, # K025.1).

▪ **Ready-to-use 1 X DPBS (**Gibco, # 14190-094)

2.1.2.3.2. Solutions used for cell fixing

▪ ***PFA 16 %*** (pH = 7.2)

Diluted before use to 4 % PFA with DPBS.

Table 15. PFA 16 % solution recipe

Chemical	Concentration	Company	Product number
PFA	16 %	Sigma-Aldrich	P6148
PBS	1 X	-	-
NaOH	1 mM	Merck	109136
ddH_2O	-	-	-

The pH was adjusted with NaOH 2M (Merck, # 109136) or HCl 1M (Carl Roth, # K025.1).

2.1.2.3.3. Solutions used for cell staining

▪ ***Crystal violet 0.05 %***

Table 16. Crystal violet 0.05 % solution recipe

Chemical	Concentration	Company	Product number
Crystal violet	0.05 %	Sigma-Aldrich	P6148
Formaldehyde	1 %	Carl Roth	4980.1
PBS	1 X	Gibco	14190-094
Methanol	1 %	Carl Roth	4627.5
ddH_2O	-	-	-

▪ ***Live/Dead™ Viability/Cytotoxicity Kit*** (Thermo Fisher Scientific, # L3224). The kit is comprised of 4 mM calcein-AM and 2 mM EthD-1. For 3D spheroid staining, a solution of DPBS containing 2 µM calcein-AM (for the staining of live cells) and 4 µM EthD-1 (for the staining of dead cells) was prepared fresh before each use.

▪ ***Hoechst 33342 10 mg/ml*** (Thermo Fisher Scientific, # H3570). Prepared fresh before each use as 0.5 µg/ml solution in DPBS.

2.1.3. Antibodies used for immunoblotting and immunofluorescence

2.1.3.1. Primary antibodies

All primary antibodies used for western blot (WB) and immunofluorescence (IF) are listed in Table 17.

Table 17. List of primary antibodies used for WB and IF (continued on next page)

Antibody	Clonality	Size	Species	Company	Product number	Working dilution
4E-BP1	polyclonal	15 to 20 kDa	Rabbit	Cell Signaling Technology	9452S	1:1,000 (WB)
Phospho-4E-BP1 (T37/46)	monoclonal	15 to 20 kDa	Rabbit	Cell Signaling Technology	2855S	1:1,000 (WB)
β-actin	monoclonal	45 kDa	Mouse	Sigma-Aldrich	A5441	1:10,000 (WB)
AKT	polyclonal	60 kDa	Rabbit	Cell Signaling Technology	4685S	1:1,000 (WB)
Phospho-AKT (S473)	monoclonal	60 kDa	Rabbit	Cell Signaling Technology	4060S	1:500 (WB)
Calnexin	polyclonal	98 kDa	Rabbit	Enzo	ADI-SPA-860-F	1:1,000 (WB)
CDC42	monoclonal	21 kDa	Mouse	Santa Cruz	sc-8401	1:1,000 (WB)
FAK	polyclonal	125 kDa	Rabbit	Cell Signaling Technology	3285S	1:1,000 (WB)
Phospho-FAK (Y576/577)	polyclonal	125 kDa	Rabbit	Cell Signaling Technology	3281S	1:1,000 (WB)
GAPDH	monoclonal	37 kDa	Rabbit	Cell Signaling Technology	2118S	1:1,000 (WB)
Histone H3	monoclonal	17 kDa	Rabbit	Cell Signaling Technology	4499S	1:1,000 (WB)
HSP90	polyclonal	90 kDa	Rabbit	Cell Signaling Technology	4874S	1:1,000 (WB)
JNK1	monoclonal	46,54 kDa	Mouse	Cell Signaling Technology	3708S	1:1,000 (WB)
Phospho-SAPK/JNK1 (T183/Y185)	monoclonal	46,54 kDa	Rabbit	Cell Signaling Technology	4668S	1:1,000 (WB)
p44/42 MAPK (Erk1/2)	monoclonal	42,44 kDa	Rabbit	Cell Signaling Technology	9102S	1:1,000 (WB)
Phospho-p44/42 MAPK (Erk1/2) (T202/Y204)	polyclonal	42,44 kDa	Rabbit	Cell Signaling Technology	4370S	1:1,000 (WB)
Melan-A	monoclonal	22 kDa	Mouse	Thermo Fisher Scientific	MA5-14168	1:100 (IF)
mTOR	monoclonal	289 kDa	Rabbit	Cell Signaling Technology	2983S	1:1,000 (WB)
NF-κB p65	monoclonal	65 kDa	Rabbit	Cell Signaling Technology	8242S	1:1,000 (WB)
Phospho-NF-κB p65 (S536)	monoclonal	65 kDa	Rabbit	Cell Signaling Technology	3033S	1:500 (WB)
p70 S6 Kinase	monoclonal	70,85 kDa	Rabbit	Cell Signaling Technology	2708S	1:1,000 (WB)
Phospho-p70 S6 kinase (T389)	monoclonal	70,85 kDa	Rabbit	Cell Signaling Technology	9234S	1:500 (WB)
PAK1/2/3	polyclonal	61 kDa (PAK2), 68 kDa (PAK1/3)	Rabbit	Cell Signaling Technology	2604S	1:1,000 (WB)
Phospho-PAK1 (S199/204)/PAK2 (S192/197)	polyclonal	61 to 67 kDa (PAK2), 68 to 74 kDa (PAK1/3)	Rabbit	Cell Signaling Technology	2605S	1:500 (WB)

PARP	polyclonal	89 kDa cleaved; 116 kDa total	Rabbit	Cell Signaling Technology	9542S	1:1,000 (WB)
PD-L1	monoclonal	40-50 kDa	Rabbit	Cell Signaling Technology	13684S	1:1,000 (WB)
RAC1	monoclonal	21 kDa	Mouse	Abcam	ab33186	1:1,000 (WB); 1:100 (IF)
RAC1/CDC42	polyclonal	21 kDa	Rabbit	Cell Signaling Technology	4651S	1:1,000 (WB)
RAC3	monoclonal	21 kDa	Rabbit	Abcam	ab129062	1:1,000 (WB)
RAS	polyclonal	21 kDa	Rabbit	Cell Signaling Technology	3965S	1:1,000 (WB)
RPTOR	monoclonal	150 kDa	Rabbit	Cell Signaling Technology	2280T	1:1,000 (WB)
RhoA	monoclonal	21 kDa	Rabbit	Cell Signaling Technology	2117S	1:1,000 (WB)
RICTOR	monoclonal	200 kDa	Rabbit	Cell Signaling Technology	2114T	1:1,000 (WB)
SRC	monoclonal	60 kDa	Rabbit	Cell Signaling Technology	2109S	1:1,000 (WB)
Phospho-SRC (Y416)	monoclonal	60 kDa	Rabbit	Cell Signaling Technology	6943S	1:1,000 (WB)
β-Tubulin	polyclonal	50 kDa	Rabbit	Abcam	ab6046	1:500 (WB)

2.1.3.2. Secondary antibodies

Table 18. List of secondary antibodies used for WB and IF

Antibody	Company	Product number	Dilution
IRDye 680LT Donkey anti-Mouse	Li-Cor	926-68022	1:10,000 (WB)
IRDye 800CW Donkey anti-Rabbit	Li-Cor	926-32213	1:10,000 (WB)
anti-Mouse IgG (H+L) Highly Cross-Adsorbed Secondary Antibody, Alexa Fluor 488	Invitrogen	A-11029	1:100 (IF)

2.1.4. Oligonucleotides

- **Primers used for RT-qPCR**

Table 19. Primers used for RT-qPCR (indicated 5' to 3')

Transcript	Forward	Reverse	Company
NOX1	AATCCTTGGGTCAACATTGG	CCCATTGTCAAGAGGTGGTT	Qiagen
NOX2	TCACTTCCTCCACCAAAACC	CCCATTGTCAAGAGGTGGTT	
NOX3	GCCCAACTGGAACAATGAGT	ATGAACACCTCTGGGGTCAG	
NOX4	CTGGTGAATGCCCTCAACTT	GGCCAGGAACAGTTGTGAAG	
NOX5	ATCTGCTCCAGTTCCTGCAT	AACAAGATTCCAGGCACCAG	
TBP	CGGAGAGTTCTGGGATTGT	GGTTCGTGGCTCTCTTATC	

- **Additional nucleotides**

Table 20. Nucleotides used for cDNA synthesis

Nucleotide	Company	Product number
dNTP	Invitrogen	18109017
Oligo(dT)$_{12-18}$ primer	Invitrogen	18418012

2.1.5. Plasmids

Table 21. Plasmids

Plasmid	Provider	Product number
pMD2.G DNA	Addgene (D. Trono)	12259
psPAX2 DNA	Addgene (D. Trono)	12260
pLKO.1 sh scrambled (empty vector)	Addgene	1864

2.1.6. shRNAs

Table 22. Plasmid sequences used for RAC1 knockdown

Plasmid	Sequence	Company and product number
shRAC_1	CCGGCGCAAACAGATGTGTTCTTAACTCG AGTTAAGAACACATCTGTTTGCGTTTTT	Sigma-Aldrich (MISSION® shRNA), # TRC0000004871
shRAC1_2	CCGGCCTTCTTAACATCACTGTCTTCTCGA GAAGACAGTGATGTTAAGAAGGTTTTTG	Sigma-Aldrich (MISSION® shRNA), # TRC0000318432

2.1.7. Additional kits and reagents

Table 23. Kits and reagents

Kit or reagent	Company	Product number	Purpose
CellTiter-Blue® Cell Viability Assay	Promega	G8081	cell proliferation/viability
HiSpeed® Plasmid Maxi Kit	Qiagen	12663	plasmid preparation
Nucleospin™ RNA Plus Kit	Macherey-Nagel	740984.250	RNA isolation
Superscript™ IV Reverse Transcriptase Kit	Invitrogen	18090050	cDNA synthesis
GoTaq® qPCR Master Mix	Promega	A6002	RT-qPCR
Active RAC1 Pull-Down and Detection Kit	Thermo Fisher Scientific	16118	RAC1 pull-down assay
Trans-Blot® Turbo™ RTA Mini 0.2 µm Nitrocellulose Transfer Kit	Bio-Rad	1704270	WB transfer

2.1.8. Cell lines

2.1.8.1. Human melanoma cell lines

Table 24. Human melanoma cell lines used, grouped by melanoma brain metastasis (MBM) or non-brain melanoma metastasis (non-MBM) status, featuring key mutations as detected by RNA sequencing (Garman et al., 2017; Krepler et al., 2017)

Cell line	Stage	BRAF status	NRAS status	RAC1 status	Additional known gene mutations	Provider
WM793	VGP	*V600E*	WT	high gain copy number	*PTEN*	M. Herlyn *
1205Lu	lung met.	*V600E*	WT	high gain copy number	*PTEN*	M. Herlyn *
WM983B	inguinal node met.	*V600E*	WT	high gain copy number	*CDKN2A, TP53*	M. Herlyn *
WM3918	met.	WT	WT	N/A	*TERT*	M. Herlyn *
M230	brain met.	*V600K*	*Q61R*	N/A	*TERT*	M. Lotem **
M331	brain met.	*V600E*	WT	N/A	*MAP2K1, TP53, TERT*	M. Lotem **
M450	brain met.	WT	WT	N/A	*CDKN2A, NF1, TP53*	M. Lotem **
WM4237	brain met.	*V600E*	WT	N/A	*TP53, TERT*	M. Herlyn *
WM4265-2	brain met.	WT	*Q61K*	N/A	*PTEN, TP53, TERT*	M. Herlyn *

Abbreviations: VGP = vertical growth phase; met. = metastasis; WT = wild type; N/A = not available

[*] M. Herlyn is affiliated with The Wistar Institute, Philadelphia, USA.

[**] M. Lotem is affiliated with Hadassah Medical Center, Jerusalem, Israel.

The full lists of mutations (detected by RNA sequencing) of the aforementioned cell lines used for this study are publicly available in Garman et al., 2017 and Krepler et al., 2017 in the Supplemental Information section.

2.1.8.2. Stable knockdown human melanoma cell lines using shRNA

Table 25. RAC1 knockdown human melanoma cell lines used, grouped by origin of the parental cell line (non-MBM or MBM)

Cell line and label	Knockdown target	shRNA clone	Other remarks
WM983B sh control	-	empty vector	control cell line
WM983B shRAC1_1	RAC1	1	-
WM983B shRAC1_2	RAC1	2	-
WM3918 sh control	-	empty vector	control cell line
WM3918 shRAC1_1	RAC1	1	-
WM3918 shRAC1_2	RAC1	2	-
M331 sh control	-	empty vector	control cell line
M331 shRAC1_1	RAC1	1	-
M331 shRAC1_2	RAC1	2	-
WM4237 sh control	-	empty vector	control cell line
WM4237 shRAC1_1	RAC1	1	-
WM4237 shRAC1_2	RAC1	2	-

2.1.8.3. Additional cell lines

Table 26. Additional cell lines

Cell line	Provider
HEK293	American Type Culture Collection (ATCC®, # CRL-1573™)
HEK293TN (highly transfectable)	BioCat (LV900A-1-GVO-SBI)
Human astrocytes	C. Berndt (Heinrich-Heine University Düsseldorf, Germany)

2.1.9. Cell culture materials

2.1.9.1. Media and supplements used for standard cell culture

Table 27. Media and supplements used for cell maintenance

Media and supplements	Composition	Company	Product number
DMEM	10 % FCS	Gibco	41966-029
1 X DPBS	-	Gibco	14190-094
FCS	-	Sigma-Aldrich	F7524
EMEM	-	Sigma-Aldrich	M0275-500ML
Human astrocyte medium	1 % penicillin/streptomycin solution (ScienCell, # 0503); 2 % FCS (ScienCell # 0010); astrocyte growth supplement (ScienCell, # 1852)	ScienCell	1801
L-Glutamine	-	AppliChem/Sigma-Aldrich	A-3704/G7513-100ML
Opti-MEM®	-	Thermo Fisher Scientific	31985088
0.05 % Trypsin-EDTA	-	Thermo Fisher Scientific	25300-062

2.1.9.2. Support matrices used for 3D assays

Table 28. Media, matrices and supplements used for 3D assays and *in vivo* studies

Matrix	Concentration	Company	Product number
Difco™ noble agar	1.5 % in DPBS	BD Biosciences	214220
Collagen I, bovine, 5 mg/ml	2 mg/ml in DPBS	Gibco	A10644-01
Matrigel™ growth factor reduced basement membrane matrix	1:1 in culture medium	Corning	354230

2.1.10. Consumables

Laboratory consumables (pipettes, reagents and centrifuge tubes, cell culture flasks, microplates, dishes) were purchased from Sarstedt and Eppendorf, unless otherwise indicated in the respective method section.

All western blot consumables (running modules, electrophoresis chambers, casting frames and stands, glass casting plates, 1.5 mm 10- and 15-well combs) were purchased from Bio-Rad.

2.1.11. Laboratory devices

Table 29. Laboratory devices

Device	Manufacturer and model	Purpose
-80 °C freezer	*Thermo Fisher Scientific™ Forma™ Serie 88000*	frozen sample storage
Biosafety cabinet	*Thermo Fisher Scientific, # 51022482*	cell culture; sterile work
	BioWizard, Kojair Tech Oy	
Fume hood	*Waldner Variolab W90*	protection for work with vapors, dusts, gas
Incubator	*Binder CB160*	cell culture maintenance; cell incubation
	Heraeus BB16	
Water bath	*GFL® 1083*	media temperature control
Microscope	*Olympus CK30*	cell culture monitoring; cell counting
	Carl Zeiss Axiovert S100TV (featuring a Visitron CMOS camera)	imaging of migratory/invasive cells, 3D spheroids, crystal violet-stained cells
	Carl Zeiss Primovert Telaval 31	IF slide imaging
Centrifuge	*Heraeus™ Labofuge™ 400R, Thermo Fisher Scientific*	cell pellet formation
	Heraeus™ Megafuge™ 40R, Thermo Fisher Scientific	RT-qPCR plate spin-down
	Heraeus™ Fresco™ 17, Thermo Fisher Scientific	protein supernatant/pellet separation
	Eppendorf Centrifuge 5417	cell pellet formation
	Benchmark Scientific C1008-B MyFuge Mini Centrifuge	short spin-down
Microplate reader	*CLARIOstar, BMG LABTECH*	proliferation/viability/ adhesion assays
	Berthold, Mithras LB 940	protein determination
Rocking shaker	*Grant-Bio PMR-30 rocking shaker*	WB membrane incubation
Vortex mixer	*Vortex-Genie 2 mixer, Scientific Industries*	solution preparation, resuspension
pH meter	*WTW inoLab Multi 720*	pH adjustment
Balance	*Sartorius 1409 B MP7-2*	chemical weighing
	Sartorius LC 6215	
Heating block	*Eppendorf ThermoMixer® F2.0*	protein denaturation
Electrophoresis system	*Mini-PROTEAN Tetra Cell, Bio-Rad*	SDS-PAGE
Power supply	*PowerPac™ Basic Power Supply, Bio-Rad*	SDS-PAGE
Transfer system	*Trans-Blot® Turbo™ Transfer System, Bio-Rad*	protein transfer from gel to membrane
WB membrane imaging system	*Odyssey® CLx, LI-COR Biosciences*	WB membrane imaging
Thermal cycler	*C1000T™ Thermal Cycler, Bio-Rad*	cDNA amplification
qPCR instrument	*Stratagene Mx3000P qPCR System, Agilent*	RT-qPCR
Spectrophotometer	*Thermo Fisher Scientific™ NanoDrop 2000c*	determination of RNA concentration

2.1.12. Data acquisition and analysis software

Table 30. Software used for data acquisition and analysis

Software	Corresponding device
MARS Data Analysis Software	CLARIOstar
MikroWin 2000	Berthold, Mithras LB 940
MxPro qPCR software	Stratagene Mx3000P qPCR System
NanoDrop 2000	Thermo Fisher Scientific™ NanoDrop 2000c
VisiView® software	Carl Zeiss Axiovert S100TV (featuring a Visitron CMOS camera)
ZEN microscope software	Carl Zeiss Primovert Telaval 31
Image Studio™ Lite	Odyssey® CLx
Image J/Fiji	Personal desktop
GraphPad Prism 8	Personal desktop
InkScape	Personal desktop
Microsoft Excel 2016	Personal desktop
Microsoft PowerPoint 2016	Personal desktop
Microsoft Word 2016	Personal desktop

2.2. METHODS

2.2.1. Cell culture

All melanoma cell lines (**Tables 24** and **25**) and the HEK293 line were maintained in DMEM supplemented with 10 % FCS (**Table 26**) and were grown at 37 °C in 5 % CO_2. Human astrocytes were maintained in astrocyte media supplemented with 2 % FCS, astrocyte growth supplement and 1 % penicillin/streptomycin (**Table 27**). A 0.05 % trypsin-EDTA solution was used for cell dissociation. Knockdown of RAC1 in MBM and non-MBM cell lines was achieved and maintained using media regularly enriched with 4 µg/ml puromycin. A Neubauer haemocytometer (Marienfeld, # 0640130) was used to count the cells before experimentation.

2.2.2. Proliferation and viability assays

The proliferation and viability of melanoma cell lines were assessed using the following methods and conditions:

1) instrinsic proliferation:

To study the intrinsic proliferation rate of MBM (M230, M331, M450, WM4237, WM4265-2) and non-MBM lines (WM793, 1205Lu, WM983B, WM3918) in standard culture, 10,000 cells/well of each line were seeded in quadruplicate in 24-well plates over a period of 96 h. After 24, 48, 72 and 96 h, the cells were trypsinized and counted using a Neubauer haemocytometer and the Olympus CK30 inverted microscope. Counting was performed over three independent experiments (N = 3).

To determine the proliferation rate of MBM and non-MBM cells with RAC1 knockdown, the CellTiter-Blue® Cell Viability Assay kit was used. For this purpose, 5,000 cells/well of each cell line were seeded in 96-well plates in quadruplicate and allowed to grow for 72 h before the addition of the CellTiter-Blue® reagent. The ratio between the CellTiter-Blue® reagent and the culture media was 1:10. This reagent is based on resazurin, a dark violet dye that only viable cells can reduce to resorufin, which is pink and highly fluorescent ($579_{Ex}/584_{Em}$). Non-viable cells lose metabolic capacity, i.e. they do not reduce resazurin to resorufin; therefore, they do not generate a fluorescent signal. The cells were incubated with CellTiter-Blue® for 3 h prior to fluorescence measurement using the CLARIOstar plate reader. The fluorescent signal emitted by the RAC1 knockdown cells was compared to that emitted by the control (sh control) cells.

2) cell viability upon drug treatment:

Cell viability upon drug treatment was measured with the CellTiter-Blue® Cell Viability Assay described above, occasionally with the help of Adina Vultur. Shortly, 5,000 cells/well were seeded in 96-well plates and allowed to adhere for 24 h. After 24 h, cells were treated with different drug concentrations. Following 48 to 72 h, the CellTiter-Blue® solution was added and the cells were incubated for 3 h prior to fluorescence measurement.

BSO was diluted to 225 mM stock solution in water. All the other inhibitors, activators, redox agents, ferroptosis inducers and growth factors used were diluted to 10 mM stock solutions in DMSO.

3) proliferation upon drug treatment assessed via cell fixing and staining with crystal violet:

Another method used for assessing cell proliferation was via cell fixation with 4 % PFA, followed by cell staining with 0.05 % crystal violet. For this purpose, 40,000 cells/well were seeded in 6-well plates and were allowed to fully adhere for 24 h. After 24 h, cells were administered drugs or combination treatments as indicated. Following 72 h, drug-sensitive cells were washed out with 1 X DPBS and resistant-cells were fixed with 4 % PFA for 5 min. Cells were then stained with 0.05 % crystal violet solution for 30 min, washed with ddH_2O and allowed to fully dry before imaging with a 10 X objective of a Carl Zeiss Axiovert S100TV inverted microscope featuring a Visitron CMOS camera. Images were acquired using the VisiView® software and analyzed using ImageJ or Fiji.

2.2.3. Adhesion assay

The adhesion potential of MBM versus non-MBM cells was performed as described in Chen, 2012 and was adapted for use with melanoma cells. Shortly, cells (20,000/well in 96-well plates) were serum-deprived overnight; the next day, they were detached, resuspended in culture medium containing 0.1 % BSA, and incubated for 20 min at 37 °C. After two washes with culture medium without FCS, adhered cells were allowed to recover in culture medium supplemented with FCS for 4 h at 37 °C. The CellTiter-Blue® reagent was then added to the cells and the adhesion potential of melanoma cells was measured after 3 h using the CLARIOstar microplate reader.

2.2.4. Migration assay

The migration potential of MBM and non-MBM lines was assessed via transwell migration assay, as described in Zhang et al., 2019, with minor modifications. Briefly, 20,000 melanoma

cells suspended in 75 µl serum-free medium were seeded in 8 µm pore size inserts (Corning®, New York, USA) in 24-well plates. Cells were allowed to migrate for 24 h towards 72 h-old pre-conditioned media supplemented with 10 % FCS. A visual representation of the transwell migration assay is shown in **Figure 12**.

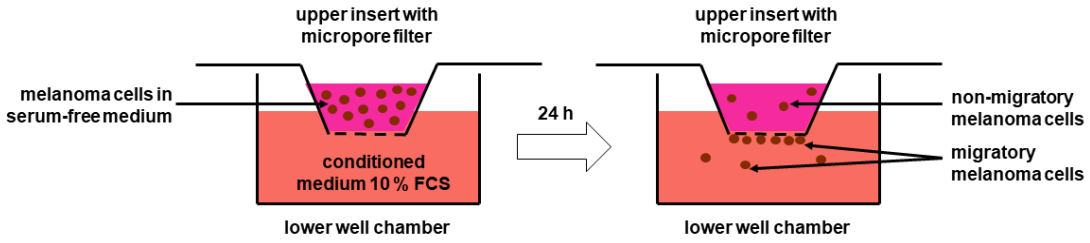

Figure 12. *A visual representation of the transwell migration assay.* Melanoma cells were seeded in serum-free media and made to invade for 24 h towards conditioned media supplemented with 10 % FCS. The migratory cells that attached to the bottoms of the insert and of the well were imaged and later quantitated.

Prior to imaging, non-migrated cells were removed from the upper side of the inserts with the help of a cotton swab and the remaining migrated cells were fixed with 4 % PFA for 15 min at room temperature and stained with 0.5 µg/ml Hoechst 33342 for 10 min at 37 °C. Fluorescent signals from migratory cells were examined with the help of a Carl Zeiss Axiovert S100TV inverted fluorescent microscope featuring a Visitron CMOS camera. Images were acquired using the VisiView® software and quantitated with ImageJ or Fiji.

2.2.5. Invasion assays

The invasion potential of MBM versus non-MBM cells was assessed by two different assays: the 3D transwell assay and the 3D matrix-supported spheroid assay.

2.2.5.1. 3D transwell invasion assay

Invasion via transwell assay was performed as described in Vultur et al., 2014 and Zhang et al., 2019, with minor modifications. A volume of 75 µl serum-free medium containing 250,000 cells of each MBM and non-MBM cell line were seeded in each insert of a 24-well plate featuring 8 µm pore size inserts. The inserts were previously coated with 40 µl of growth factor reduced Matrigel™ diluted 1:1 in serum-free DMEM. Cells from the upper insert were allowed to invade towards the bottom well chamber containing pre-conditioned DMEM (medium in which melanoma cells were grown for 72 h), supplemented with 20 % FCS for 24 h. A visual representation of the transwell invasion assay is shown in **Figure 13**.

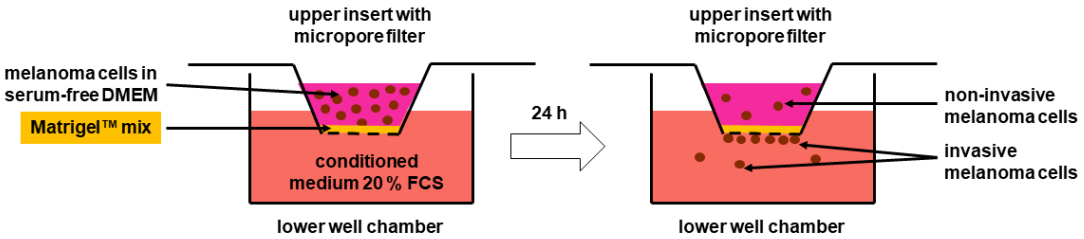

Figure 13. *A visual representation of the 3D transwell invasion assay.* Melanoma cells were seeded in serum-free media in inserts pre-coated with Matrigel™ mix and made to invade for 24 h towards conditioned media supplemented with 20 % FCS. The invasive cells that crossed to the bottoms of the insert and of the well were imaged and later quantitated.

Prior to imaging, non-invasive cells were removed from the upper side of the inserts with the help of a cotton swab and the remaining invasive cells were fixed with 4 % PFA for 15 min at room temperature and stained with 0.5 µg/ml Hoechst 33342 for 10 min at 37 °C. Fluorescent signals from the invasive cells were examined using a Carl Zeiss Axiovert S100TV inverted microscope featuring a Visitron CMOS camera. Images were acquired using the VisiView® software and quantitated with ImageJ or Fiji.

2.2.5.2. 3D melanoma spheroid assay

Melanoma spheroids were generated as described in Smalley et al., 2008. A volume of 100 µl medium containing 5,000 cells was seeded in each well of a 96-well plate on top of 50 µl of non-adherent solidified 1.5 % noble agar. After minimum 72 h, melanoma cells self-assembled and formed spheroids. The spheroids were manually harvested with the help of a 1000 µl pipette tip, they were embedded in a collagen I mix (300 µl/well) and were moved into new 24-well plates previously layered with 300 µl/well of the same acellular collagen I mix. The recipe for the collagen I mix is shown in **Table 31**.

Table 31. Collagen-I mix recipe

Media, matrix and supplement	Concentration
Collagen I, bovine	1.55 mg/ml
EMEM	1 X
FCS	10 %
L-Glutamine	1.68 mM
$NaHCO_3$	0.15 %

The spheroid-collagen-media mix was subsequently overlayed with fresh culture media with or without drug treatment. A visual representation of spheroid formation and embedding in collagen is shown in **Figure 14**.

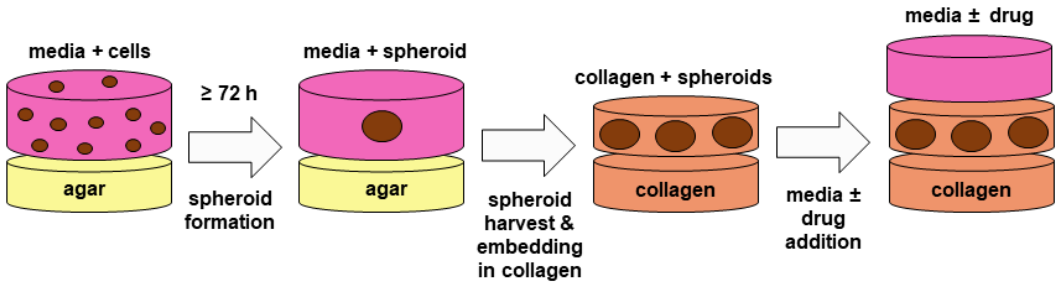

Figure 14. *A visual representation of the 3D melanoma assay.* Cells were seeded on 1.5 % agar; after 72 h or more spheroids were formed, harvested and embedded in collagen; underneath the collagen-spheroids mix a layer of acellular collagen was added and on top of it media with or without a drug or a combination treatment at a given concentration.

After 48-72 h (the end time point depended on the invasion potential of each cell line or on the potency of the applied treatments), the spheroids were stained with the Live/Dead™ Viability/Cytotoxicity Kit. This kit comprises a calcein-AM and an EthD-1 solution. Live cells possess intracellular esterase activity, determined by the enzymatic conversion of the non-fluorescent calcein-AM to the fluorescent calcein ($495_{Ex}/515_{Em}$). EthD-1 infiltrates cells with damaged membranes and undergoes an increase in fluorescence upon binding to nucleic acids, thus producing a red signal in dead cells ($495_{Ex}/635_{Em}$). In order to stain spheroids, a 500 µl DPBS solution containing 2 µM calcein-AM and 4 µM EthD-1 was prepared fresh before each use and was added on top of each spheroid-containing well (overlaying liquid medium was removed before dye addition). Spheroids were imaged using a Carl Zeiss Axiovert S100TV inverted microscope featuring a Visitron CMOS camera, GFP (green signal) and RFP (red signal) filters. Images were acquired using the VisiView® software and analyzed with ImageJ or Fiji. Quantitation of the spheroid invasion area was performed by measuring the total area covered by the cells of a given spheroid minus the core of each spheroid.

2.2.6. Determination of protein expression levels

2.2.6.1. Reverse phase protein array assay

The reverse phase protein array (RPPA) allows a fine detection and quantification of hundreds of total and post-translationally modified proteins in healthy and diseased cells. With this technique, the expression and activity status of key signaling pathways in cells can be investigated (Creighton and Huang, 2015).

The RPPA assay was performed in the laboratory of Michael Davies at the MD Anderson Center RPPA Core Facility from Houston, Texas, USA, as previously described in Tibes et al.,

2006. The samples were prepared by Adina Vultur, the data processing was completed by Patricia Brafford and the biostatistical analyses were performed by Phyllis Gimotty.

Serial-diluted lysates from three MBM (M230, M331, M450) and three non-MBM (1205Lu, WM983B, WM3918) cell lines, as well as positive and negative controls, were printed on nitrocellulose-coated glass slides using a 2470 Microarray printer from Aushon Biosystems (Billerica, Massachusetts, USA). Each slide was probed with a validated primary antibody and a biotin-conjugated secondary antibody. Additionally, a Dako signal amplification system (Copenhagen, Denmark) was used to amplify the signal detected by the primary antibodies. The intensity of each spot was calculated using the MicroVigene^{TM} (VigeneTech, Billerica, Massachusetts, USA) software and compared with the intensity generated by the control lysates. A visual representation of the RPPA assay is shown in **Figure 15**.

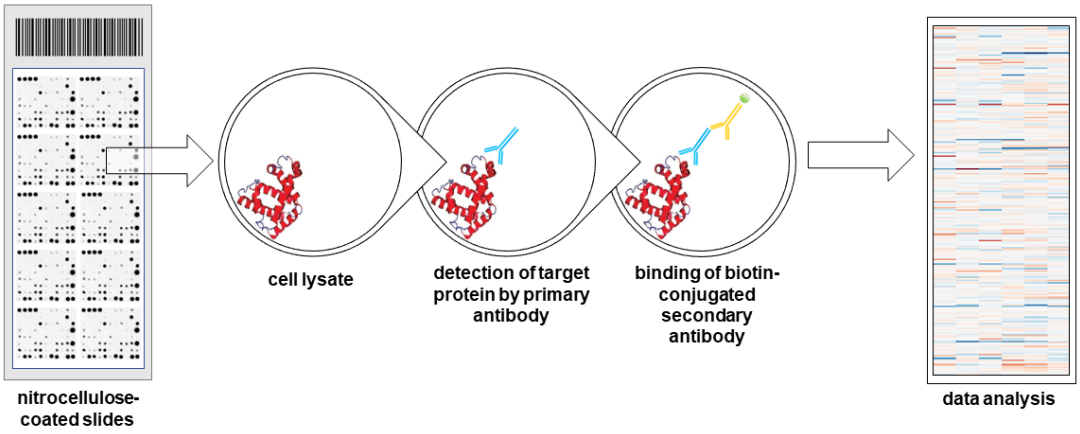

Figure 15. *An overview of the RPPA assay.* Cell lysates were printed on nitrocellulose-coated slides. Target proteins were detected by specific primary antibodies. Secondary biotinylated antibodies bound to primary antibodies, which allowed the detection of target proteins. The proteins were later visualized and data were analyzed.

All antibodies used to conduct the RPPA assay are publicly available on the webpage of the MD Anderson Center RPPA Core Facility.

To validate the findings of the RPPA assay, additional WBs were performed using fresh sets of lysates isolated from different cell cultures.

2.2.6.2. Western blot

Western blot (WB) is a molecular biology technique used to identify specific proteins from a mixture of proteins extracted from cells. This method involves four major steps: sample preparation (**2.2.6.2.1**, **2.2.6.2.2** and **2.2.6.2.3**), protein separation by size (**2.2.6.2.3**), transfer to a nitrocellulose membrane (**2.2.6.2.4**) and marking target proteins with the appropriate primary and secondary antibodies (**2.2.6.2.5**) (Mahmood and Yang, 2012).

The technique was performed as described in Vultur et al., 2008, with minor modifications. WBs were occasionally conducted by Adina Vultur (or under her supervision) at the Wistar Institute. The procedure is detailed below.

2.2.6.2.1. Protein extraction

▪ *From 2D cultures.* MBM and non-MBM cells were grown in 10 cm dishes to at least 70 % confluence. In order to remove any traces of serum and residues, cells were washed twice with ice-cold 1 X DPBS and then lysed directly on the plate with the appropriate – directly proportional to the cell confluence – lysis buffer volume. The TGH lysis buffer was freshly prepared on ice (recipe provided in **Table 3**). With the help of a cell scraper, lysates were collected from the dish surface and transferred to Eppendorf tubes. The tubes were incubated on ice for 20 min with a periodic resuspension prior to centrifugation.

▪ *From 3D cultures.* Melanoma spheroids were generated as described in section **2.2.5.2**. After 72 h of invasion in collagen, the spheroid-containing wells were washed twice with 1 X DPBS supplemented with PI. The acellular bottom layer of collagen I was removed and the top layer containing the spheroids was transferred to an Eppendorf tube. Up to 50 µl of TGH lysis buffer (same recipe as for 2D cultures) were added in each tube and were placed on ice for 40-50 min before centrifugation, with occasional mixing with a pipette.

Following isolation, both 2D and 3D lysates were centrifuged at 13,000 rpm for 10 min at 4 °C and the supernatants were collected and transferred to new tubes and kept at -80 °C until further use.

2.2.6.2.2. Determination of protein concentration

The protein concentration of MBM and non-MBM cell lysates was determined using a colorimetric protein assay. For this purpose, the Bradford reagent (see recipe in **Table 4**) was used. The reagent is based on COOMASSIE® Brilliant Blue G 250, which displays a shift in absorbance from 470 nm (red) to 595 nm (blue) upon protein binding. For each experimental sample, 1 µl of protein lysate was mixed with 799 µl of ddH_20 and 200 µl of Bradford reagent in an Eppendorf tube. A volume of 200 µl of each sample was loaded in triplicate into 96-well plates. The absorbance at 595 nm was read using the Berthold Mithras LB 940 device and the total protein concentration calculation was based on a BSA standard curve ranging from 0.5 to 20 µg/ml. The amount of absorption was directly proportional to the protein present in the sample.

2.2.6.2.3. Protein separation by size

The acrylamide gel recipes used for sodium dodecyl sulfate polyacrylamide gel electrophoresis (SDS-PAGE) can be found in **Tables 11** and **12 A-C**. SDS-PAGE allows the separation of proteins by their molecular weight, i.e. small molecular weight proteins migrate faster, while high molecular weight proteins migrate slower through the gel. The gel acts as a sieve through which the negatively charged molecules migrate towards the anode (positively charged).
All samples were adjusted to reach the same concentration (25-100 µg), they were mixed with 4 X Lämmli buffer (containing β-mercaptoethanol) and denatured at 95 °C before being resolved on the polyacrylamide gel. At first, a voltage of 60 V was applied; once the samples reached the separation gel, the voltage was increased to 110 V. A protein ladder (Precision Plus Protein™ Dual Color Standard) was used to determine the protein size.

2.2.6.2.4. Protein transfer

Following gel electrophoresis, the proteins were transferred onto 0.2 µm nitrocellulose membranes with the Trans-Blot® Turbo™ Transfer System. As recommended by the manufacturer, before starting the transfer, the membranes and the transfer stacks were equilibrated in transfer buffer for 3 min (the recipe is shown in **Table 6**). The "transfer sandwich" was assembled in the order shown in **Figure 16**.

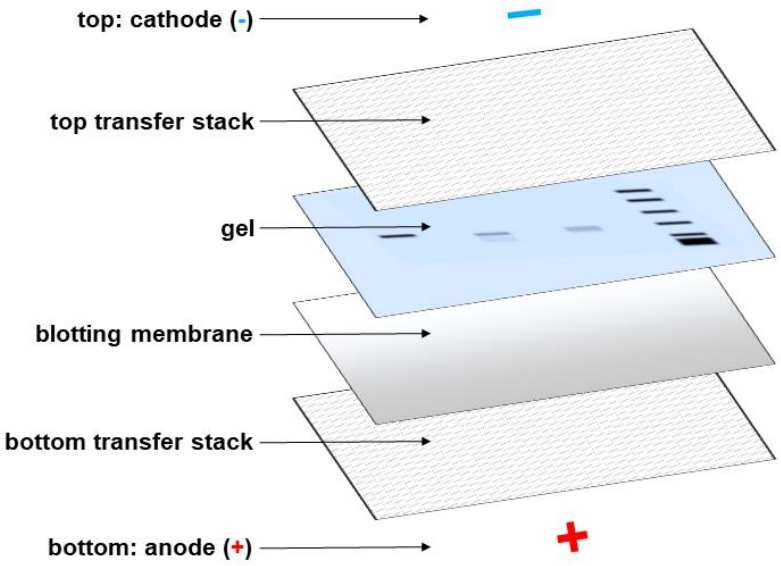

Figure 16. *Assembly of the "transfer sandwich".* The "transfer sandwich" was assembled in the following order (from the anode to the cathode): bottom transfer stack, nitrocellulose membrane, gel, top transfer stack.

The transfer was performed at 1.3 A, 25 V, for 10 min with high molecular weight proteins, for 7 min with mixed molecular weight proteins or for 5 min with low molecular weight proteins.

2.2.6.2.5. Blocking and antibody incubation

After the transfer was completed, the membranes were blocked for at least 1 h with a 5 % BSA solution, followed by an overnight incubation at 4 °C with primary antibodies. The primary antibodies used for WB and the respective dilutions are listed in **Table 17**. Next, the membranes were washed thrice with 1 X TBS-T for 5 min each time and incubated with secondary antibodies (listed in **Table 18**) for 1 h in the dark, at room temperature. Thereafter the membranes were washed thrice with 1 X TBS-T for 10 min each time. Membranes were imaged using the Odyssey® CLx system. The bands were quantified with the Image Studio™ Lite program.

2.2.6.3. GTPase activity assays

GTPases are a family of hydrolase enzymes that are inactive when bound to GDP but active when bound to GTP. RAC1 and RhoA are both small GTPases and use similar assays for detection of activity.

2.2.6.3.1. RAC1 activity assay

The RAC1 activity assay was performed using the Active RAC1 Pull-Down and Detection Kit according to the manufacturer's instructions. The kit provides a GST-fusion protein comprising the p21-binding domain (PBD) of human p21-activated protein kinase 1 (PAK1) and glutathione agarose resin to specifically pull-down the intracellular active RAC1. A volume of 500 µl RIPA-based lysis buffer freshly supplemented with 1 mM Na_3VO_4, 1 mM PMSF, 1 mM NaF and 1 X PI was used to lyse the melanoma cells grown in each 10 cm plate. Cell lysates (comprising 500 µg of protein) were incubated with gentle rocking for 1 h at 4 °C with the glutathione resin and the GST-human PAK1-PBD. For the assays in which RIPA-based lysis buffer was used, the protein concentration was determined using the Pierce™ BCA Protein Assay Kit (Thermo Fisher Scientific™, #23225), according to the manufacturer's instructions. This assay is based on the biuret reaction. The biuret reaction occurs when proteins reduce Cu^{2+} to Cu^{+} in an alkaline solution, resulting in a purple color formation by bicinchoninic acid (BCA). A volume of 25 µl of each cell lysate containing 500 µg of protein was resolved on a 12 % SDS-polyacrylamide gel. Total and active RAC1 levels were evaluated via WB as described in section **2.2.6.2**.

2.2.6.3.2. RhoA activity assay

RhoA activity was measured as described in Leinhos et al., 2019. This assay was performed by Sabine Krull and Anke Zieseniss from the scientific group of Dörthe Katschinski. In brief, the protein extraction was performed with a lysis buffer comprising 25 mM HEPES (pH = 7.5), 150 mM NaCl, 10 mM $MgCl_2$, 1 % NP-40, 1 mM EDTA, 10 % glycerol, 100 µM PMSF, 25 mM NaF, 1 mM Na_3VO_4 and 1 X PI. Cleared lysates were incubated for 1 h at 4 °C under constant rotation with 100 µl GST-Rhotekin-RBD beads. Total and active RhoA levels were assessed via WB.

2.2.7. Immunofluorescence

The immunofluorescence (IF) assay was performed as described in Roesch et al., 2010, with the assistance of Adina Vultur. Accordingly, melanoma cells were grown on glass coverslips (VWR, # 631-0172) for 72 h, washed twice with PBS^{++}, fixed for 20 min with 4 % PFA, permeabilized for 5 min in PBS^{T++} and quenched with 50 mM NH_4Cl in PBS^{T++} for 5 min at room temperature. After blocking with 1 % BSA in PBS^{T++} for 1 h, the cells were incubated for 45 min at room temperature with primary antibody solution prepared in 0.2 % BSA in PBS^{T++} (antibody dilutions are shown in **Table 17**). After one wash in 0.2 % BSA in PBS^{T++}, cells were incubated at room temperature for 45 min with the secondary antibody solution prepared in 0.2 % BSA in PBS^{T++}. Coverslips were consecutively washed in 0.2 % BSA in PBS^{T++}, PBS^{T++} and ddH_2O. VECTASHIELD® containing 1.5 µg/ml DAPI was the mounting medium used. The fluorescent signals detected from the proteins of interest were examined with a 40 X objective using a Carl Zeiss Axio Observer D1 inverted phase contrast fluorescence microscope equipped with a Colibri LED system.

2.2.8. Determination of mRNA expression levels

The determination of mRNA expression levels was occasionally performed with the help of Andrea Paluschkiwitz.

2.2.8.1. RNA isolation

The total RNA was isolated from MBM and non-MBM cells using the Nucleospin™ RNA Plus Kit. Firstly, melanoma cells were seeded in 10 cm dishes and were allowed to grow until they reached at least 70 % confluence. The cells were then pelleted, the supernatant was discarded and the pellet was resuspended and lysed in 350 µl lysis buffer (part of the kit). Each cell lysate

was then transferred to a gDNA-removal column which was discarded after a short spin-down. Next, 100 µl of binding solution were added to the flow-through. The mix was then transferred to a RNA binding column and was spun-down. The flow-through was discarded and the column was washed once with washing buffer 1 and twice with washing buffer 2 (part of the kit). Lastly, the RNA was eluted via the addition of RNase-free H_2O, the column was spun-down and the flow-through containing the total RNA was saved.
The RNA concentration was measured with the Thermo Fisher Scientific™ NanoDrop 2000c.

2.2.8.2. cDNA synthesis

The complementary DNA (cDNA) was synthesized through reverse transcription from the isolated RNA using the Superscript™ IV Reverse Transcriptase Kit, according to the manufacturer's instructions. Briefly, 800 ng of template RNA were mixed with 50 µM Oligo-$d(T)_{20}$ primers and 10 mM dNTP mix to a final volume of 13 µl. This mix was heated at 65 °C for 5 min, allowing the primer annealing. The annealed RNA was then incubated on ice for at least 1 min. To the annealed RNA, 7 µl of reaction mix were added; this consisted of 4 µl of 5 X SuperScript™ IV buffer, 1 µl of 100 mM DTT, 1 µl of ribonuclease inhibitor and 1 µl of SuperScript™ IV reverse transcriptase (200 U/µl). The mix was incubated at 50-55 °C for 10 min and lastly at 80 °C for 10 min (the incubation at 80 °C inactivated the reaction).

2.2.8.3. Quantitative real-time polymerase chain reaction (qRT-PCR)

Quantitative real-time polymerase chain reaction (qRT-PCR) monitors the amplification of a targeted DNA molecule while the polymerase chain reaction is running.
qRT-PCR was performed using the GoTaq® qPCR Master Mix, which comprises a full-length Taq DNA polymerase, dNTPs and $MgCl_2$ and a Bryt™ Green dye. The Bryt™ Green dye is a fluorescent dye ($493_{Ex}/530_{Em}$) that intercalates with the double-stranded DNA which can be monitored following each PCR cycle. The components of the reaction mix used for qRT-PCR are listed below in **Table 32**.

Table 32. qRT-PCR reaction mix

Reagent	Volume used per reaction (µl)
2 X GoTaq® qPCR Master Mix	25
10 µM forward primer	1.5
10 µM reverse primer	1.5
H_2O	12
1:10 cDNA (< 500 ng)*	10

* cDNA was pre-diluted in RNase-free H_2O (1:10).

All primers were purchased from Qiagen and are listed in **Table 19**. The qRT-PCR reaction mix including the cDNA were pipetted into each well of a 96-well PCR plate. The plate was closed with a 4titude® adhesive qPCR seal (4titude®, # 0560) in order to avoid the evaporation of the content due to high temperature cycles. The qRT-PCR was performed with the Stratagene Mx3000P qPCR System, using the following cycling program (**Table 33**):

Table 33. qPCR cycling program

Number of cycles	Temperature (°C)	Time (min:sec)	Step
1	95	15:00	polymerase activation
35-45	95	00:15	denaturation
	58 (55 for primer assays)	00:30	annealing
	72	00:30	elongation
1	95	1:00	dissociation
	58 (55 for primer assays)	00:30	
	95	00:30	

The results were analyzed with the MxPro qPCR software. TBP (TATA box binding protein) was used in all qRT-PCRs as a housekeeping gene. The CT (number of cycles required for the fluorescent signal to exceed the fluorescent threshold) values of the target mRNAs were normalized to the CT values of TBP. Data were quantitated using the $2^{-\Delta CT}$ method.

2.2.9. Human astrocyte conditioned medium preparation

In the present study, human astrocyte conditioned medium (HACM) was used to mimic elements of the brain microenvironment. For this purpose, human astrocytes were grown in specially formulated medium (human astrocyte medium) to at least 90 % confluence for 72 h. This medium containing brain soluble factors was harvested, filtered and further used for functional assays (proliferation, adhesion, migration), as shown in **Figure 17**.

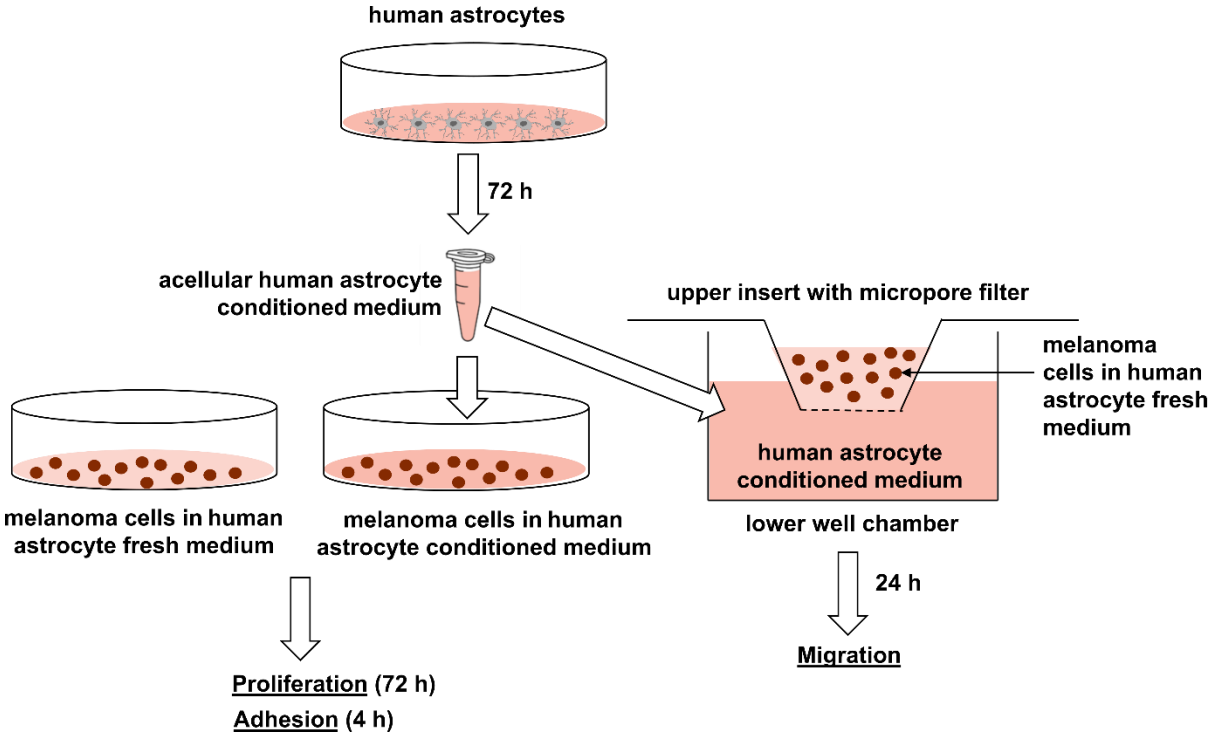

Figure 17. *HACM preparation.* Human astrocytes were grown in astrocyte medium for 72 h prior to medium harvesting. The HACM obtained was further used for proliferation assays (incubation time: 72 h), adhesion assays (incubation time: 4 h) and transwell migration assays (incubation time: 24 h). Fresh astrocyte medium was used as control for the proliferation and adhesion assays. For the migration assays, melanoma cells were seeded in inserts in fresh astrocyte medium; of note, no additional FCS was added in the bottom well of the transwell inserts to ensure that only the cells attracted to the brain soluble factors cross the membrane pores.

2.2.10. Co-culturing melanoma cells with neurons and glial cells

Co-culturing melanoma cells with primary hippocampal neurons was performed with the help of Sinem Sertel from the scientific group of Silvio Rizzoli.

Primary hippocampal cultures were prepared from P0 Wistar newborn rats as previously described (Banker and Cowan, 1977; Beaudoin 3rd et al., 2012). Briefly, newborn rat brains were collected and the hippocampi were dissected, placed in cold HBSS (Gibco, # 14025092) and incubated at 37 °C in an enzyme solution (in DMEM, 2 mg cysteine, 100 mM $CaCl_2$, 50 mM EDTA and 25 U/ml papain). After 1 h, the hippocampi were incubated in an inactivating solution (in DMEM 5 % FCS, 25 mg albumin and 25 mg trypsin inhibitor). After 15 min, 40,000 cells were cultured in MEM supplemented with 10 % horse serum, 3.3 mM glucose and 2 mM glutamine, on 24-well glass plates (Cellvis, # P24-1.5P) previously coated with 1 mg/ml poly-L-lysine hydrochloride (Sigma-Aldrich, # P2658). After 4 h the medium was replaced with Neurobasal-A medium (Gibco, # 10888022) with B27 supplement (Gibco, # 17504044), GlutaMAX™ (Gibco, # 35050061), 20 U/ml penicillin and 20 µg/ml streptomycin and the cells were incubated for 21 days at 37 °C (Opazo et al., 2010). At DIV21, 2,000 melanoma cells pre-

stained with CellTracker™ Green CMFDA were added in each well. After 24 h, each well was imaged (Cytation™ 5, BioTek) and analyzed by Sinem Sertel using MATLAB. The circularity score (i.e. how similar a cell's morphology is to a circle) of each green positive melanoma cell was determined.

2.2.11. Protein knockdown studies

Stable downregulation of RAC1 was performed as described in Noguchi et al., 2018 via small hairpin RNA (shRNA) and lentiviral infection of the non-MBM lines WM983B, WM3918 and the MBM lines M331 and WM4237.

Vectors and shRNAs used in this study were purchased from Addgene or Sigma-Aldrich MISSION® (**Tables 21** and **22**). Glycerol stocks of shRNA were grown in LB medium with ampicillin. Plasmid preparation was performed using the HiSpeed® Plasmid Maxi Kit. The plasmid concentration was assessed using Thermo Fisher Scientific™ NanoDrop 2000c.

The lentiviral production of shRNA particles was performed by seeding HEK293TN cells at 60 % confluence in 10 cm dishes and transfecting with 1 ml Lipofectamine® 2000/Opti-MEM mix (1:50 ratio), 1 µg pMD2.6, 3 µg psPAX2 and 4 µg pLKO.1 (empty vector, shRAC1_1 or shRAC1_2). Following a period of 24, 48 and 72 h post-transfection, the media (containing the virus with control or knockdown plasmids) were harvested and filtered through a 0.45 µ pore filter. The viral supernatants were then used to infect melanoma cells (48 h samples), while the rest were frozen at -80 °C as backups (24 h and 72 h supernatants).

WM983B, WM3918, M331 and WM4237 melanoma cells were seeded separately at 60 % confluence in 6-well plates. To increase the infection efficiency, 8 µg/ml polybrene were added to the 48 h virus/medium mix (before its addition to the melanoma cells). After 24 h of infection, the virus-containing medium was removed and fresh medium enriched with 1-2 µg/ml puromycin in order to select for the transfected cells was added. Selection occurred over 48 h; thereafter the medium containing puromycin and non-transfected cell debris was replaced with fresh medium without antibiotics and the surviving cells were allowed to recover. Puromycin (4 µg/ml) was added every 2 weeks over 24 h to the culture media in order to select for the knockdown (KD) cells. All further experiments were performed in the absence of antibiotics.

2.2.12. *In vivo* studies

Animal experiments were performed in NSG (NOD scid gamma) mice by Adina Vultur, Tetiana Godok and Haiyin Li at the Wistar Institute (scientific group of Meenhard Herlyn), as previously described (Krepler et al., 2017). Mice were divided into three groups: sh control (5

female and 4 male mice), shRAC1_1 (5 female and 4 male mice) and shRAC1_2 (4 female mice). Prior to injection, WM4237 MBM cells (sh control, shRAC1_1 and shRAC1_2) were infected with the pCDH-EF1a-eFFly-mCherry plasmid (Addgene #104833) by lentiviral transduction and only the positive mCherry cells were further used. Positive mCherry cells were sorted using a MoFlo Astrios EQ cell sorter with Summit Software (Beckman Coulter, Brea, CA). Mice were each subcutaneously (s.c.) injected with 80,000 stable WM4237 sh control, shRAC1_1 and shRAC1_2 cells embedded in reduced growth factor Matrigel^{TM}. Tumor size was measured every 3-5 days using a caliper (Width x Depth x Height)/2 [mm³]. Primary tumors were removed if they reached 1,000 mm³ in size and mice were allowed to recover. If necessary for animal welfare, mice were prematurely sacrificed. After 58 days of tumor growth, mice were euthanized. Tumors were imaged using an IVIS 200 whole body system (Xenogen, Alameda, California, USA).

2.2.13. Statistical analyses

Data were analyzed using Microsoft Excel 2016 or GraphPad Prism 9 and presented as mean ± SEM (standard error of the mean), unless otherwise specified. Statistical significance was typically tested with unpaired, two-tailed Student's t-test. The False Discovery Rate (FDR) procedure was used to evaluate multiple comparisons in the RPPA dataset. The significant differences are marked with * for $p < 0.05$, ** for $p < 0.01$ and *** for $p < 0.001$.

3. RESULTS

3.1. Melanoma brain metastasis cells are Melan-A positive

Prior to experimentation, the melanoma status of all MBM lines used for this project was validated by Melan-A staining using IF (**Figure 18**). Melan-A (shown below as a green signal) is a melanoma-specific antigen. A no primary antibody solution was used to verify that the green signal was specific to Melan-A and not to the secondary antibody. HEK293 cells (human embryonic kidney cell line) were used as a negative control.

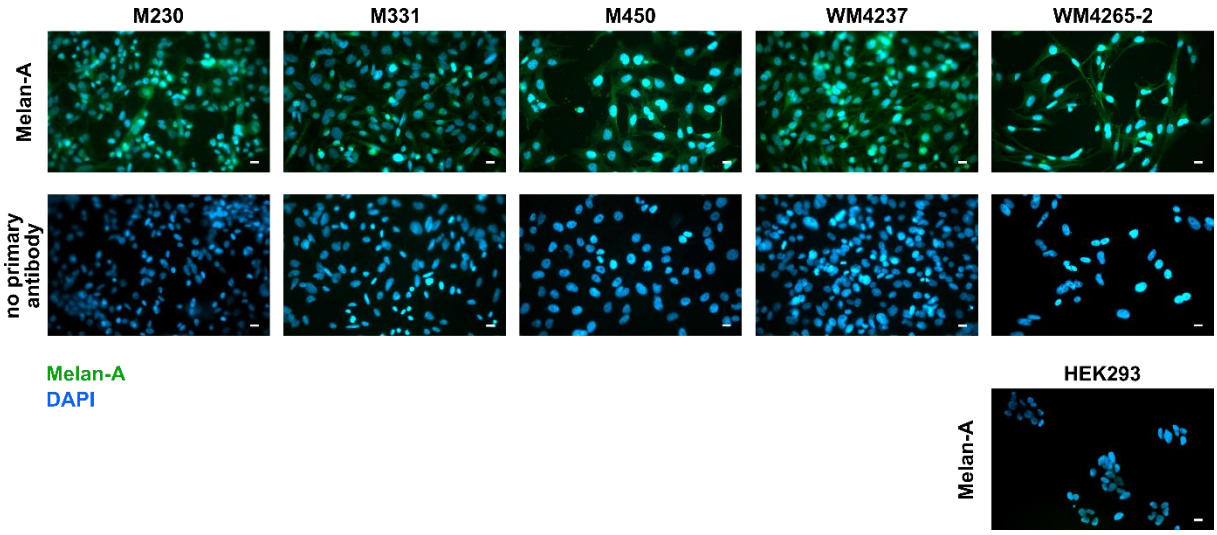

Figure 18. *Melanoma cell identity of MBM cells.* The melanoma status of all MBM lines (M230, M331, M450, WM4237, WM4265-2) was validated by positive Melan-A staining (green signal) using IF. Nuclear staining using DAPI is shown in blue. HEK293 cells were used as a negative control. Magnification: 40 X. Scale bar: 50 µm.

The MBM cell lines used for this study were established from different patients and independently in two different laboratories, the Wistar Institute ("WM" lines) and Hadassah Medical Center ("M" lines). Targeted RNA sequencing studies of these five MBM cell lines, focused on 108 common melanoma altered genes (see **Table 24**), were performed for this project and are now published (Krepler et al, 2017; Garman et al, 2017). Targeted sequencing was also conducted on the non-MBM cell lines used for this study (WM793, 1205Lu, WM983B, WM3918). Three out of a total of nine investigated cell lines featured wild-type (WT) BRAF (WM3918, M450, WM4265-2); of these, only one was also NRAS-mutant (WM4265-2). All the other examined cell lines were BRAF-mutant (WM793, 1205Lu, WM983B, M230, M331, WM4237) and one MBM line was both BRAF- and NRAS-mutant

(M230). All nine cell lines presented additional gene mutations, but no specific alteration appeared more frequently in the MBM cell lines, compared to the extracranial lines (**Table 24**).

3.2. Melanoma brain metastasis cells display distinct signaling profiles

To identify molecular signals and pathways specific to the MBM cells, RPPA analyses comparing three non-MBM (1205Lu, WM983B, WM3918) and three MBM cell lines (M230, M331, M450) were performed. With this method, 297 total and phosphorylated proteins were examined (**Suppl. Table 1**). Our analyses revealed 10 hits (FDR ≤ 10 %) as distinctly expressed between non-MBM and MBM cell lines, which were grouped into proliferation/survival-related hits (**Figure 19 A**) and adhesion/migration-related hits (**Figure 19 B**); although not categorized as hits, additional signaling effectors are also shown in their corresponding groups, as they are important for melanoma biology or are related to the proteins defined as hits.

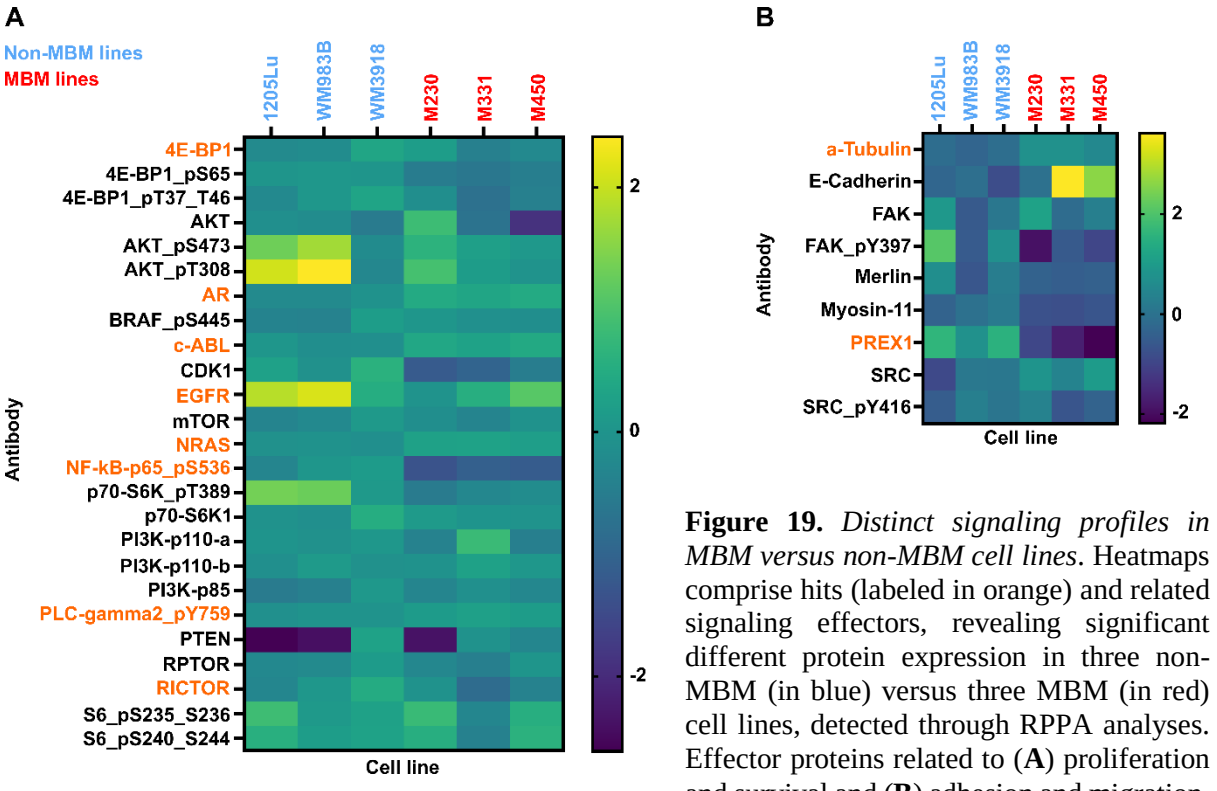

Figure 19. *Distinct signaling profiles in MBM versus non-MBM cell lines*. Heatmaps comprise hits (labeled in orange) and related signaling effectors, revealing significant different protein expression in three non-MBM (in blue) versus three MBM (in red) cell lines, detected through RPPA analyses. Effector proteins related to (**A**) proliferation and survival and (**B**) adhesion and migration. Each heatmap box reveals the mean value from three samples per cell line and is shown as yellow in case of high protein abundance and as indigo in case of low protein abundance. "p" stands for phosphorylated protein.

While high levels of phosphorylated AKT were previously observed by others in MBM cells (Chen et al., 2014; Davies et al., 2009; Niessner et al., 2013), we could not confirm this in our panel of MBM lines. Distinct 4E-BP1, NRAS, NF-κB or RICTOR expression patterns were instead detected and were highlighted for validation by WB. Interestingly, PREX1, a GEF for

RAC1, was significantly downregulated in the MBM lines, compared to the non-MBM lines. Merlin, a tumor suppressor involved in the regulation of RAC1/PAK1 signaling (Shi et al., 2016), was also decreased in the MBM lines (albeit not significantly between the two groups). Given that some of these proteins and the signaling pathways in which they are involved are interconnected, it is plausible to presume that MBM cells can use these networks distinctly and to their advantage.

In an expanded panel of MBM lines, the validation of a number of proteins detected by the RPPA assay was undertaken. Namely, RAS and NF-κB levels, mTOR-related signals (RPTOR of mTORC1, RICTOR of mTORC2, total mTOR, p70S6K, 4E-BP1) were examined, but no consistent distinct activity or expression pattern was validated in the MBM lines (**Figure 20 A**). Next, the expression of proteins involved in adhesion and migration was examined in two non-MBM and two MBM lines. Total and phosphorylated levels of FAK and SRC were higher in the non-MBM lines, compared to the MBM lines. While our RPPA did not include the direct investigation of RAC1, many proteins identified as hits are related to this protein (NF-κB, EGFR, PREX1, mTOR-related signals) (Liang et al., 2021); hence, we investigated RAC1 levels in the same panel of cell lines and we detected RAC1/CDC42 upregulation in the MBM lines (**Figure 20 B**).

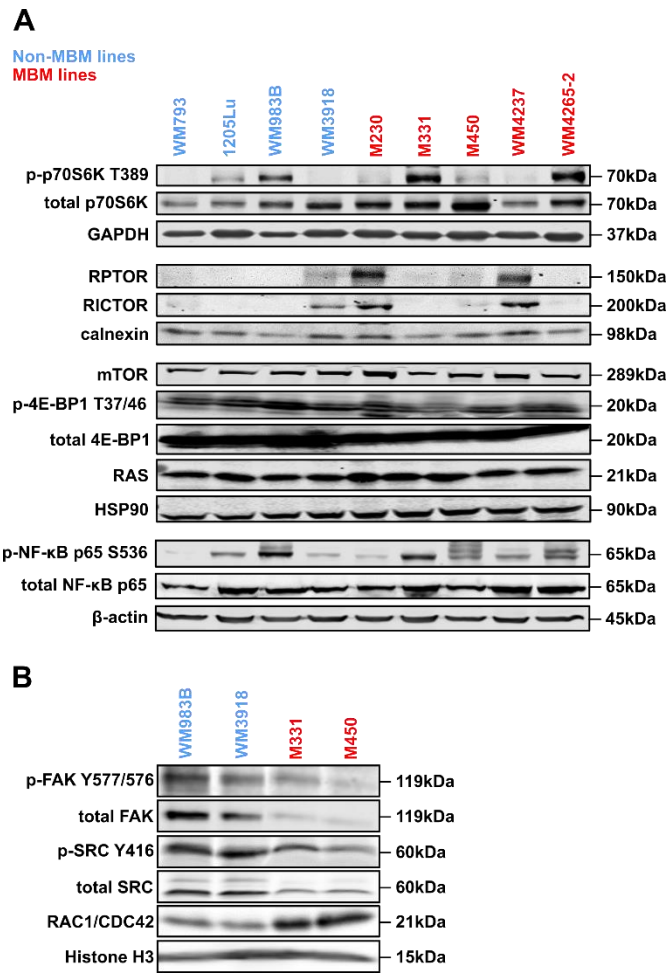

Figure 20. *Validation of RPPA results by western blot.* (**A**) WB analyses of proliferation/survival-related proteins: phosphorylated and total p70S6K, RPTOR, RICTOR, mTOR, phosphorylated and total 4E-BP1, RAS, phosphorylated and total NF-κB. GAPDH, calnexin, HSP90 and β-actin were used as loading controls. (**B**) WB analyses of phosphorylated and total FAK, phosphorylated and total SRC and RAC1/CDC42. Histone H3 was used as a loading control. Non-MBM cell lines are labeled in blue, while the MBM lines are written in red. "p" stands for phosphorylated protein.

3.3. Melanoma brain metastasis cells display distinct growth properties

Given the distinct expression of molecular signals associated with proliferation and adhesion/migration in MBM versus non-MBM cells, we next performed a series of functional assays in our panel of cell lines, including proliferation, adhesion, migration and invasion assays. Despite the genetic heterogeneity of the investigated melanoma cell lines, MBM lines displayed significantly lower proliferation rates over 96 h than non-MBM lines in standard *in vitro* culture (**Figure 21 A**). Moreover, high cell density at 72 h did not enhance MBM growth (**Figure 21 B**).

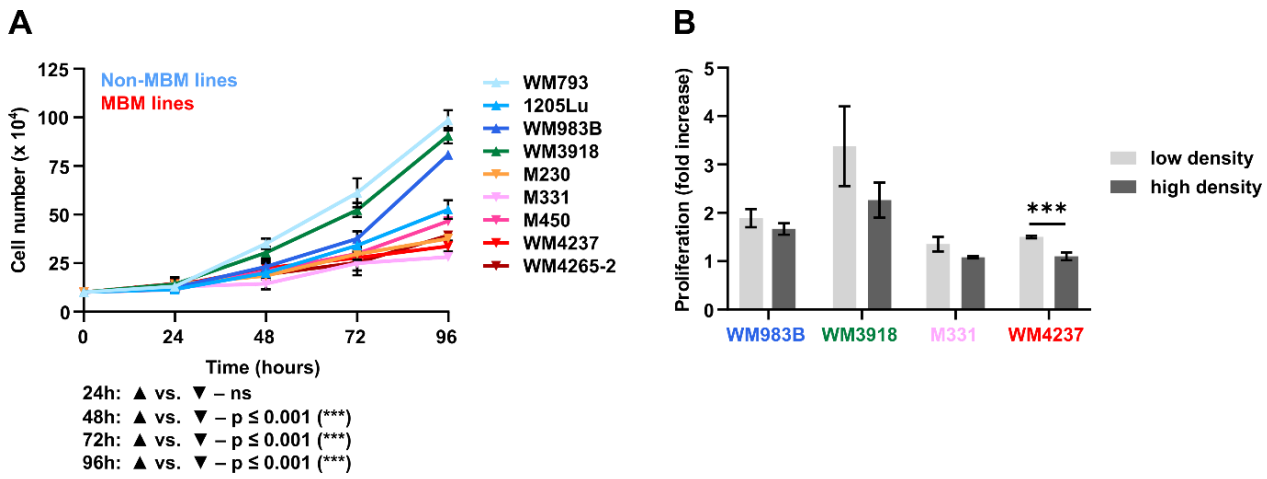

Figure 21. *Growth profile of MBM versus non-MBM cell lines*. (**A**) Non-MBM cells (in cool colors) and MBM cells (in warm colors) proliferation over 96 h. 10,000 cells/well were seeded in 24-well plates and counted every 24 h for four days. Each triangle represents n=4 wells ± SEM from three independent experiments. The Mann-Whitney test was used to compare proliferation in MBM versus non-MBM lines with significance at 48 h, 72 h and 96 h. (**B**) Cell density does not enhance MBM proliferation. Non-MBM cells (WM983B and WM3918) and MBM cells (M331, WM4237) were seeded at 5,000 cells/well (low density) or 30,000 cells/well (high density) and were allowed to proliferate for 72 h prior to counting. The fold increase in counted cell number over seeded number is shown. Data are presented as mean of n=4 wells/condition ± SEM from two separate experiments. Unpaired, two-tailed Student's t-tests were used to compare low- and high- density cells, (*) $p < 0.05$; (**) $p < 0.01$; (***) $p < 0.001$.

Because MBM cells grow slowly under standard culture conditions, growth factors and nutrients were added to the culture medium in order to stimulate cell proliferation. Upon incubation with insulin (100 µg/ml) for 72 h, a significant increase in proliferation was noticed in all the investigated MBM cell lines compared to the non-MBM lines (**Figure 22 A**). However, the addition of insulin-like growth factor 1 (IGF-1, 50 ng/ml) only significantly enhanced the proliferation in one MBM line (**Figure 22 B**). Since glucose is the main source of energy for the human brain (Mergenthaler et al., 2013), the effects of increased glucose concentrations in the culture medium (from 25 mM to 50 mM) were also investigated. Interestingly, MBM cells were unaffected by the glucose changes (**Figure 22 C**). The addition of different concentrations of glutamine, a nonessential amino acid, also did not enhance MBM

proliferation. Notably, only non-MBM growth was significantly enhanced in the presence of glutamine, compared to MBM growth (**Figure 22 D**).

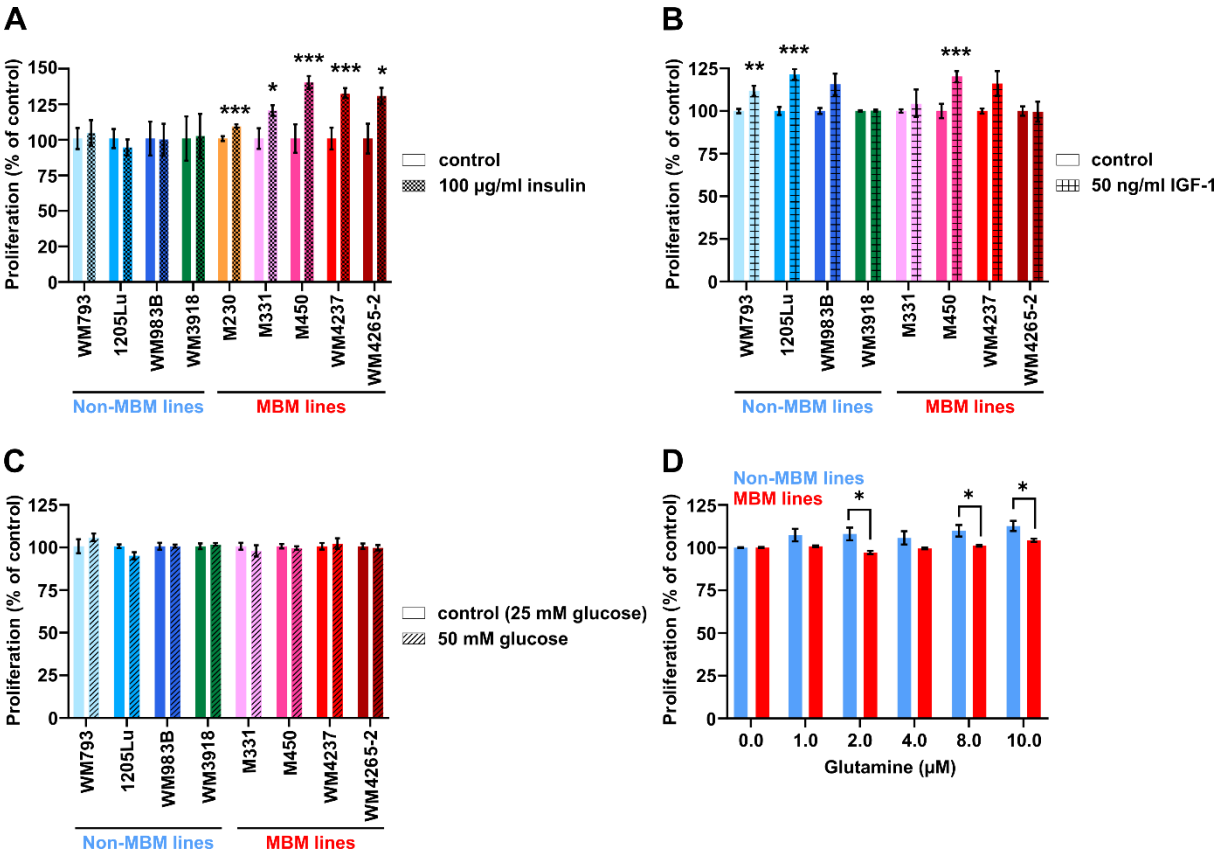

Figure 22. *MBM cell proliferation is enhanced in the presence of insulin.* (**A-C**) Proliferation of MBM versus non-MBM cells in the presence of 100 µg/ml of (**A**) insulin, (**B**) 50 ng/ml of IGF-1 and (**C**) 50 mM of glucose. 5,000 cells/well were seeded in 96-well plates and were allowed to adhere for 24 h before treatment. Cells were incubated with growth factors or nutrients for 72 h prior to fluorescence measurement. (**D**) Proliferation of MBM versus non-MBM cells, in the presence of glutamine. 5,000 cells/well were seeded in 96-well plates and were allowed to adhere for 24 h before treatment. Cells were incubated with different concentrations of glutamine (0-10 µM) for 72 h prior to fluorescence measurement.
Data are presented as mean of three independent experiments ± SEM (n=4 wells/each experiment). In (A-C), non-MBM cells are displayed in cool colors and MBM cells are shown in warm colors. In (D) pooled non-MBM cells are shown in blue and pooled MBM cells in red. Statistical significance was assessed using unpaired, two-tailed Student's t-test, (*) $p < 0.05$; (**) $p < 0.01$; (***) $p < 0.001$. In (A-C), treated cells were compared to their untreated control. In (D), non-MBM cells were compared to MBM cells at different glutamine concentrations.

To assess intrinsic metastasis-associated properties in MBM cells, adhesion studies (**Figure 23 A**), transwell migration assays (**Figure 23 B**), invasion assays using both Matrigel™-coated transwell inserts (**Figure 23 C**) and 3D spheroids embedded in collagen I (**Figure 23 D**) were performed. Interestingly, MBM lines did not reveal distinct adhesion, migration or invasion properties in standard culture compared to non-MBM lines; the differences observed were instead cell line-specific.

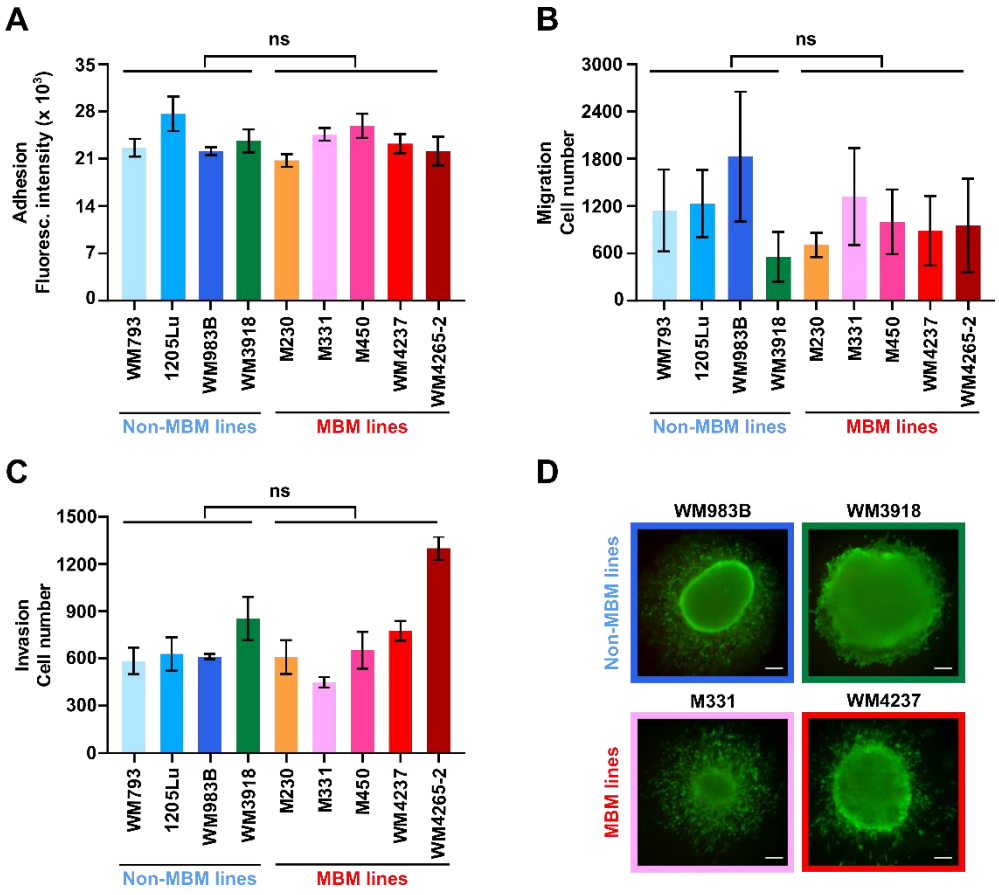

Figure 23. *MBM cells do not display a more aggressive behavior in standard in vitro functional assays compared to non-MBM cells.* (**A**) Adhesion potential of MBM versus non-MBM lines. 20,000 cells/well were seeded for 20 min prior to washing; the remaining cells were measured. Data are presented as mean of three separate experiments ± SEM (n=4 wells/each experiment; N=3). (**B**) Migration potential of MBM versus non-MBM lines. 20,000 cells were seeded in each insert and were allowed to migrate towards conditioned media (supplemented with 10 % FCS) for 24 h. Data are presented as mean ± SEM (N=3 independent experiments). (**C**) Invasion of MBM versus non-MBM lines using Matrigel™-coated inserts. 250,000 cells were seeded in each insert pre-coated with Matrigel™ (diluted 1:1 in DMEM) and were allowed to invade towards conditioned media (supplemented with 20 % FCS) for 24 h. Data are presented as mean ± SEM (N=3). (**D**) Intrinsic invasion of MBM versus non-MBM cells in a collagen I matrix. 3D spheroids were allowed to invade for 72 h prior to image acquisition. Representative images of non-MBM (WM983B, WM3918) and MBM (M331, WM4237) spheroids are shown (n≥3 spheroids/cell line). Live cells are shown in green, dead cells in red. Magnification: 10 X. Scale bar: 100 µm.
Non-MBM cells are displayed in cool colors and MBM cells are shown in warm colors. (A-C) Statistical significance comparing non-MBM and MBM cells was assessed using unpaired, two-tailed Student's t-test, (*) $p < 0.05$; (**) $p < 0.01$; (***) $p < 0.001$; (ns) not significant.

Altogether, our observations thus far indicate that melanoma cell lines of brain metastasis origin can display reduced growth *in vitro* and this can be enhanced by the addition of insulin. However, adhesion, migration or invasion properties in MBM lines are not overall different when compared to extracranial cell lines.

3.4. Melanoma brain metastasis cells express high levels of RAC1

In order to confirm the distinct expression of RAC1 in MBM cells, RAC1 and CDC42 levels were evaluated separately in an expanded panel of cell lines. High levels of total RAC1 were consistently detected in all the MBM cell lines tested, compared to non-MBM lines. However, CDC42 upregulation was not observed (**Figure 24 A**). Moreover, lysates of two non-MBM and two MBM cell lines grown as 3D invading spheroids also confirmed RAC1 upregulation in the MBM lines, regardless of cell density, culture conditions or presence of a collagen I matrix (**Figure 24 B**).

As RAC1 is a GTPase, its activity was next assessed by a pulldown assay; this activity assay is based on the GTP-bound RAC1 interaction with the p21-binding domain (PBD) of PAK1. As shown in **Figure 24 C**, RAC1 activity was not enhanced in the MBM cell lines, despite high total protein expression. Interestingly, the non-MBM line WM3918 consistently showed high RAC1 activity, in spite of being the cell line with the lowest total RAC1 levels from all the investigated cell lines (**Figure 24 A**), indicating that the assay can detect high RAC1 activity but this is not clearly seen in MBM cells.

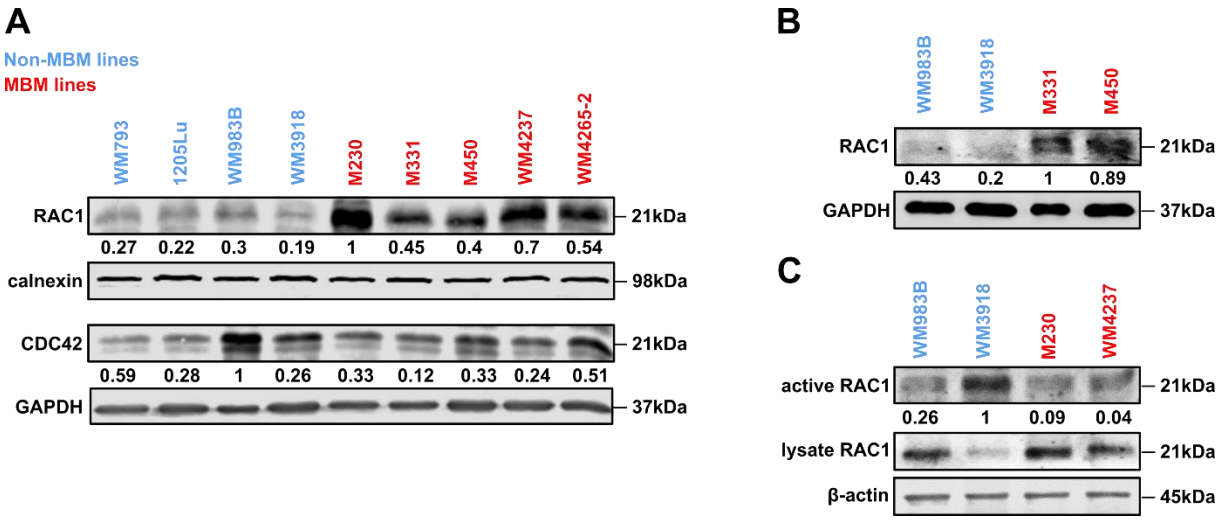

Figure 24. *RAC1 protein is upregulated in the MBM lines compared to non-MBM lines*. (**A**) WB analyses in non-MBM and MBM lines revealed high RAC1 expression in the brain; CDC42 expression was cell line-dependent. RAC1 and CDC42 band quantitation is shown as the ratio between the total protein and the loading control (calnexin and GAPDH, respectively), 1 being the highest value. (**B**) RAC1 expression is elevated in lysates prepared from 3D spheroids embedded in collagen I. RAC1 band quantitation is shown as the ratio between RAC1 and the loading control GAPDH. (**C**) RAC1 pull-down assay showing active RAC1 in non-MBM and MBM lines. A representative blot of two separate experiments is shown, as well as the band quantitation of active RAC1 relative to total (lysate) protein levels. β-actin was used as the loading control. Non-MBM cell lines are labeled in blue and the MBM lines in red.

The environment in which proteins work is determined by their subcellular localization. Subcellular localization thus modulates the access of proteins to various molecular interaction

partners and is important for understanding the protein functions as well as the overall organization of the cell (Scott et al., 2005). RAC1 has been demonstrated to localize to various subcellular compartments, including endosomes and the nucleus, in addition to the cytosol and cell membrane, and to shift between these cellular compartments in response to stimuli (Abdrabou and Wang, 2018). In order to investigate RAC1 subcellular localization, IF staining of MBM and non-MBM cells in 2D and 3D was performed; DAPI was used for nuclear staining. A diffuse RAC1 expression was noted under both 2D (**Figure 25 A**) and 3D (**Figure 25 B**) conditions.

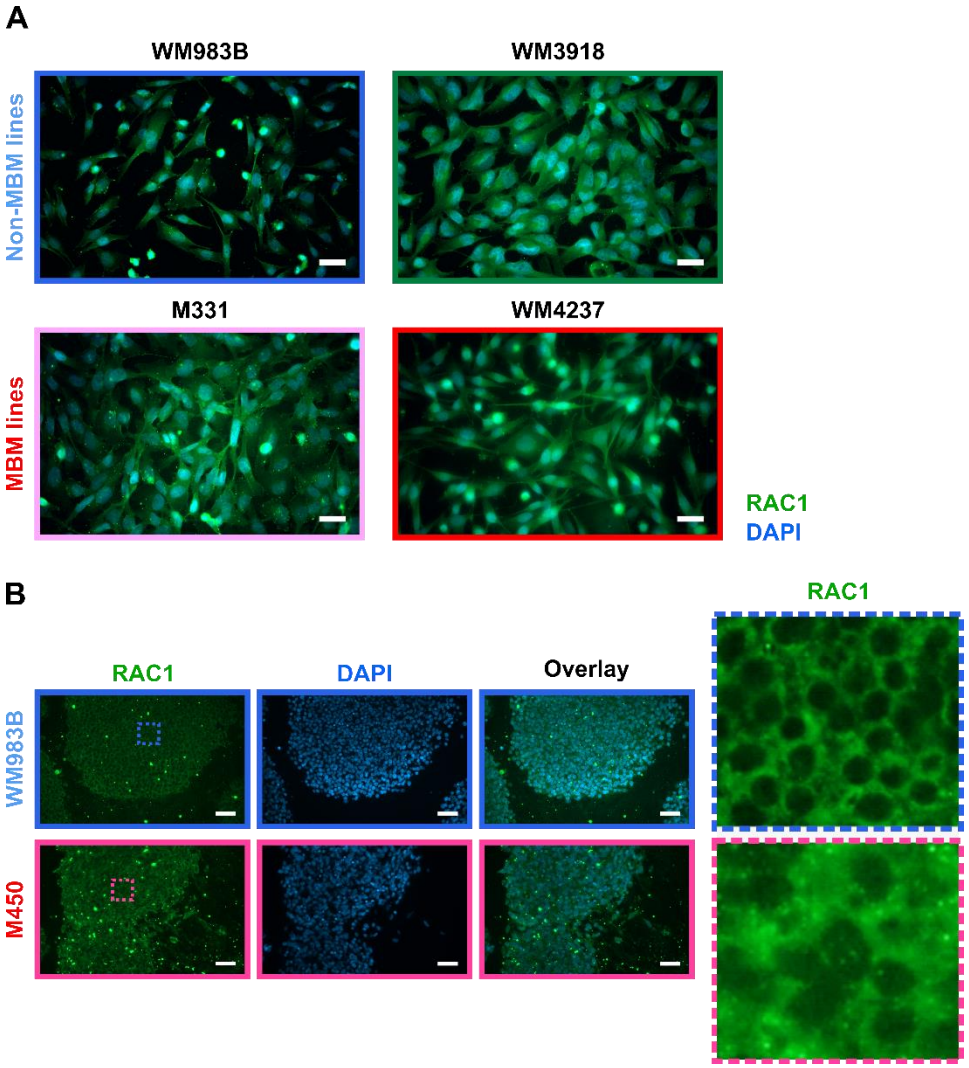

Figure 25. *RAC1 cellular localization is diffuse in both MBM and non-MBM cells.* (**A**) IF staining of RAC1 protein (green signal) in non-MBM (WM983B, WM3918) and MBM cells (M331, WM4237). Nuclei are stained with DAPI (blue signal). Scale bar: 50 µm. (**B**) IF staining of RAC1 protein (green signal) across 3D melanoma non-MBM (WM983B) and MBM spheroids (M450). Nuclei are stained with DAPI (blue signal). Scale bar: 100 µm. Magnification: 40 X. Right hand insets correspond to the dotted blue and red boxes shown on the left. Non-MBM cell lines are labeled in blue and the MBM lines in red.

Due to the fact that RhoA is involved in a regulatory double negative feedback loop with RAC1 (Chauhan et al., 2011), its expression levels as well as its GTPase activity using a pull-down assay were also assessed (Leinhos et al., 2019). WB analyses displayed a cell line-dependent total RhoA expression in the investigated melanoma cell lines (**Figure 26 A**), suggesting that changes in RAC1 expression are independent of RhoA. Moreover, no increased RhoA activity was detected in the MBM lines (**Figure 26 B**). On the other hand, the RAC1 direct effector PAK1 and its downstream effector c-Jun N-terminal kinase 1 (JNK1) displayed higher activity in 4 out of 5 of MBM cell lines (**Figure 26 C**); the p54 isoform of JNK showed high activity in all MBM lines. This indicates a possible RAC1/PAK1/JNK1 signaling axis in the MBM cells similar to the one involved in interneuron development (de Curtis, 2014). RAC3 levels were also investigated, but no increased expression was detected in the MBM lines (**Figure 26 C**), indicating that RAC1 total protein on its own is important for MBM biology.

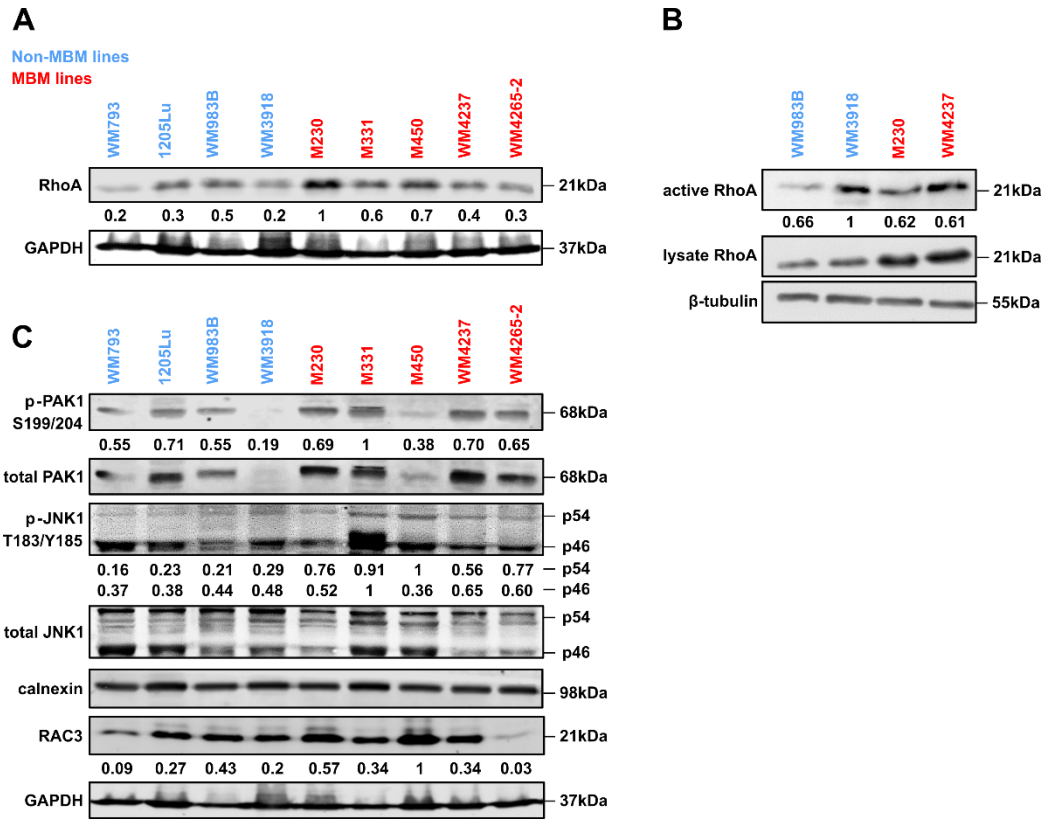

Figure 26. *Expression and activity of RAC1 effector proteins, assessed by western blot analyses.* (**A**) RhoA is not upregulated in the MBM lines compared to the non-MBM lines. Band quantitation is shown as the ratio between total RhoA and the loading control GAPDH. (**B**) Pull-down assay showing active RhoA in the non-MBM and MBM lines. A representative blot of two separate experiments is presented, as well as the band quantitation of active RhoA relative to total (lysate) protein levels. β-tubulin was used as the loading control. (**C**) PAK1 and JNK1 levels are elevated in the MBM lines; RAC3 levels are cell line-dependent. Band quantitation for PAK1 and JNK1 is shown as the ratio between phosphorylated and total protein. For PAK1 and JNK1 (total and phosphorylated) blots, calnexin was used as the loading control. For the RAC3 blot, band quantitation is normalized to the loading control GAPDH. Non-MBM cell lines are labeled in blue and the MBM lines in red. "p" stands for phosphorylated protein.

3.5. RAC1 inhibition enhances melanoma brain metastasis cell death

RAC1 and its effectors continue to emerge as key regulators of resistance to targeted therapeutics (Bid et al, 2013). Targeting RAC1 therapeutically has been challenging in the clinics; however, inhibitors are available (Liang et al., 2021). Targeted therapeutics aiming at RAC1 GEFs commonly used in drug studies are described in section **1.1.4.3**. Given the high RAC1 expression in our MBM cells, we next investigated if these cells were more responsive or resistant to RAC inhibitors and inhibitors currently used in the clinics targeting the MAPK pathway.

As shown in **Figure 27 A i**, the small molecule inhibitor EHop-016 (RAC inhibitor) reduced melanoma proliferation upon 48 h incubation in standard culture. MBM cells appeared more resistant to high doses of this compound (5-10 μM), but this could be a result of their lower proliferation rate. On the other hand, EHop-016 induced cell death only in the MBM line M331 but not in the extracranial line WM983B, as shown in the WB analysis looking at poly (ADP-ribose) polymerase (PARP) cleavage (**Figure 27 A ii**). NSC23766 (RAC1 specific inhibitor) at physiological doses did not affect melanoma cell proliferation; however, when higher drug concentrations were tested (50-100 μM), MBM cells were less sensitive to it, compared to the non-MBM cells (**Figure 27 B**), possibly due to their higher RAC1 levels. EHT 1864 (RAC inhibitor) did not decrease MBM proliferation at doses up to 10 μM; on the contrary, this small molecule inhibitor slightly stimulated the proliferation of MBM cells (**Figure 27 C**). Given the non-specific targets associated with each compound, additional signaling studies are necessary to understand these drug responses.

When the clinically-relevant BRAF*V600E* inhibitor vemurafenib (**Figure 27 D**) and MEK inhibitor trametinib (at low doses) (**Figure 27 E**) were tested in the MBM and non-MBM cell lines, limited effects on proliferation were observed; moreover, differences between the two groups were rather unnoticeable. However, because BRAF*V600E* inhibitors combined with other targeted therapies have previously shown promising clinical results (Broman et al., 2019; Wong and Ribas, 2016), the combination of BRAF*V600E* and RAC inhibitors was next investigated in the MBM cells. As shown in **Figure 28 A**, the combination treatment of vemurafenib and EHop-016 was more effective than either single agent administered alone. To mimic *in vivo* conditions, the same experiment was conducted in 3D spheroids grown in a collagen I matrix and similar effects were noticed, most notably in the MBM cell lines (**Figure 28 B**). Of note, higher drug concentrations were used in the 3D setting to allow drug penetration through the thick support matrix. The effect of RAC inhibition along with BRAF*V600E* inhibition on cell migration in the absence of a matrix was also tested (**Figure 28 C**). EHop-

016 alone altered melanoma migration, most notably in the MBM lines; however, the combination treatment of vemurafenib and EHop-016 was proven more effective against MBM migration. Of note, as this was a shorter assay (to account for the increase in cell number as a result of proliferation), lower drug concentrations were used.

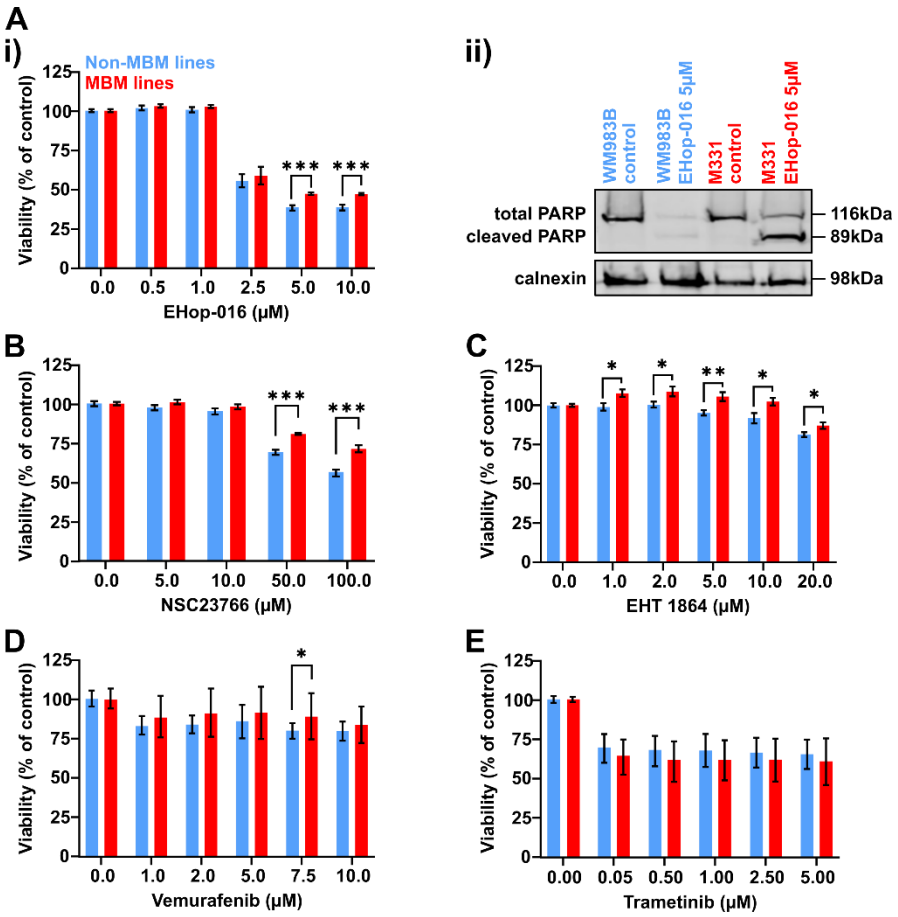

Figure 27. *Inhibition of RAC1 and MAPK by small molecule inhibitors in MBM and non-MBM cell lines.* (**A**) **i)** Cell viability upon EHop-016 treatment. 5,000 cells/well were seeded in 96-well plates and were allowed to adhere for 24 h before treatment. Cells were incubated with different concentrations of EHop-016 (0-10 μM) for 48 h prior to CellTiter-Blue® measurement. **ii)** WB analysis for PARP cleavage in WM983B (non-MBM line) and M331 (MBM line) treated with EHop-016 (and their corresponding untreated controls). Calnexin was used as loading control. (**B-C**) Cell viability upon (**B**) NSC23766 and (**C**) EHT 1864 treatment. 5,000 cells/well were seeded in 96-well plates and were allowed to adhere for 24 h before treatment. Cells were incubated with different concentrations of NSC23766 (0-100 μM) or EHT 1864 (0-20 μM) for 48 h prior to fluorescence measurement. (**D-E**) Cell viability upon (**D**) vemurafenib and (**E**) trametinib treatment. 5,000 cells/well were seeded in 96-well plates and were allowed to adhere for 24 h before treatment. Cells were incubated with different concentrations of vemurafenib (0-10 μM) or trametinib (0-5 μM) for 72 h prior to fluorescence measurement.
Data are presented as mean of three independent experiments ± SEM (n=4 wells/each experiment). Pooled non-MBM cells are shown in blue and pooled MBM cells in red. Statistical significance was assessed using unpaired, two-tailed Student's t-test, (*) $p < 0.05$; (**) $p < 0.01$; (***) $p < 0.001$ (drug effects on MBM cells were compared to the effects on non-MBM cells).

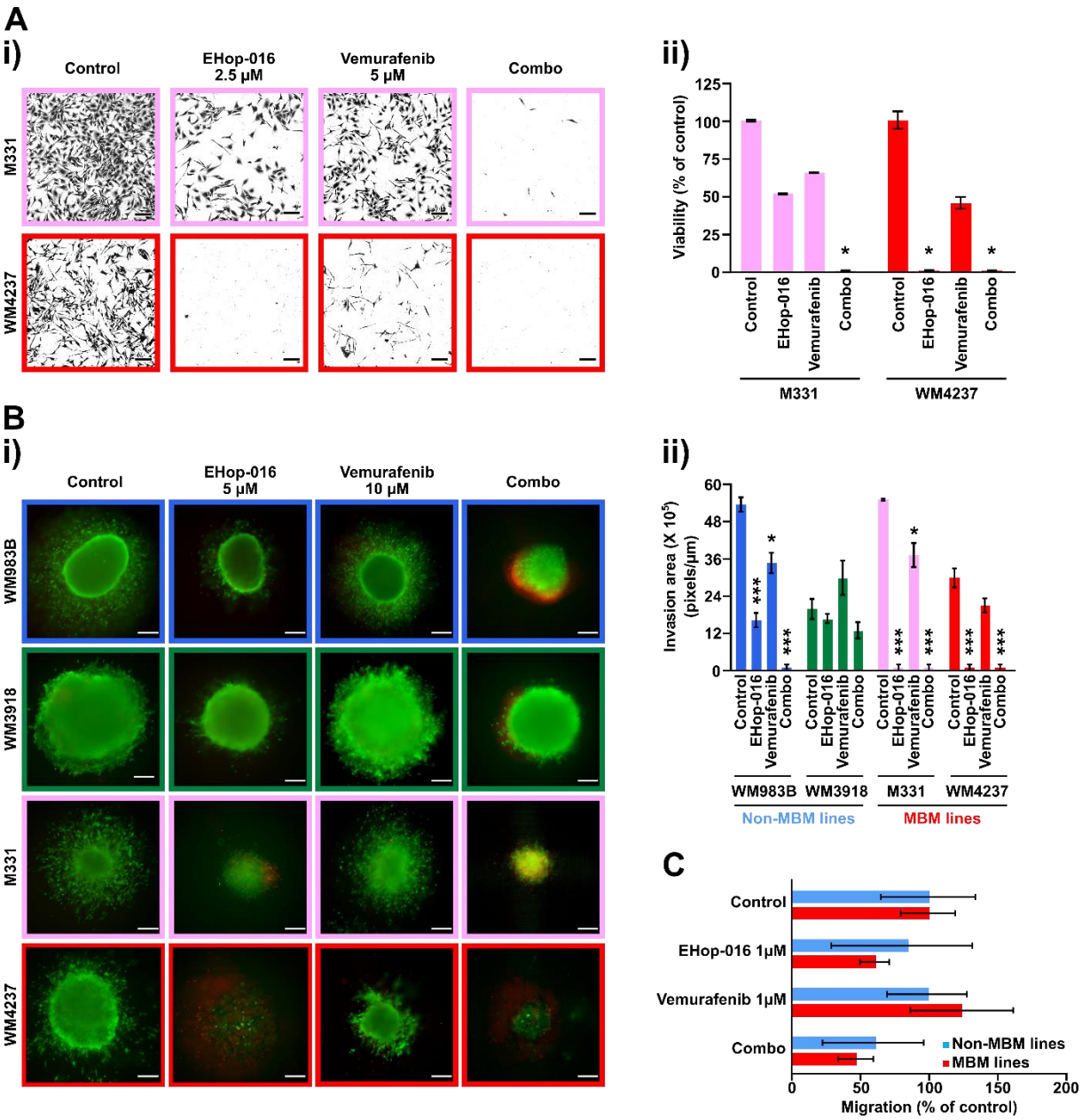

Figure 28. *Combined RAC and BRAFV600E inhibitor treatment reduces MBM proliferation, invasion and migration.* (**A**) **i)** Representative images of viable MBM cells following 72 h treatment with the indicated inhibitors. Cells were stained with 0.05 % crystal violet and imaged using brightfield microscopy. Scale bar: 50 µm. Magnification: 10 X. **ii)** Quantification of the crystal violet viability assay. Data are presented as mean of two independent experiments ± SEM. (**B**) Representative images of invading 3D non-MBM and MBM spheroids upon EHop-016 and vemurafenib treatment for 72 h, as indicated. Live cells are shown in green and dead cells in red. Scale bar: 100 µm. Magnification: 10 X. **ii)** Quantification of the 3D spheroid invasion assay. Data are presented as mean of at least three spheroids per cell line. (**C**) Transwell migration assay following 24 h treatment with the indicated inhibitors. 20,000 cells were seeded in each 8 µm pore size insert and were allowed to migrate towards conditioned media (supplemented with 10 % FCS).
In (A-B), MBM cells are displayed in warm colors, while non-MBM cells are shown in cool colors. In (C) pooled non-MBM cells are shown in blue and pooled MBM cells in red. Statistical significance was assessed using unpaired, two-tailed Student's t-test, (*) $p < 0.05$; (**) $p < 0.01$; (***) $p < 0.001$ (treated cells were compared to the untreated control cells). Abbreviations: combo = EHop-016 + vemurafenib treatment (at the respective concentrations).

3.6. Melanoma brain metastasis cells require higher levels of PI3K/AKT/mTOR inhibitors compared to extracranial cells

Inhibitors of the PI3K/AKT/mTOR pathway have not received thus far approval to be used in the clinics to treat melanoma patients due to the higher success rate of immunotherapies; however, they have been explored clinically (Yang et al., 2019). Given the importance of this signaling cascade in melanoma biology and resistance to therapy and because the RPPA revealed distinct protein expression related to this pathway (see **Figure 19**), the efficacy of PI3K/AKT/mTOR inhibitors on MBM growth was investigated. Viability assays using BKM120 (pan-class I PI3K inhibitor), GDC-0941 (potent and selective inhibitor of PI3Kα/δ) and rapamycin (allosteric mTOR inhibitor) were performed. These compounds did not have a dramatic effect on MBM proliferation; however, the MBM lines appeared slightly more resistant to the tested PI3K inhibitors compared to the non-MBM lines (**Figure 29 A-C**), which could be indicative of their aggressive nature. Moreover, the effect of rapamycin (1 μM) was tested on MBM and non-MBM 3D spheroids. Upon rapamycin treatment, melanoma cells were less invasive and spheroids shrank in size, but this was not specific to the MBM cells (**Figure 29 D**). This is in accordance to the varied mTOR signaling observed in **Figure 20**. In addition, PD-L1 levels were investigated in the MBM and non-MBM cell lines, as this protein is relevant to current anti-melanoma immunotherapies; however, PD-L1 expression was cell line-specific (**Figure 29 E**).

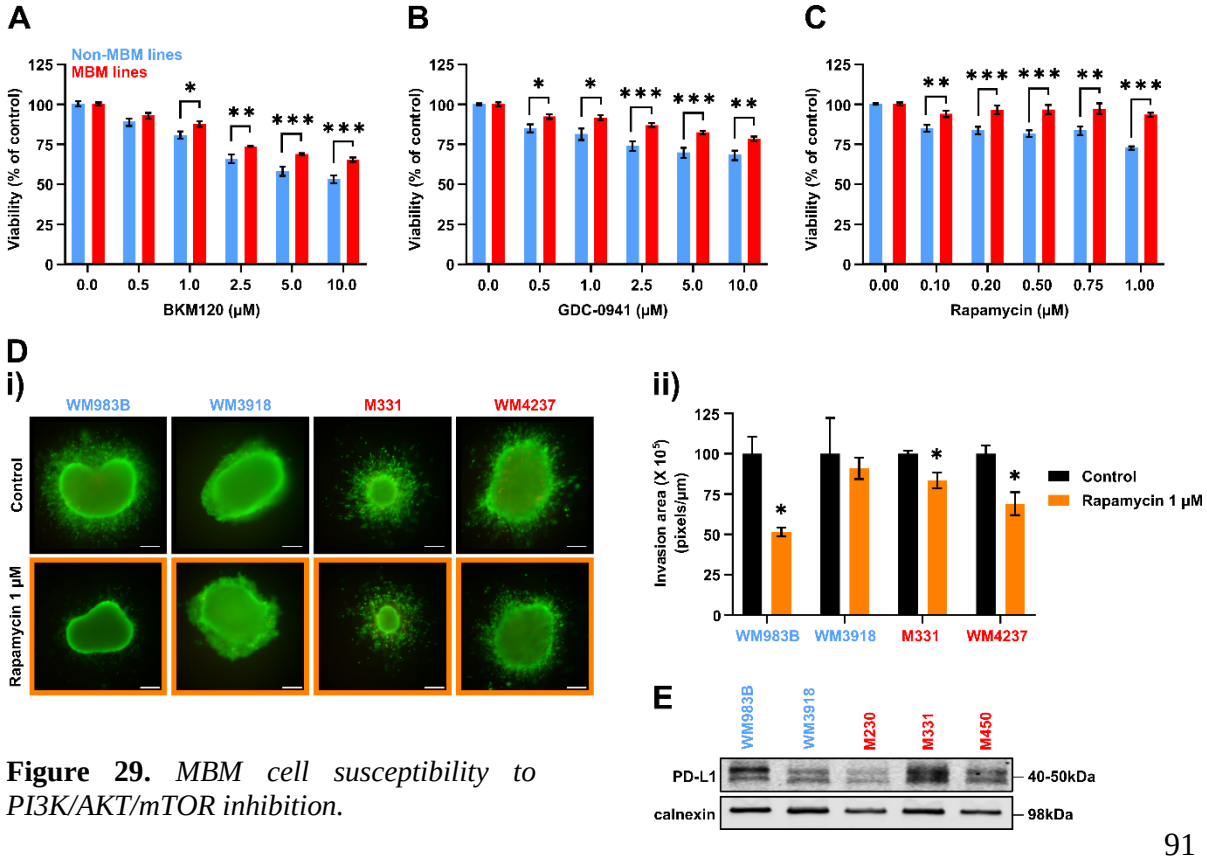

Figure 29. *MBM cell susceptibility to PI3K/AKT/mTOR inhibition.*

(**A-C**) Cell viability upon (**A**) BKM120, (**B**) GDC-0941 and (**C**) rapamycin treatment. 5,000 cells/well were seeded in 96-well plates and were allowed to adhere for 24 h before treatment. Cells were incubated with different concentrations of BKM120 (0-10 µM), GDC-0941 (0-10 µM) and rapamycin (0-1 µM) for 72 h prior to fluorescence measurement. Data are presented as mean of three independent experiments ± SEM (n=4 wells/each experiment). Pooled non-MBM cells are shown in blue and pooled MBM cells in red. Statistical significance was assessed using unpaired, two-tailed Student's t-test, (*) $p < 0.05$; (**) $p < 0.01$; (***) $p < 0.001$ (drug effects on MBM cells were compared to the ones on non-MBM cells). (**D**) **i)** Representative images of invading 3D non-MBM (WM983B, WM3918) and MBM spheroids (M331, WM4237) upon rapamycin treatment (1 µM) for 72 h. Live cells are shown in green and dead cells in red. Magnification: 10 X. Scale bar: 100 µm. **ii)** Quantification of the 3D spheroid invasion assay. (**E**) WB analysis of PD-L1 expression in non-MBM and MBM cells.
Non-MBM cells are labeled in blue and MBM cells in red throughout the figure. Data are presented as mean of at least three spheroids per cell line. Statistical significance was assessed using unpaired, two-tailed Student's t-test, (*) $p < 0.05$; (**) $p < 0.01$; (***) $p < 0.001$ (treated cells were compared to the untreated control cells).

3.7. RAC1 knockdown impairs melanoma brain metastasis cell proliferation, invasion and primary tumor growth

Due to our detection of high RAC1 in an extended panel of MBM lines (see **Figure 24 A**), our RPPA data leaning towards distinct adhesion/migration-related signaling (see **Figure 19 B**) and because of the established importance of RAC1 in melanoma biology (see sections **1.1.4.3** and **1.1.4.4**), we further focused our research efforts on investigating the role of RAC1 in MBM.

Compounds that block RAC1 are either unspecific (EHop-016, EHT 1864) or have a high IC50 (NSC23766); nevertheless, the potency and specificity of these inhibitors have improved (and will most likely improve) with each iteration (Bid et al., 2013). Thus, our next approach was to reduce RAC1 expression using shRNA lentiviral transduction in order to examine its function more specifically in MBM biology.

The introduction of shRNA into melanoma cells via lentiviral infection allows for stable, long-term KD of the targeted gene, strengthening the result reproducibility and excluding the need for multiple transfections. Moreover, stable KD cells can be used for *in vivo* studies, as opposed to transient knockdown cells (Moore et al., 2013).

Prior to further experimentation, RAC1 KD was confirmed by WB (**Figure 30**).

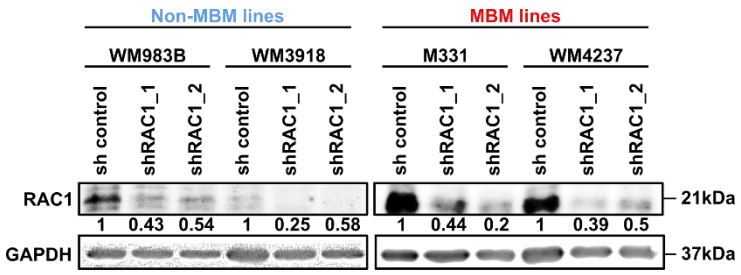

Figure 30. *RAC1 knockdown confirmation*. RAC1 KD was confirmed by WB analysis in MBM (M331, WM4237) and non-MBM cell lines (WM983B, WM3918) for two clones of shRNA against RAC1. Band quantitation was normalized to the loading control (GAPDH). Non-MBM lines are labeled in blue and MBM lines in red.

Upon RAC1 KD, an inhibition of proliferation was observed in both MBM and extracranial cell lines, suggesting that all investigated melanoma cells benefit from higher RAC1 to multiply (**Figure 31 A**; **Supplemental Table 2**). Interestingly, adhesion was only slightly affected, with the MBM lines WM4237 RAC1_1 and WM4237 shRAC1_2 being the most adhesive (**Figure 31 B**; **Supplemental Table 2**). Intriguingly, inhibition of RAC1 led to the stimulation of non-MBM cell migration towards conditioned medium, while the MBM cells were rather unaffected (**Figure 31 C**; **Supplemental Table 2**). Moreover, transwell assays using Matrigel™-coated inserts revealed a reduction in MBM invasion (**Figure 31 D**; **Supplemental Table 2**); the same effect was noticed in a 3D setting when RAC1 KD melanoma cells were allowed to invade a collagen I matrix (**Figure 31 E**; **Supplemental Table 2**). These results suggest that RAC1 is essential for the invasion potential of melanoma cell lines and that this is more evident in microenvironments that can simulate what happens *in vivo*. With this, we are in agreement with Shannan and colleagues who reported that 3D melanoma models confer an advantage over 2D models in understanding the effects of PI3K inhibition (Shannan et al., 2016).

To validate the importance of RAC1 *in vivo*, RAC1 KD WM4237 cells (sh control, shRAC1_1 and shRAC1_2) were injected s.c. into NSG mice, followed by the regular investigation of primary tumor growth and metastasis development for 58 days. Upon RAC1 KD, the primary tumor growth was hampered (**Figure 32 A-B**); additionally, there was a delay of about 8 days in tumor appearance in the shRAC1 group (**Figure 32 C**). Due to the aggressive nature and recurrence of the primary melanoma in the control group (despite primary tumor resection), the *in vivo* studies were halted prior to detection of brain metastases and earlier than expected for the model (data not shown; Valiente et al., 2020). Of note, the WM4237 RAC1 KD cells were subjected to multiple *ex vivo* manipulations (shRNA transfection, selection with puromycin, infection with luciferase reporter, positive fluorescent cell sorting) before being injected into mice; therefore, this approach could have altered to a certain extent the phenotype of the MBM cells, which is known to change with long-term culture (Valiente et al., 2020).

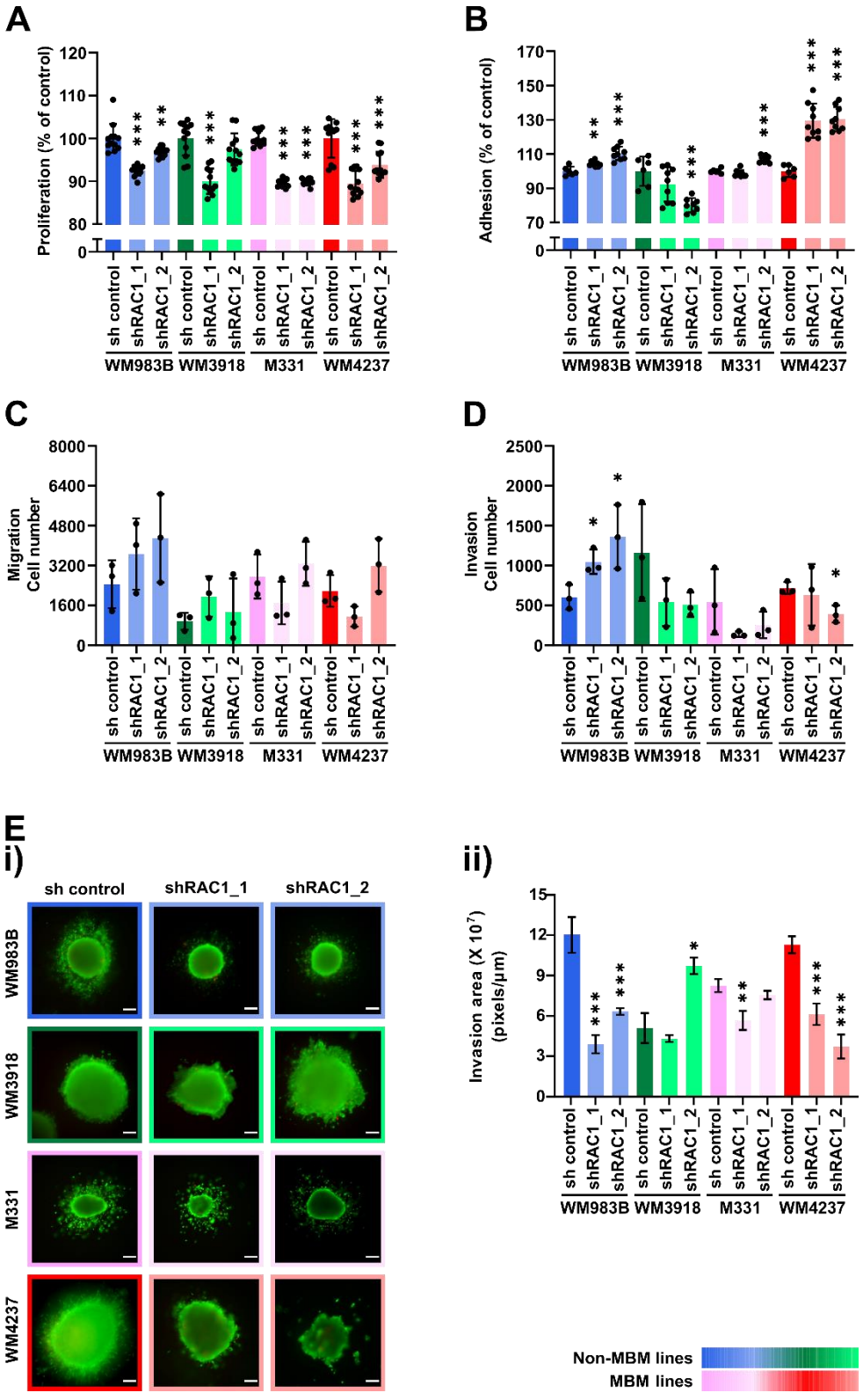

Figure 31. *RAC1 inhibition using shRNA impairs MBM proliferation and invasion.* (**A**) Proliferation of MBM versus non-MBM cell lines with RAC1 KD. 5,000 cells were seeded per condition and were allowed to grow for 72 h prior to fluorescence measurement. (**B**) Adhesion potential of MBM versus non-MBM lines with RAC1 KD. 20,000 cells were seeded per condition for 20 min prior to washing, followed by cell recovery for 4 h, staining and fluorescence measurement. (**C**) Migration potential of MBM versus non-MBM lines with RAC1 KD. 20,000 cells were seeded per insert and were allowed to migrate for 24 h towards conditioned medium supplemented with 10 % FCS. (**D**) Invasion potential of MBM versus non-MBM lines with RAC1 KD, assessed via transwell assay. 250,000 cells were seeded per each insert pre-coated with Matrigel™ and were allowed to invade the matrix for 24 h towards

conditioned medium supplemented with 20 % FCS. (**E**) Invasion potential of MBM versus non-MBM lines with RAC1 KD, assessed through 3D spheroid assay. **i)** Representative images of spheroids with RAC1 KD allowed to invade for 72 h prior to image acquisition. Live cells are shown in green and dead cells in red. Magnification: 10 X. Scale bar: 100 µm. **ii)** Quantification of the 3D spheroid invasion assay.
In (A-D), data are presented as mean ± SEM (N=3 separate experiments). Statistical significance was assessed using unpaired, two-tailed Student's t-test, (*) $p < 0.05$; (**) $p < 0.01$; (***) $p < 0.001$ (non-MBM lines were compared to the MBM lines). Each black dot indicates an individual value obtained from proliferation, adhesion, migration and transwell invasion experiments. In (E), data are presented as mean of at least three spheroids per cell line. Statistical significance was assessed using unpaired, two-tailed Student's t-test, (*) $p < 0.05$; (**) $p < 0.01$; (***) $p < 0.001$ (RAC1 KD cells were compared to the control cells). Non-MBM lines are shown in cool colors and MBM lines in warm colors.

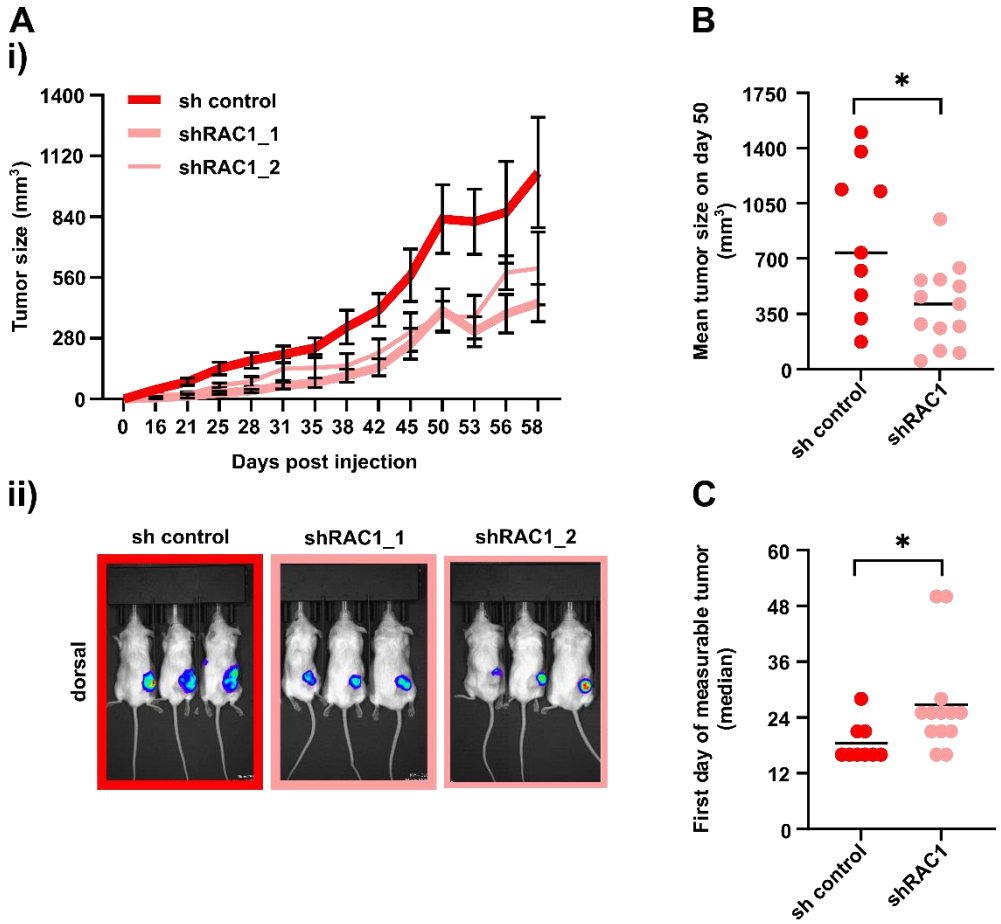

Figure 32. *RAC1 inhibition using shRNA reduces primary tumor growth.* (**A**) **i)** *In vivo* tumor growth of WM4237 MBM cells with shRAC1 KD. Cells were injected into NSG mice and primary tumor volumes were measured every 3-5 days for 58 days. Data are presented as mean ± SEM. **ii)** Whole mouse imaging (representative images) using the Xenogen IVIS 200 system after s.c. injection with WM4237 MBM cells upon RAC1 KD. (**B**) Mean tumor size of WM4237 MBM cells with shRAC1 KD on day 50. (**C**) Median day of appearance of first measurable primary tumor of WM4237 MBM cells with shRAC1 KD.
Mice groups: sh control (n=9), shRAC1_1 (n=9), shRAC1_2 (n=4). In (B-C), statistical significance was assessed using unpaired, two-tailed Student's t-test, (*) $p < 0.05$; (**) $p < 0.01$; (***) $p < 0.001$.

3.8. RAC1 knockdown and downstream signaling changes

Because RAC1 is known to interact with many signaling proteins (see sections **1.1.4.3** and **1.1.4.4**), the expression levels of other proteins involved in RAC1-related signaling and crosstalk pathways were next evaluated. MAPK and PI3K/AKT/mTOR-related signals are important for melanoma aggressive behavior (Meierjohann, 2017), as already discussed in section **1.1.4**. As indicators of pathway activity, phosphorylated and total levels of AKT and ERK were examined. As shown in **Figure 33**, the activity of AKT and ERK was reduced upon RAC1 KD in all cell lines; this coincided with the decreased proliferation shown in **Figure 31 A**. Additionally, an increase in phosphorylated PAK1 and JNK1 (RAC1 effectors) was observed in the MBM cells following RAC1 KD (see band quantitation), more noticeable in the WM4237 cell line, indicating the compensatory activation of downstream effectors. Together with the WB analyses shown in **Figure 26 C**, these data suggest a distinct PAK1/JNK1 signaling axis in the MBM lines investigated in this study.

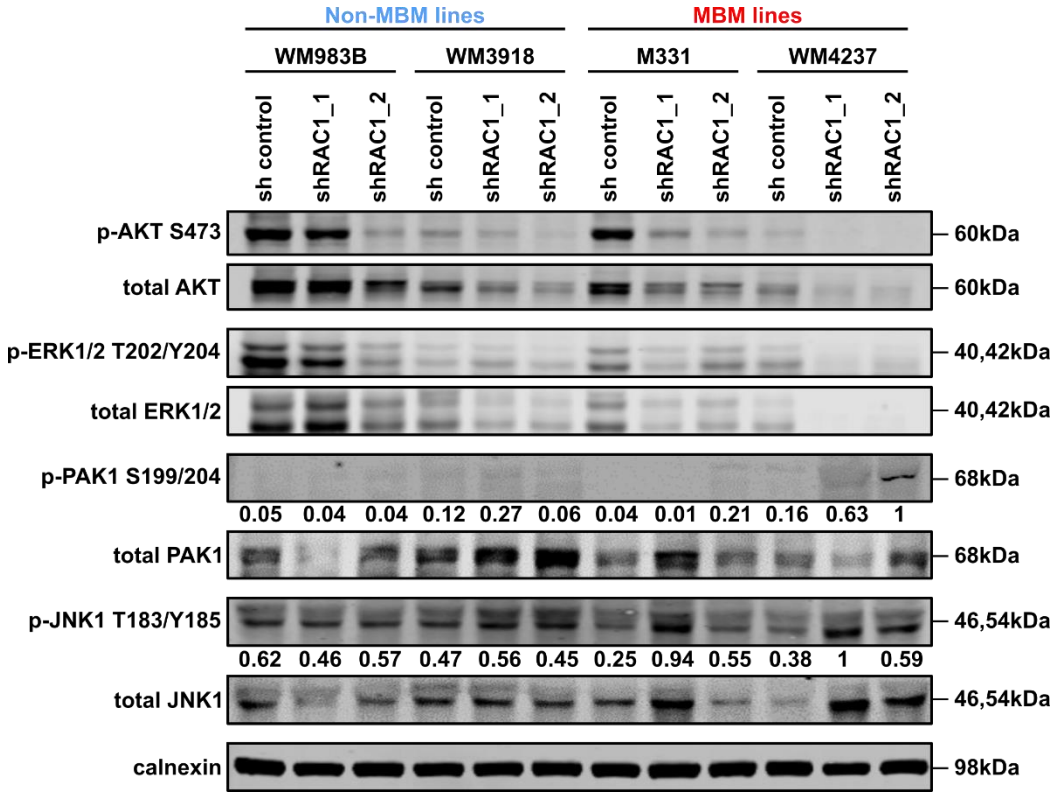

Figure 33. *RAC1 KD impairs PI3K and MAPK activity*. WB analyses for phosphorylated and total levels of AKT, ERK, PAK1 and JNK1 in non-MBM and MBM cell lines following RAC1 KD. Calnexin was used as loading control. Band quantitation for active PAK1 and JNK1 is shown as the ratio between phosphorylated and total protein. Non-MBM cell lines are labeled in blue and the MBM lines in red. "p" stands for phosphorylated protein.

3.9. The brain microenvironment plays a key role in melanoma brain metastasis proliferation, adhesion and migration

The tumor microenvironment (TME) of metastatic organs promotes the growth of disseminated cancer cells by creating a niche that enhances survival and proliferation signals (Klein et al., 2012). The involvement of the TME should thus not be omitted when evaluating the behavior of metastatic cancers *in vitro*. Astrocytes facilitate brain metastasis by stimulating cancer cell survival, stemness and trans-BBB migration (Zou et al., 2019). A recent study demonstrated that once they cross the BBB and reach the brain parenchyma, metastatic melanoma cells profit from the high fatty-acid brain microenvironment and start to proliferate (Zou et al., 2019).

Here, we used human astrocyte conditioned medium (HACM) to mimic elements of the brain microenvironment. Incubation of MBM and extracranial cells in HACM resulted in an increase in proliferation in all MBM lines (while for all non-MBM lines proliferation was decreased compared to control). However, this was significant for only two out of five MBM lines indicating some heterogeneity in this response (**Figure 34 A**). Our findings however are in agreement this those reported by Zou and colleagues for the WM4265-2 MBM line (Zou et al., 2019). Moreover, exposure of melanoma cells to HACM led to enhanced MBM adhesion (**Figure 34 B**) and migration (**Figure 34 C**). Additional migration studies were performed in fresh human astrocyte medium to confirm that the increase in MBM migration was due to the soluble factors in the HACM (**Figure 34 D**). Furthermore, WB analyses using cells incubated with HACM revealed an upregulation of RAC1 and PAK, most noticeable in the MBM lines (**Figure 34 E**). These observations indicate the important role of the brain microenvironment in promoting RAC1/PAK signaling and the distinct behavior of MBM cells compared to non-MBM cells.

Although rodent models do not entirely recapitulate human disease, human MBM cells can disseminate to the brain from a s.c. site in these models (Krepler et al., 2017; Valiente et al., 2020). Moreover, brain-derived soluble factors obtained from mice organ cultures can increase the migration potential of brain-metastasizing melanoma cells (Klein et al., 2012). Accordingly, we co-cultured melanoma cells with rat-derived neural cells (neurons and glia) for 72 h and observed enhanced MBM cell spread and adhesion, while the non-MBM cells remained rounded (**Figure 35**). RAC1 directs mesenchymal movement, characterized by elongated cellular morphology (Colón-Bolea et al., 2021). Therefore, the presence of stimulating brain cells along with the high RAC1 levels expressed by the MBM cells possibly conferred them a nourishing microenvironment that favored cell adhesion.

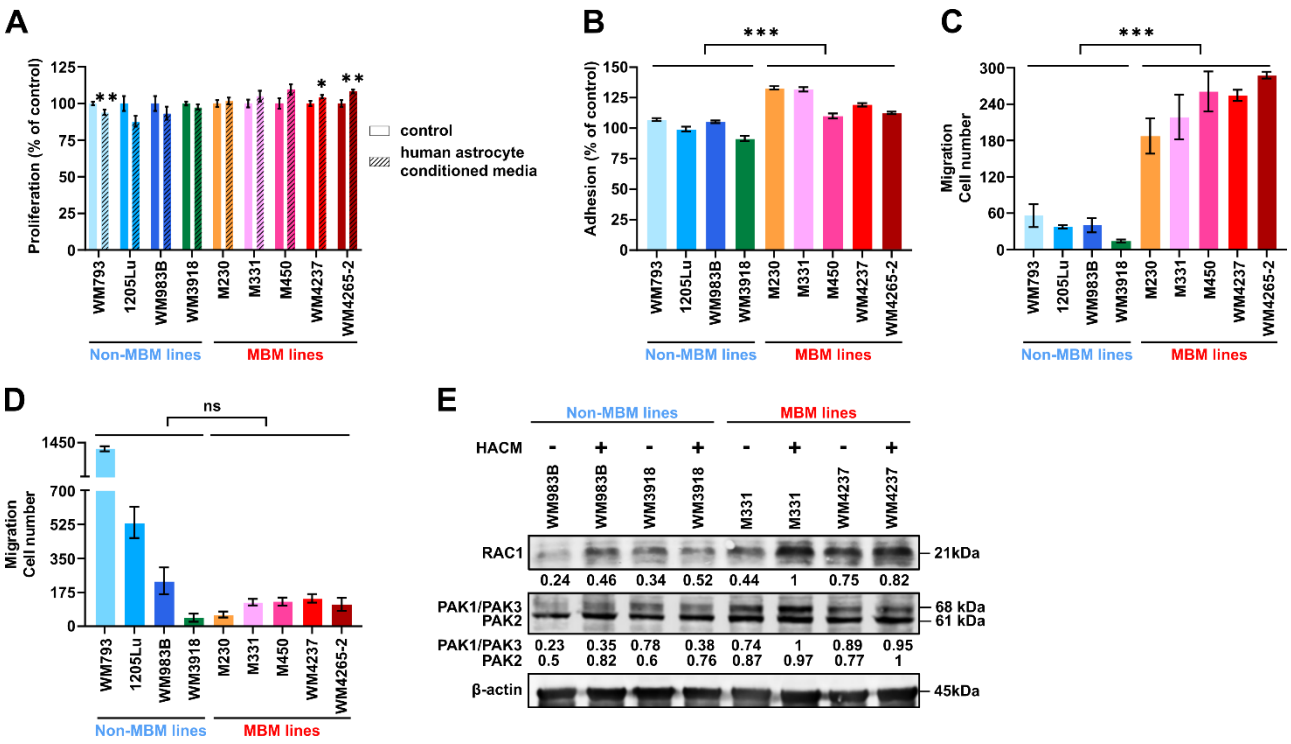

Figure 34. *Secreted factors by the brain microenvironment enhance MBM proliferation, adhesion and migration.* (**A**) The proliferation of two MBM lines is significantly enhanced in HACM. 5,000 cells/well were seeded and incubated for 72 h in fresh astrocyte medium (control) or HACM prior to fluorescence measurement. (**B**) Adhesion in HACM is elevated in MBM. 20,000 cells were seeded per condition for 20 min prior to washing, followed by cell recovery for 4 h, staining and fluorescence measurement. Values were normalized to the ones obtained from cells incubated in astrocyte fresh medium. (**C-D**) Migration of MBM lines is enhanced in HACM. 20,000 cells were seeded in transwell inserts and were allowed to migrate towards (**C**) HACM or (**D**) fresh astrocyte medium for 24 h prior to imaging. (**E**) RAC1 and PAK1 levels increase in the presence of HACM. WB analysis for RAC1 and PAK1/2/3 in non-MBM and MBM cells pre-incubated for 72 h in HACM. Band quantitation for RAC1 was normalized to the loading control β-actin.
In (A-B), data are presented as mean of n=4 wells/condition ± SEM, from three separate experiments. In (C-D), data are presented as mean ± SEM (N=3 independent experiments). In (E), data are representative of two separate experiments. Statistical significance was assessed using unpaired, two-tailed Student's t-test, (*) $p < 0.05$; (**) $p < 0.01$; (***) $p < 0.001$; (ns) = not significant (in (A) cells incubated in HACM were compared to cells incubated in control medium; in (B-D), non-MBM cells were compared to MBM cells). MBM cells are displayed in warm colors, while extracranial cells are shown in cool colors. Abbreviations: HACM = human astrocyte conditioned medium.

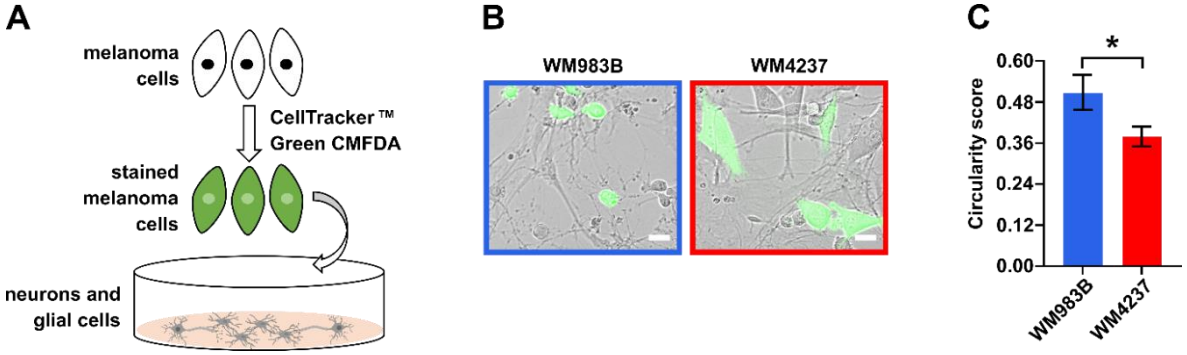

Figure 35. *MBM cell adhesion is increased in the presence of rat neuron and glia co-cultures.* (**A**) Melanoma cells were stained with CellTracker™ Green CMFDA prior to co-culturing them with rat-derived neurons and glial cells. (**B**) Representative images of stained melanoma cells (non-MBM

WM983B and MBM WM4237) co-cultured with unstained neurons and glial cells. Scale bar: 50 µm. Magnification: 20 X. (**C**) Quantification of the co-culture experiment. The circularity score applies to CellTracker™ Green CMFDA-positive melanoma cells. The higher the score, the more circular the melanoma cell. The bar graph displays mean ± SEM (n=32 WM983B cells and n=82 WM4237 cells). Statistical significance was assessed using unpaired, two-tailed Student's t-test, (*) $p < 0.05$; (**) $p < 0.01$; (***) $p < 0.001$.

3.10. The presence of brain secreted factors enhances the effect of RAC1 knockdown on melanoma brain metastasis

To assess the influence of RAC1 levels on MBM response to the brain microenvironment, cells with RAC1 KD were exposed to HACM. In the presence of RAC1 KD, MBM cell proliferation (**Figure 36 A**), adhesion (**Figure 36 B**) and migration (**Figure 36 C**) were no longer stimulated by human astrocyte-derived factors. Consequently, our observations thus far point to an increased aggressive behavior of the MBM cells in the presence of brain secreted factors, which is regulated by the expression levels of RAC1.

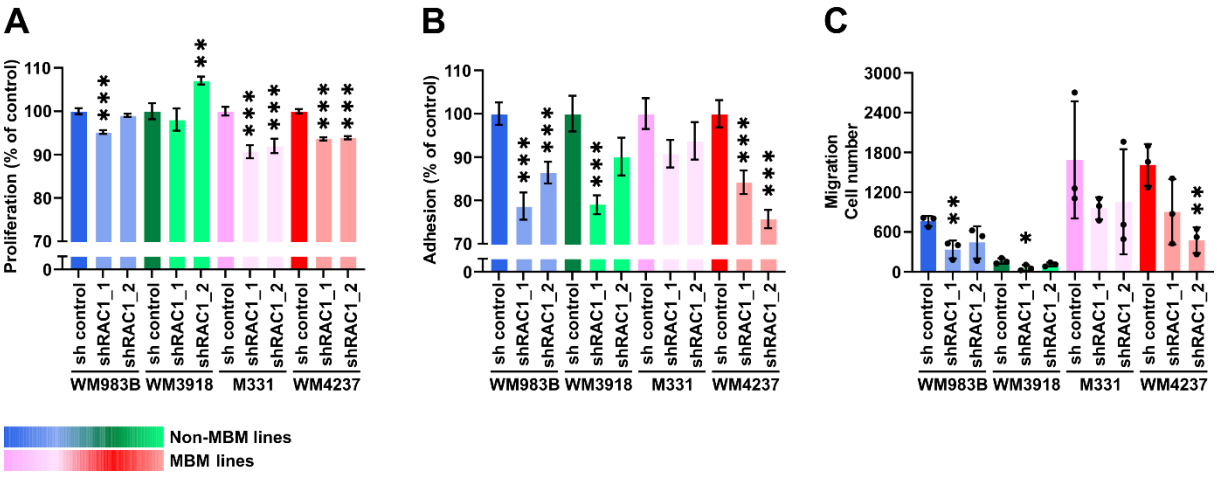

Figure 36. *The effects of brain-derived secreted factors on MBM are influenced by RAC1 levels.* (**A**) Proliferation of MBM cells in HACM is inhibited by RAC1 KD. 5,000 cells/well were seeded and incubated for 72 h in HACM prior to fluorescence measurement. (**B**) Adhesion of melanoma cells in HACM is inhibited by RAC1 KD. 20,000 cells were seeded per condition for 20 min prior to washing, followed by cell recovery for 4 h, staining and fluorescence measurement. (**C**) Migration of melanoma cells in HACM is inhibited by RAC1 KD. 20,000 cells were seeded in transwell inserts and were allowed to migrate towards astrocyte conditioned media for 24 h prior to imaging. Of note, additional FCS (20 %) was added in the bottom well to promote cell survival.
In (A-B), data are presented as mean of three independent experiments ± SEM (n=4 wells/experiment). In (C), black dots indicate an individual value obtained from different migration experiments. Data are presented as mean ± SEM (N=3 separate experiments). Statistical significance was assessed using unpaired, two-tailed Student's t-test, (*) $p < 0.05$; (**) $p < 0.01$; (***) $p < 0.001$ (RAC1 KD cells were compared to their respective sh control cells). Non-MBM cells are displayed in cool colors and MBM cells in warm colors.

3.11. Melanoma brain metastasis cell growth and invasion is altered in the presence of redox agents

RAC1 is known to mediate multiple cellular functions including ROS production (Ferro et al., 2012). Additionally, members of the NOX family are regulated by RAC proteins, as described in section **1.1.5**. Therefore, the expression levels of different NOX isoforms in MBM and extracranial cells was examined by RT-qPCR; interestingly, no distinct NOX expression pattern was detected in the MBM lines (**Figure 37 A**).

Therapeutic agents that lead to increased ROS levels can inhibit brain cancer growth (Rinaldi et al., 2016; Singer et al., 2015). Thus, the response of MBM cells to oxidants (H_2O_2), reducing agents (DTT), as well as antioxidants (mTEMPO, NAC) in standard 2D and 3D cultures was investigated. However, the observed effects were not MBM specific but rather cell-line specific (**Figure 37 B-C**). Since these are preliminary studies, we cannot fully conclude on the role of redox agents in MBM and additional experiments are needed (for instance by exposing the cells to brain secreted factors or to neurons and glial cells).

3.12. Melanoma brain metastasis cells are more susceptible to ferroptosis inducers than extracranial cells

With regard to anti-MBM therapeutic approaches, the present study demonstrated so far that the MBM cells are rather resistant to some ROS agents (see **Figure 37 B-C**), PI3K/AKT/mTOR inhibitors (see **Figure 29**) and even some MAPK inhibitors (see **Figure 27 D-E**). Ferroptosis is a form of redox-driven programmed cell death that is different from apoptosis and can be fatal even to drug-resistant cells (Feng et al., 2020). Given that RAC1 is involved in the regulation of redox processes and in an attempt to target the MBM cells therapeutically, we tested the effectiveness of ferroptosis inducers against MBM. Accordingly, MBM and non-MBM cells were treated with erastin (cystine/glutamate antiporter inhibitor), RSL3 (GPX4 inhibitor) and BSO (glutamate cysteine ligase inhibitor) for 48-72 h (**Figure 38 A-C**). An increased susceptibility to all the aforementioned ferroptosis inducers was observed in the MBM lines compared to the extracranial lines, especially at higher drug doses. Moreover, this effect could be reversed upon pre-incubation with ferrostatin-1 (Fer-1), a potent and selective inhibitor of ferroptosis (**Figure 38 D**).

Evidently, MBM enhanced sensitivity to ferroptotic cell death needs further investigation. Identifying MBM-specific signaling molecules involved in ferroptosis might be a first step into this direction. Further studies aiming to unravel a possible role of RAC1 in ferroptosis are ongoing.

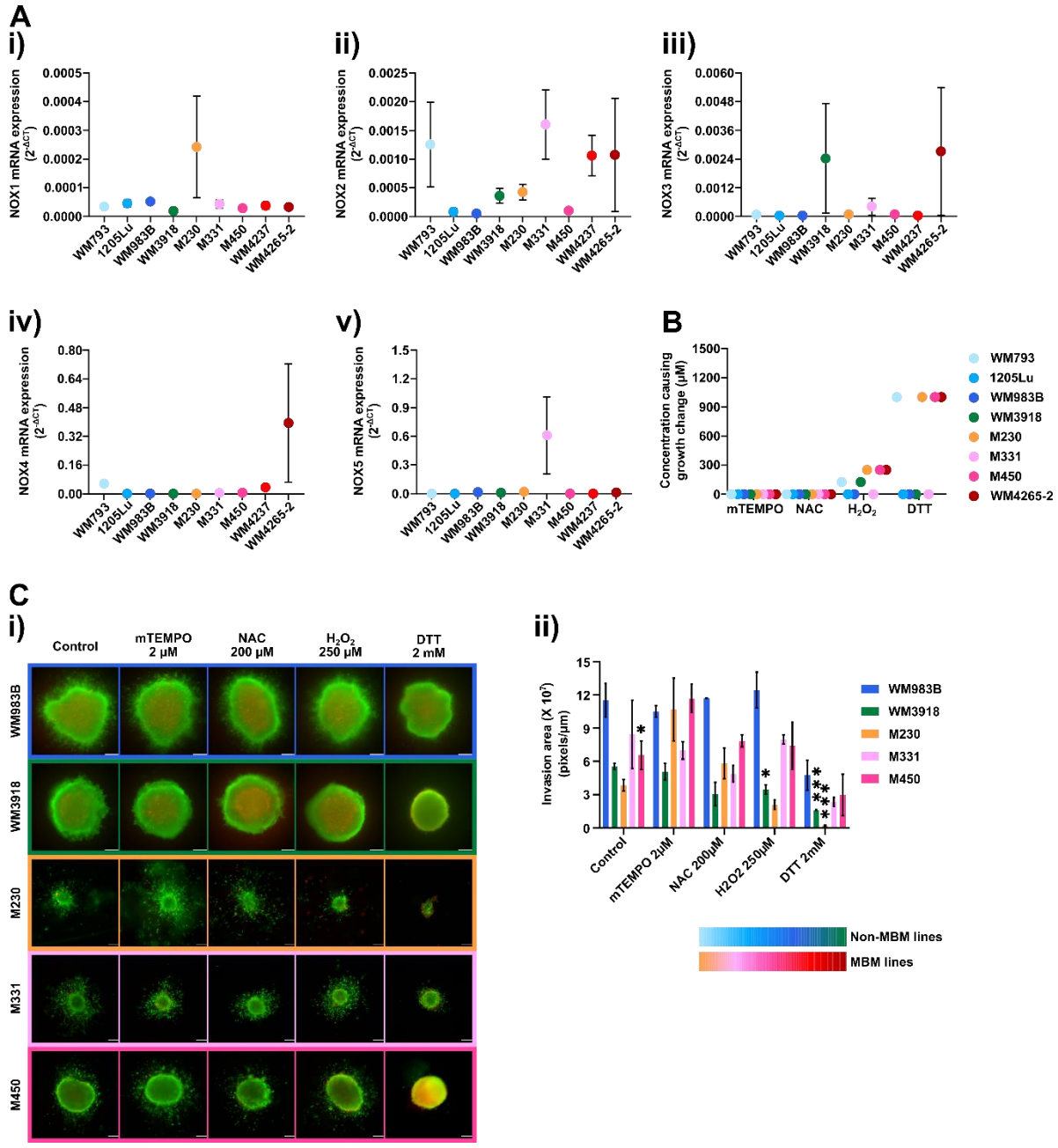

Figure 37. *High RAC1 expression in MBM does not clearly affect redox-driven processes in preliminary studies.* (**A**) mRNA expression of (**i**) NOX1, (**ii**) NOX2, (**iii**) NOX3, (**iv**) NOX4 and (**v**) NOX5 in non-MBM and MBM lines, quantified by RT-qPCR. Data are normalized to the expression of the control gene TBP and are presented as mean ± SEM (N=3 independent experiments). (**B**) Viability assay upon incubation with redox-altering agents. 5,000 cells were treated with ROS agents (mTEMPO, NAC, H_2O_2 and DTT) for 48 h prior to fluorescence measurement. Data are presented as drug dose upon which a 20 % change in proliferation was detected. Data points were obtained from n=4 wells/condition, from over 10 separate experiments. (**C**) Redox-altering agents' impact on melanoma invasion. **i)** Representative images of at least three spheroids upon treatment with the indicated agents. Live cells are shown in green and dead cells in red. Scale bar: 100 μm. Magnification: 10 X. **ii)** Quantification of the 3D spheroid invasion assay. Statistical significance was assessed using unpaired, two-tailed Student's t-test, (*) $p < 0.05$; (**) $p < 0.01$; (***) $p < 0.001$ (treated cells were compared to untreated cells).
Non-MBM cells are marked with cool colors, while MBM cells are shown in warm colors. Abbreviations: DTT = dithiothreitol; H_2O_2 = hydrogen peroxide; mTEMPO = mitoTEMPO, mitochondria-targeted antioxidant; NAC = N-acetyl cysteine.

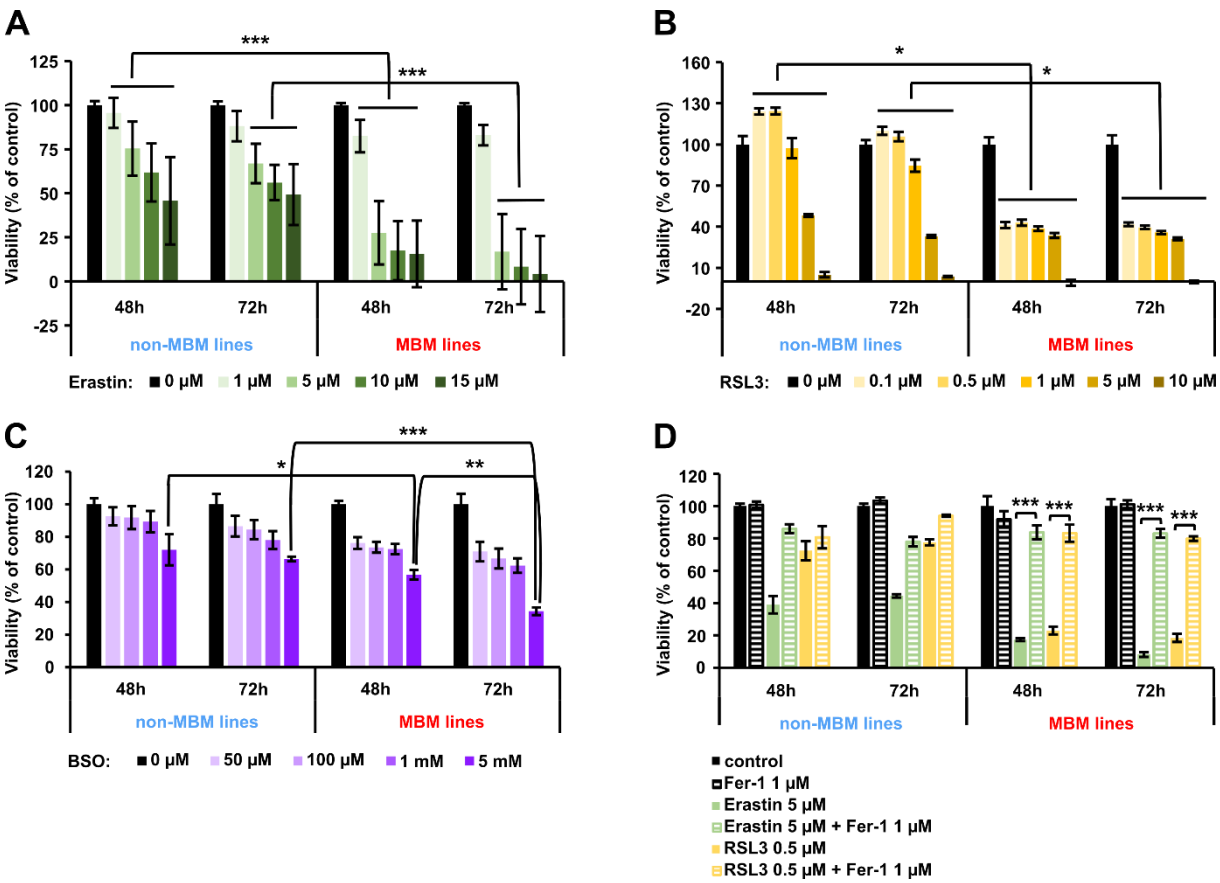

Figure 38. *MBM cells are more sensitive to ferroptosis inducers than non-MBM cells.* Viability of pooled non-MBM and pooled MBM cells upon (**A**) erastin, (**B**) RSL3 and (**C**) BSO. (**D**) Erastin and RSL3 effects were recovered in the presence of Fer-1. 5,000 cells/well were seeded in 96-well plates and were allowed to adhere for 24 h before treatment. Cells were incubated with different concentrations of ferroptosis inducers (as indicated) for 48-72 h prior to fluorescence measurement.
Data are presented as mean ± SEM (N=3 separate experiments). Statistical significance was assessed using unpaired, two-tailed Student's t-test, (*) $p < 0.05$; (**) $p < 0.01$; (***) $p < 0.001$. Non-MBM lines are labeled in blue and MBM lines in red.

4. DISCUSSION

Metastasis is cancer's hallmark and is responsible for most cancer-related deaths (Fares et al., 2020). To quote Siddhartha Mukherjee in *The Emperor of All Maladies*: "Cancer, even when it begins locally, is inevitably waiting to explode out of its confinement."; this is also the case for melanoma, a highly metastatic type of cancer and the deadliest of skin cancers. Although anti-melanoma therapies have come a long way in the last decade and provide long term results in some cases, many patients still succumb to the disease (Rebecca et al., 2020). Brain metastases in particular have a high impact on the mortality and quality of life of patients with advanced melanoma. The remarkable advances in anti-melanoma therapies helped increase the 1-year overall survival rate of MBM patients from 20–25 % to almost 85 % (mostly in asymptomatic patients) (Salvati et al., 2020). Notwithstanding, successful, lifelong treatment of patients with MBM remains a true challenge and we have much to yet understand about brain lesions.

We investigated a previously uncharacterized panel of human-derived MBM cell lines in order to unravel MBM-specific biological processes and novel therapeutic targets. Our observations point to MBM-specific *in vitro* functional properties and signaling patterns, irrespective of genetic background, and this is in agreement with many other studies on MBM so far (Bucheit et al., 2014; Chen et al., 2014; Cho et al., 2015; Davies et al., 2009; Kircher et al., 2019), suggesting that genetically diverse cells can migrate to the brain but the metastatic organ then confers specific tumor cell properties.

4.1. Melanoma brain metastasis cells display a slow proliferation rate that can be enhanced in the presence of growth factors

Our panel of MBM lines displayed a slower *in vitro* proliferation rate compared to our extracranial lines; this could be the result of a dormant phenotype that BM cells engage prior to expansion and brain colonization (Boire et al., 2019). The slow proliferation of our MBM cells could be enhanced by the addition of insulin but not IGF-1 or other nutrients such as glucose, indicating a selective response to TME factors. The beneficial effects of insulin on cell proliferation have been described over 40 years ago (Straus, 1981) and researchers use insulin as a growth supplement for cell culture media on a daily basis. Therefore, why in our case only MBM growth was significantly stimulated by the addition of this growth factor is unclear. One of the possible explanations is the upregulation of RAC1 in these cell lines, which was shown to have a crucial role in insulin-stimulated glucose uptake in skeletal muscle (Satoh and

Takenaka, 2019; Ueda et al., 2010). Moreover, by analyzing the insulin plasma values in various types of brain tumors, Alexandru and colleagues demonstrated that the values of this growth factor were enhanced in brain metastases (Alexandru et al., 2014). It is therefore conceivable that the addition of insulin to the culture media simulated to a certain extent the brain microenvironment, making the MBM cells more proliferative.

Melanoma growth *in vitro* is dependent on high glucose levels (Ferguson et al., 2017); however, upon incubation with 50 mM glucose (double the amount provided in the commercial DMEM medium), the proliferation of our melanoma lines was not enhanced. Some melanoma lines are also addicted to glutamine (Qin et al., 2010), which was also the case for our extracranial lines but not our MBM lines, suggesting that the MBM cell proliferation is rather dependent on other growth factors.

4.2. Melanoma brain metastasis cells display unique signaling properties

We observed distinct expression of migration/adhesion-related signals in our MBM lines using both western blot analyses and RPPA. Notably, RAC1 was upregulated in our panel of MBM lines. RAC1 is a member of the RHO family of small GTPases, along with CDC42, RhoA and other RAC isoforms; this family of proteins plays a crucial role in cancer metastasis (Maldonado et al., 2020). According to our analyses, CDC42, RhoA and RAC3 were not distinctly expressed in our panel of MBM lines, indicating that higher RAC1 levels in these particular cells are unique and not dependent on or causing changes in other RHO family members.

RAC1 affects signaling pathways such as MAPK, PI3K/AKT/mTOR or JNK; therefore, it plays key roles in regulating proliferation, survival and metastasis-associated processes (Bosco et al., 2009; Cannon et al., 2020; Vu et al., 2015). Moreover, RAC1 regulates DNA damage response and protects keratinocytes from apoptosis caused by UV radiation (Deshmukh et al., 2017). In terms of its clinical relevance, RAC1 non-silent mutations can be found in about 5 % of melanomas and the RAC1*P29S* mutation is the third most frequent hotspot mutation in sun-exposed melanomas (Hodis et al., 2012). When compared to our MBM lines, three out of four of our extracranial cell lines had a high gain copy number in RAC1 (Garman et al., 2017, **Table 24**) but not higher RAC1 protein expression. The elevated RAC1 expression in our MBM lines in the absence of RAC1 genetic modifications suggests that differences in protein expression could also be indicative of aggressive disease. Post-translational modifications of RAC1 can also regulate the function of this enigmatic protein. The reported post-translational modifications of RAC1 include ubiquitination, adenylylation, lipidation and even

phosphorylation. RAC1 can be phosphorylated at multiple sites by SRC, FAK, AKT or ERK which hinders its GTP binding activity. However, there is currently no pathogenic evidence to support the role of these phosphorylations in cancer development (Abdrabou and Wang, 2018).

As a GTPase, RAC1 cycles between a GTP-bound active and a GDP-bound inactive conformation in order to activate effector proteins and regulate cellular processes. Despite high RAC1 expression levels (confirmed in both 2D and 3D lysates), we could not validate high RAC1 activity in our MBM lines grown *in vitro*; however, this does not negate the importance of RAC1 in MBM, as GTP-independent functions have also been reported (Saci et al., 2011). It is also possible that RAC1 is primed for activation in the brain microenvironment under the right stimulatory environment, which would explain why we detected high levels of RAC1 protein expression but not activity in standard melanoma monoculture. More sensitive methods (such as single cell imaging using sensors for RAC1 activity) might confirm high RAC1 activity in the MBM cells. It would also be important to determine RAC1 activity in MBM cells upon insulin treatment or in the presence of brain-derived soluble factors.

We also observed lower FAK and SRC levels in the MBM cell lines compared to extracranial lines, suggesting that the aggressive behavior of these two groups of cell lines is driven by distinct molecular signals. Moreover, four out of five investigated MBM lines displayed upregulation of PAK1 and JNK1. Of note, the MBM line that displayed the lowest PAK1 protein expression levels (M450) was also our most highly proliferative MBM line in standard culture. Given that RAC1/PAK1/JNK1 signaling is important for neuronal development, a brain-induced reprogramming of metastasized melanoma cells with an acquisition of neuronal features could likely occur, as previously postulated by others and supported by the neural crest origin of melanoma cells (de Curtis, 2014; Diener and Sommer, 2021).

4.3. The particular features of the brain microenvironment influence melanoma brain metastasis aggressive behavior

Cancer metastasis is dependent on the interplay between tumor cells and the microenvironment of distal organs, as proposed by the "seed and soil" hypothesis (Paget, 1853; Zou et al., 2019). The microenvironment, or "soil," not only modulates metastatic tumor cell expansion but also contributes to therapy resistance. The microenvironment of the brain is unique; it contains brain-specific cell types such as neurons and supporting glial cells (Zou et al., 2019). Astrocytes are the most numerous glial cells in the brain (Brandao et al., 2019); they engage with invading cancer cells in the early stages of brain colonization in experimental mice and this contact persists throughout the development of the metastatic lesions (Kienast et al., 2010; Valiente et

al., 2014). In spite of their unquestionable aggressiveness, the MBM cell lines investigated in this study did not display higher adhesion, migration or invasion potential than the non-MBM lines under standard, *in vitro* conditions. However, exposure of these cells to astrocyte-derived soluble factors significantly enhanced MBM aggressive behavior, i.e. higher proliferation, adhesion and migration ability were observed, compared to the extracranial cells. Moreover, by incubating our MBM cells in human astrocyte conditioned media, we were able to enhance total RAC1 and PAK levels. These results indicate that MBM cells are not more mobile but rather they need a proper microenvironment to reach the brain and thrive. It is therefore possible that the MBM cells undergo growth arrest *in vitro* until the appropriate growth signals (insulin, brain-derived soluble factors) are present (Izraely et al., 2011) (**Figure 39**). Loss or downregulation of FAK signaling might be partial evidence for this quiescent state (Aguirre-Ghiso, 2007; Ossowski and Aguirre-Ghiso, 2010), which was also the case for our MBM cells.

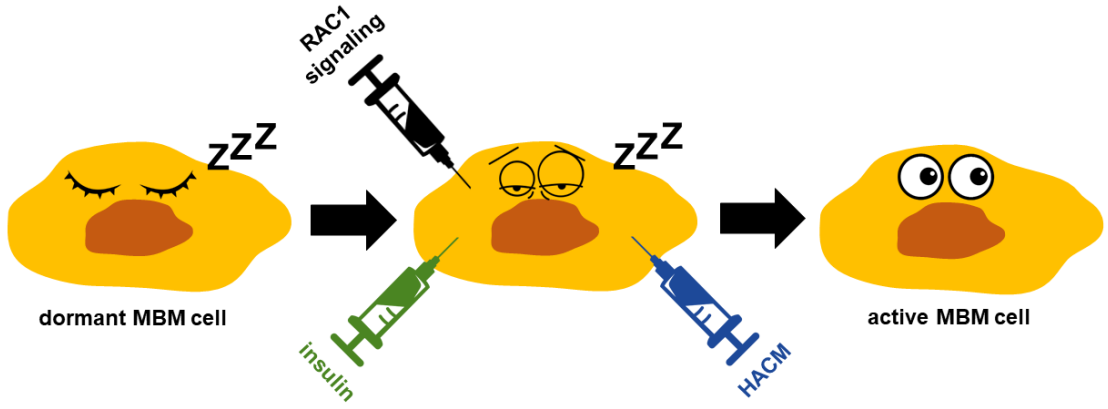

Figure 39. *MBM cells require brain-derived or specific growth signals to become active in vitro.* Dormant MBM cells dependent on RAC1 signaling can become active in the presence of insulin or HACM. Abbreviations: HACM = human astrocyte conditioned media.

4.4. RAC1 is associated with melanoma brain metastasis aggressiveness

When we inhibited RAC1 by shRNA lentiviral transfection, MBM proliferation was slightly altered and migration was not affected, suggesting that RAC1 signaling in this setting was not essential. However, in the presence of support matrices, MBM cell invasion was dramatically reduced, suggesting a pivotal role of RAC1 in the aggressive behavior of MBM cells in microenvironments recapitulating elements of the *in vivo* setting.

To expand on the important role of the microenvironment in MBM biology, we exposed our shRAC1 KD cell lines to human astrocyte-derived soluble factors and we were able to decrease MBM cell proliferation, adhesion and migration, indicating that enhanced RAC1 levels are indispensable for maintaining MBM cell aggressiveness. We also explored the effects of RAC1

KD on additional proteins important for melanoma pathobiology. Accordingly, we performed western blot analyses examining total and phosphorylated ERK (indicator of MAPK pathway activity) and AKT (indicator of PI3K/AKT/mTOR pathway activity) and observed a decrease in ERK and AKT expression and activity directly proportional to the lower total RAC1 levels. It is possible that the effects of RAC1 KD on cell proliferation, adhesion, and migration are a result of a decrease in MAPK and PI3K signaling and not just RAC1 since these pathways cross-regulate each other. Nevertheless, what these studies indicate is the important role of RAC1 levels in melanoma and not just its mutational status.

We also observed a compensatory increase in PAK and JNK1 activity in our MBM cells upon RAC1 KD, once again suggesting distinct RAC1/PAK1/JNK1 signaling in this panel of cell lines. These observations highlight the key role of RAC1 in MBM, possibly placing it *in the driver's seat for melanoma*, as stated by Machesky and Sansom (Machesky and Sansom, 2012).

To confirm that RAC1 levels are important to MBM *in vivo*, we used a newly established human-derived MBM PDX model that spontaneously metastasizes to the brain following s.c. injection (Krepler et al., 2017). This model is unique in replicating the human metastatic process (Valiente et al., 2020). By inoculating WM4237 RAC1 KD cells into NSG mice, we noticed a decrease in primary tumor growth, compared to the control group. In addition, we observed a delay in primary tumor appearance, proving the importance of RAC1 for WM4237 aggressive behavior *in vivo*. Regarding the metastatic process, this PDX model requires around 17 weeks for the brain lesions to appear (Valiente et al., 2020). However, for the welfare of the animals, we were obligated to discontinue the *in vivo* experiment early and, therefore, we could not detect brain metastases. Nevertheless, to our knowledge, this was the first attempt to use such a model for biological studies and we advise that it is better used with minimal *ex vivo* cell handling and using low cell passage numbers to maintain MBM-like properties. Our observations also indicate that this model could be improved by providing the MBM cells *ex vivo* conditions that simulate the brain microenvironment (brain-derived soluble factors, insulin) prior to their inoculation into mice. Notwithstanding, this *in vivo* model confirmed the important role of high RAC1 levels for MBM *in vivo*. The development of additional models with spontaneous metastatic potential to the brain will undoubtedly improve our understanding of MBM. Of note, long-term RAC1 KD without continuous antibiotic selection can allow cells with higher RAC1 levels to take over; therefore, our observations over 58 days *in vivo* can underestimate the role of RAC1 in MBM over time.

4.5. Prospective anti-melanoma brain metastasis therapies

Regarding modern anti-melanoma therapies, we observed cell-line specific PD-L1 expression, giving no indication that our MBM cells would respond better to anti-PD-1/PD-L1 immunotherapy than the extracranial cells (Newell et al., 2022; Sunshine et al., 2017); however, many other factors regulate immune surveillance, therefore this research area needs more exploration, especially in the presence of a brain-like environment. Additionally, we noticed an increased resistance to BRAF/MEK inhibitors, the standard treatment for BRAF*V600E*-mutant advanced melanoma. This resistance could be explained by the additional mutations (*NRAS*, *MAP2K1* mutations) that our panel of MBM harbors (Kakadia et al., 2018). On the other hand, when we combined the clinically relevant BRAF*V600E* inhibitor vemurafenib with the RAC inhibitor EHop-016, we observed additive anti-MBM effects in both 2D and 3D cultures, opening the door to potentially more efficient anti-MBM therapies for BRAF-mutated melanomas that do not respond to anti-BRAF/MEK targeted therapy. Nevertheless, EHop-016 is a non-specific RAC inhibitor that can target all RAC isoforms and CDC42 as well (Cannon et al., 2020); thus, additional studies are needed to dissect its inhibiting properties *in vitro* and *in vivo*. NSC23766, a specific RAC1 inhibitor might provide another option; however, we observed in our panel of MBM lines an increased resistance at physiological doses of NSC23766, as also reported by others (Liang et al., 2021). PAK inhibitors, on the other hand, are well tolerated thus far and could provide a viable clinical option (Chung et al., 2019; Semenova and Chernoff, 2017).

We also observed an enhanced resistance to PI3K/AKT/mTOR inhibition in our MBM cells. Due to the high toxicity levels and inefficiency in downregulating the pathway to levels required for tumor responses, the majority of the inhibitors of this pathway were also unsuccessful in clinical trials (Wright et al., 2021). However, a recent study reports an increased efficacy of the combination of MAPK and PI3K inhibitors in an *in vivo* melanoma model (Aasen et al., 2019), indicating that additional studies could enable the development of novel targeted anti-melanoma therapies in the future. While targeting MBM in the clinic with new agents will take time and effort, the knowledge that RAC1 is important for MBM may unravel it as a new biomarker of aggressive disease and help in patient subtyping. Brain imaging is not a routine practice for melanoma patients and patients who are at risk for MBM could benefit from more frequent brain monitoring.

In addition to targeting signaling pathways and immune-based processes, novel therapies can also come from a better understanding of cancer biology and its weaknesses. For example, ferroptosis is a newly identified form of iron-dependent cell death that differs from other types

of regulated cell death in terms of morphology, biochemistry and genetics (Talty and Bosenberg, 2021). To investigate if ferroptosis inducers would be a good treatment option for our drug-resistant MBM cells, we treated these cells with erastin, RSL3 and BSO and we detected an increased sensitivity to all these compounds compared to the extracranial cells. Additional investigations are by all means needed; however, to our knowledge, we are the first group to report an increased susceptibility of MBM cells to ferroptotic cell death.

Forthcoming research could explore the efficacy of combining ferroptosis inducers and RAC1 inhibitors (using physiological doses) in order to fully eradicate MBM cells. Moreover, it will be important that further investigations examine the effects of combining insulin and brain-derived soluble factors on MBM biology. Furthermore, future studies into the involvement of ROS and RAC1 in melanoma dissemination and MBM generation should certainly shed light into the plasticity of melanoma cells in different environments and how tumor cell metabolism can be harnessed for therapeutic purposes.

Finally, the MBM field is in its infancy and few models are available for preclinical interrogation. We are aware that we have a limited panel of cell lines in our study and this may only represent a subset of melanoma patients with MBM. As these models of MBM disease increase in number, in the future we will have a better understanding of MBM biology and which targets to prioritize to reach most patients. For the time being, given the important role of RAC1 mutations in melanoma and our finding that high RAC1 levels are essential for a random panel of genetically diverse MBM lines, we recommend that RAC1 and its signaling are given more clinical attention.

4.6. Conclusions

The present study aimed to identify novel therapeutic targets that could improve current anti-MBM treatments and is a small step in the direction of better understanding melanoma-associated brain lesions. The molecular characterization of MBM and the understanding of how the metastatic microenvironment alter tumor biology are crucial for better managing patients with advanced disease. We report here that MBM cells can retain a slow proliferative phenotype once removed from the brain and that RAC1 expression is increased in a random panel of genetically diverse cell lines and that RAC1 signaling in MBM involves PAK1 and JNK1. In addition, MBM reliance on the RAC1/PAK pathway is most strongly observed in brain-like microenvironments. Overall, there is substantial evidence pointing to a key role for RAC1 signaling in melanoma; nonetheless, to our knowledge, we are the first group to acknowledge its importance in MBM aggressive behavior.

The main findings of this study are summarized in **Figure 40**.

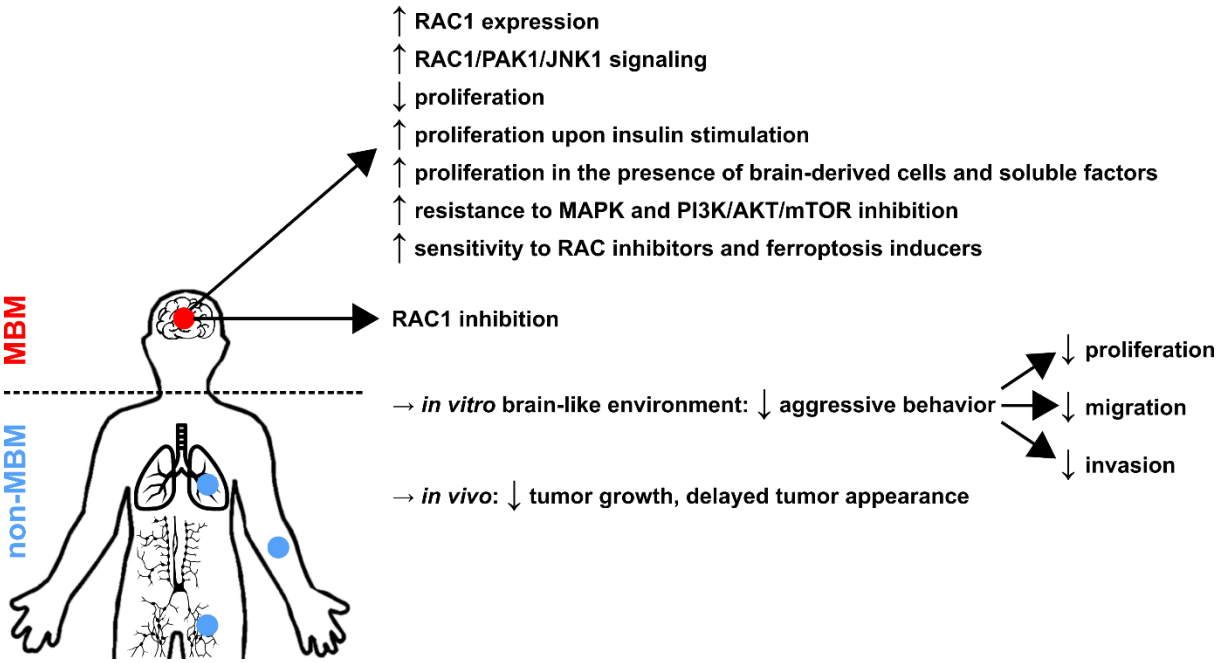

Figure 40. *Melanoma brain metastases – an overview of major findings.* MBM cell lines (in red) display increased RAC1/PAK1/JNK1 levels, compared to non-MBM lines (in blue). Moreover, MBM cells exhibit low proliferation in standard *in vitro* culture, which could be enhanced by brain soluble factors, the presence of brain-derived cells or insulin. Regarding therapeutic properties, MBM cells are resistant to MAPK and PI3K/AKT/mTOR inhibitors, but they are more sensitive in combination with RAC inhibitors and also to ferroptosis inducers than their extracranial counterparts. RAC1 inhibition using shRNA lentiviral transduction leads to a reduced aggressive behavior of the MBM cells, provided they are exposed to a brain-like microenvironment. Moreover, RAC1 KD results in decreased *in vivo* tumor growth.

Importantly, this study shows that there are options for patients with MBM in the foreseeable future and we are confident that as our knowledge evolves, we will be able to bring MBM to the level of manageable disease.

REFERENCES

Aasen, S. N., H. Parajuli, T. Hoang, Z. Feng, K. Stokke, J. Wang, K. Roy, R. Bjerkvig, S. Knappskog and F. Thorsen (2019). "Effective Treatment of Metastatic Melanoma by Combining MAPK and PI3K Signaling Pathway Inhibitors." Int J Mol Sci **20**(17): 4235.

Abate-Daga, D., M. C. Ramello, I. Smalley, P. A. Forsyth and K. Smalley. (2018). "The biology and therapeutic management of melanoma brain metastases." Biochem Pharmacol **153**: 35–45.

Abdrabou, A., and Z. Wang (2018). "Post-Translational Modification and Subcellular Distribution of Rac1: An Update." Cells **7**(12): 263.

Achrol, A. S., R. C. Rennert, C. Anders, R. Soffietti, M. S. Ahluwalia, L. Nayak, S. Peters, N. D. Arvold, G. R. Harsh, P. S. Steeg and S. D. Chang (2019). "Brain metastases." Nat Rev Dis Primers **5**(1): 5.

Active RAC1 Pull-Down and Detection Kit. https://www.thermofisher.com/document-connect/document-connect.html?url=https%3A%2F%2Fassets.thermofisher.com%2FTFS-Assets%2FLSG%2Fmanuals%2FMAN0011728_Active_Rac1_PullDown_Detect_UG.pdf&title=VXNlciBHdWlkZTogIEFjdGl2ZSBSYWMxIFB1bGwtRG93biBhbmQgRGV0ZWN0aW9uIEtpdA

Adler, N. R., R. Wolfe, J. W. Kelly, A. Haydon, G. A. McArthur, C. A. McLean and V. J. Mar (2017). "Tumour mutation status and sites of metastasis in patients with cutaneous melanoma." Br J Cancer **117**(7): 1026-1035.

Aguirre-Ghiso, J. A. (2007). "Models, mechanisms and clinical evidence for cancer dormancy." Nat Rev Cancer **7**(11): 834-46.

Aguissa-Touré, A. H. and G. Li (2012). "Genetic alterations of PTEN in human melanoma." Cell Mol Life Sci **69**(9): 1475-1491.

Albino, A. P., R. Le Strange, A. I. Oliff, M. E. Furth and L. J. Old (1984). "Transforming ras genes from human melanoma: a manifestation of tumour heterogeneity?" Nature **308**(5954): 69-72.

Alexandru, O., L. Ene, O. S. Purcaru, D. E. Tache, A. Popescu, O. M. Neamtu, L. G. Tataranu, A. M. Georgescu, V. Tudorica, C. Zaharia and A. Dricu (2014). "Plasma levels of glucose and insulin in patients with brain tumors." Curr Health Sci J **40**(1): 27–36.

Araiza-Olivera, D., Y. Feng, G. Semenova, T. Y. Prudnikova, J. Rhodes and J. Chernoff (2018). "Suppression of RAC1-driven malignant melanoma by group A PAK inhibitors." Oncogene **37**(7): 944-952.

Balch, C. M., J. E. Gershenwald, S. J. Soong, J. F. Thompson, M. B. Atkins, D. R. Byrd, A. C. Buzaid, A. J. Cochran, D. G. Coit, S. Ding, A. M. Eggermont, K. T. Flaherty, P. A. Gimotty, J. M. Kirkwood, K. M. McMasters, M. C. Mihm, Jr., D. L. Morton, M. I. Ross, A. J. Sober and V. K. Sondak (2009). "Final version of 2009 AJCC melanoma staging and classification." J Clin Oncol **27**(36): 6199-6206.

Berger, M. F., E. Hodis, T. P. Heffernan, Y. L. Deribe, M. S. Lawrence, A. Protopopov, E. Ivanova, I. R. Watson, E. Nickerson, P. Ghosh, H. Zhang, R. Zeid, X. Ren, K. Cibulskis, A. Y.

Sivachenko, N. Wagle, A. Sucker, C. Sougnez, R. Onofrio, L. Ambrogio, D. Auclair, T. Fennell, S. L. Carter, Y. Drier, P. Stojanov, M. A. Singer, D. Voet, R. Jing, G. Saksena, J. Barretina, A. H. Ramos, T. J. Pugh, N. Stransky, M. Parkin, W. Winckler, S. Mahan, K. Ardlie, J. Baldwin, J. Wargo, D. Schadendorf, M. Meyerson, S. B. Gabriel, T. R. Golub, S. N. Wagner, E. S. Lander, G. Getz, L. Chin and L. A. Garraway (2012). "Melanoma genome sequencing reveals frequent PREX2 mutations." Nature **485**(7399): 502-506.

Bid, H. K., R. D. Roberts, P. K. Manchanda and P. J. Houghton (2013). "RAC1: an emerging therapeutic option for targeting cancer angiogenesis and metastasis." Mol Cancer Ther **12**(10): 1925-34.

Boire, A., S. B. Coffelt, S. A. Quezada, M. G. Vander Heiden and A. T. Weeraratna (2019). "Tumour Dormancy and Reawakening: Opportunities and Challenges." Trends Cancer **5**(12): 762-765.

Boire, A., P. K. Brastianos, L. Garzia and M. Valiente (2020). "Brain metastasis." Nat Rev Cancer **20**(1): 4-11.

Bosco, E. E., J. C. Mulloy and Y. Zheng (2009). "Rac1 GTPase: a "Rac" of all trades." Cell Mol Life Sci **66**(3): 370-374.

Brandao, M., T. Simon, G. Critchley and G. Giamas (2019). "Astrocytes, the rising stars of the glioblastoma microenvironment." Glia **67**(5): 779-790.

Broman, K. K., L. A. Dossett, J. Sun, Z. Eroglu and J. S. Zager (2019). "Update on BRAF and MEK inhibition for treatment of melanoma in metastatic, unresectable, and adjuvant settings." Expert Opin Drug Saf **18**(5): 381-392.

Brown, P. D., M. S. Ahluwalia, O. H. Khan, A. L. Asher, J. S. Wefel and V. Gondi (2018). "Whole-Brain Radiotherapy for Brain Metastases: Evolution or Revolution?" J Clin Oncol **36**(5): 483-491.

Bucheit, A. D., G. Chen, A. Siroy, M. Tetzlaff, R. Broaddus, D. Milton, P. Fox, R. Bassett, P. Hwu, J. E. Gershenwald, A. J. Lazar and M. A. Davies (2014). "Complete loss of PTEN protein expression correlates with shorter time to brain metastasis and survival in stage IIIB/C melanoma patients with BRAFV600 mutations." Clin Cancer Res **20**(21): 5527-5536.

Cannon, A. C., C. Uribe-Alvarez and J. Chernoff (2020). "RAC1 as a Therapeutic Target in Malignant Melanoma." Trends Cancer **6**(6): 478-488.

Carswell R. (1838). "Illustrations of the elementary forms of disease." London: Longman, Orme, Brown, Greene and Longman

Cassidy, P. B., M. Honeggar, R. L. Poerschke, K. White, S. R. Florell, R. H. Andtbacka, J. Tross, M. Anderson, S. A. Leachman and P. J. Moos (2015). "The role of thioredoxin reductase 1 in melanoma metabolism and metastasis." Pigment Cell Melanoma Res **28**(6): 685-695.

Cen, D., R. I. Gonzalez, J. A. Buckmeier, R. S. Kahlon, N. B. Tohidian and F. L. Meyskens, Jr. (2002). "Disulfiram induces apoptosis in human melanoma cells: a redox-related process." Mol Cancer Ther **1**(3): 197-204.

Chang, F., C. A. Lemmon, D. Park and L. H. Romer (2007). "FAK potentiates Rac1 activation and localization to matrix adhesion sites: a role for betaPIX." Mol Biol Cell **18**(1): 253-264.

Chapman, P. B., A. Hauschild, C. Robert, J. B. Haanen, P. Ascierto, J. Larkin, R. Dummer, C. Garbe, A. Testori, M. Maio, D. Hogg, P. Lorigan, C. Lebbe, T. Jouary, D. Schadendorf, A. Ribas, S. J. O'Day, J. A. Sosman, J. M. Kirkwood, A. M. Eggermont, B. Dreno, K. Nolop, J. Li, B. Nelson, J. Hou, R. J. Lee, K. T. Flaherty and G. A. McArthur (2011). "Improved survival with vemurafenib in melanoma with BRAF V600E mutation." N Engl J Med **364**(26): 2507-2516.

Chauhan, B. K., N. Lou, Y. Zheng and R. A. Lang (2011). " Balanced Rac1 and RhoA activities regulate cell shape and drive invagination morphogenesis in epithelia." PNAS **108**(45): 18289-18294.

Chen, G. and M. A. Davies (2012). "Emerging insights into the molecular biology of brain metastases." Biochem Pharmacol **83**(3): 305-314.

Chen, G., N. Chakravarti, K. Aardalen, A.J. Lazar, M.T. Tetzlaff, B. Wubbenhorst, S. B. Kim, S. Kopetz, A. A. Ledoux, Y. N. Gopal, C. G. Pereira, W. Deng, J. S. Lee, K. L. Nathanson, K. D. Aldape, V. G. Prieto, D. Stuart and M. A. Davies (2014). "Molecular profiling of patient-matched brain and extracranial melanoma metastases implicates the PI3K pathway as a therapeutic target." Clin Cancer Res **20**(21): 5537-46.

Chen, Y. (2012). "Cell Adhesion Assay." Bio-101: e98.

Cheng, L., A. Lopez-Beltran, F. Massari, G. T. MacLennan and R. Montironi (2018). "Molecular testing for BRAF mutations to inform melanoma treatment decisions: a move toward precision medicine." Mod Pathol **31**(1): 24-38.

Chio, I. I. C. and D. A. Tuveson (2017). "ROS in Cancer: The Burning Question." Trends Mol Med **23**(5): 411-429.

Cho, J. H., J. P. Robinson, R. A. Arave, W. J. Burnett, D. A. Kircher, G. Chen, M. A. Davies, A. H. Grossmann, M. W. VanBrocklin, M. McMahon and S. L. Holmen (2015). "AKT1 Activation Promotes Development of Melanoma Metastases." Cell Rep **13**(5): 898-905.

Chung, E. Y., Y. Mai, U. A. Shah, Y. Wei, E. Ishida, K. Kataoka, X. Ren, K. Pradhan, B. Bartholdy, X. Wei, Y. Zou, J. Zhang, S. Ogawa, U. Steidl, X. Zang, A. Verma, M. Janakiram and B. H. Ye (2019). "PAK Kinase Inhibition Has Therapeutic Activity in Novel Preclinical Models of Adult T-Cell Leukemia/Lymphoma." Clin Cancer Res **25**(12): 3589-3601.

Cohen, J. V., N. Wang, V. A. Venur, M. J. Hadfield, D. P. Cahill, K. Oh and P. K. Brastianos (2020). "Neurologic complications of melanoma." Cancer **126**(3): 477-486.

Colombino, M., M. Capone, A. Lissia, A. Cossu, C. Rubino, V. De Giorgi, D. Massi, E. Fonsatti, S. Staibano, O. Nappi, E. Pagani, M. Casula, A. Manca, M. Sini, R. Franco, G. Botti, C. Caracò, N. Mozzillo, P. A. Ascierto and G. Palmieri (2012). "BRAF/NRAS mutation frequencies among primary tumors and metastases in patients with melanoma." J Clin Oncol **30**(20): 2522-2529.

Colón-Bolea, P., R. García-Gómez and B. Casar (2021). "RAC1 Activation as a Potential Therapeutic Option in Metastatic Cutaneous Melanoma." Biomolecules **11**(11): 1554.

Conrad, M., S. M. Lorenz and B. Proneth (2021). "Targeting Ferroptosis: New Hope for As-Yet-Incurable Diseases." Trends Mol Med **27**(2): 113-122.

Creighton, C. J. and S. Huang. (2015). "Reverse phase protein arrays in signaling pathways: a data integration perspective." Drug Des Devel Ther **9**: 3519–3527.

de Curtis, I. (2014). "Roles of Rac1 and Rac3 GTPases during the development of cortical and hippocampal GABAergic interneurons." Front Cell Neurosci **8**: 307.

Czarnecka, A. M., E. Bartnik, M. Fiedorowicz and P. Rutkowski (2020). "Targeted Therapy in Melanoma and Mechanisms of Resistance." Int J Mol Sci **21**(13).

D'Orazio, J. A., S. Jarrett, A. Marsch, J. Lagrew and L. Cleary (2013). "Melanoma — Epidemiology, Genetics and Risk Factors." Recent Advances in the Biology, Therapy and Management of Melanoma, Lester M. Davids, IntechOpen.

Damsky, W. E. and M. Bosenberg (2017). "Melanocytic nevi and melanoma: unraveling a complex relationship." Oncogene **36**(42): 5771-5792.

Dankort, D., D. P. Curley, R. A. Cartlidge, B. Nelson, A. N. Karnezis, W. E. Damsky, Jr., M. J. You, R. A. DePinho, M. McMahon and M. Bosenberg (2009). "Braf(V600E) cooperates with Pten loss to induce metastatic melanoma." Nat Genet **41**(5): 544-552.

Davies, H., G. R. Bignell, C. Cox, P. Stephens, S. Edkins, S. Clegg, J. Teague, H. Woffendin, M. J. Garnett, W. Bottomley, N. Davis, E. Dicks, R. Ewing, Y. Floyd, K. Gray, S. Hall, R. Hawes, J. Hughes, V. Kosmidou, A. Menzies, C. Mould, A. Parker, C. Stevens, S. Watt, S. Hooper, R. Wilson, H. Jayatilake, B. A. Gusterson, C. Cooper, J. Shipley, D. Hargrave, K. Pritchard-Jones, N. Maitland, G. Chenevix-Trench, G. J. Riggins, D. D. Bigner, G. Palmieri, A. Cossu, A. Flanagan, A. Nicholson, J. W. Ho, S. Y. Leung, S. T. Yuen, B. L. Weber, H. F. Seigler, T. L. Darrow, H. Paterson, R. Marais, C. J. Marshall, R. Wooster, M. R. Stratton and P. A. Futreal (2002). "Mutations of the BRAF gene in human cancer." Nature **417**(6892): 949-954.

Davies, M. A., P. Saiag, C. Robert, J. J. Grob, K. T. Flaherty, A. Arance, V. Chiarion-Sileni, L. Thomas, T. Lesimple, L. Mortier, S. J. Moschos, D. Hogg, I. Márquez-Rodas, M. Del Vecchio, C. Lebbé, N. Meyer, Y. Zhang, Y. Huang, B. Mookerjee and G. V. Long (2017). "Dabrafenib plus trametinib in patients with BRAF(V600)-mutant melanoma brain metastases (COMBI-MB): a multicentre, multicohort, open-label, phase 2 trial." Lancet Oncol **18**(7): 863-873.

Davies, M. A., K. Stemke-Hale, E. Lin, C. Tellez, W. Deng, Y. N. Gopal, S. E. Woodman, T. C. Calderone, Z. Ju, A. J. Lazar, V. G. Prieto, K. Aldape, G. B. Mills and J. E. Gershenwald (2009). "Integrated Molecular and Clinical Analysis of AKT Activation in Metastatic Melanoma." Clin Cancer Res **15**(24): 7538-7546.

Davies, M. A., K. Stemke-Hale, C. Tellez, T. L. Calderone, W. Deng, V. G. Prieto, A. J. Lazar, J. E. Gershenwald and G. B. Mills (2008). "A novel AKT3 mutation in melanoma tumours and cell lines." Br J Cancer **99**(8): 1265-1268.

Davis, E. J., D. B. Johnson, J. A. Sosman and S. Chandra (2018). "Melanoma: What do all the mutations mean?" Cancer **124**(17): 3490-3499.

Deshmukh, J., R. Pofahl and I. Haase (2017). "Epidermal Rac1 regulates the DNA damage response and protects from UV-light-induced keratinocyte apoptosis and skin carcinogenesis." Cell Death Dis **8**(3): e2664.

Diener, J. and L. Sommer (2021). "Reemergence of neural crest stem cell-like states in melanoma during disease progression and treatment." Stem Cells Transl Med **10**(4): 522-533.

Dimitriou, F., G.V. Long and A. M. Menzies (2021). "Novel adjuvant options for cutaneous melanoma." Ann Oncol **32**(7): 854-865.

Dixon, S. J. (2017). "Ferroptosis: bug or feature?" Immunol Rev **277**(1): 150-157.

Dixon, S. J., K. M. Lemberg, M. R. Lamprecht, R. Skouta, E. M. Zaitsev, C. E. Gleason, D. N. Patel, A. J. Bauer, A. M. Cantley, W. S. Yang, B. Morrison, 3rd and B. R. Stockwell (2012). "Ferroptosis: an iron-dependent form of nonapoptotic cell death." Cell **149**(5): 1060-1072.

Dolma, S., S. L. Lessnick, W. C. Hahn and B. R. Stockwell (2003). "Identification of genotype-selective antitumor agents using synthetic lethal chemical screening in engineered human tumor cells." Cancer Cell **3**(3): 285-296.

Dorard, C., C. Estrada, C. Barbotin, M. Larcher, A. Garancher, J. Leloup, F. Beermann, M. Baccarini, C. Pouponnot, L. Larue, A. Eychène and S. Druillennec (2017). "RAF proteins exert both specific and compensatory functions during tumour progression of NRAS-driven melanoma." Nat Commun **8**: 15262.

Dummer, R., A. Hauschild, M. Santinami, V. Atkinson, M. Mandalà, J. M. Kirkwood, V. Chiarion Sileni, J. Larkin, M. Nyakas, C. Dutriaux, A. Haydon, C. Robert, L. Mortier, J. Schachter, T. Lesimple, R. Plummer, K. Dasgupta, E. Gasal, M. Tan, G. V. Long and D. Schadendorf (2020). "Five-Year Analysis of Adjuvant Dabrafenib plus Trametinib in Stage III Melanoma." N Engl J Med **383**(12): 1139-1148.

Estrela, J. M., A. Ortega and E. Obrador (2006). "Glutathione in cancer biology and therapy." Crit Rev Clin Lab Sci **43**(2): 143-181.

Euromelanoma. https://www.euromelanoma.org/.

Fares, J., M. Y. Fares, H. H. Khachfe, H. A. Salhab and Y. Fares (2020). "Molecular principles of metastasis: a hallmark of cancer revisited." Signal Transduct Target Ther **5**(1): 28.

Fellner, C. (2012). "Ipilimumab (yervoy) prolongs survival in advanced melanoma: serious side effects and a hefty price tag may limit its use." PT **37**(9): 503–530.

Feng, H., B. Hu, K. W. Liu, Y. Li, X. Lu, T. Cheng, J. J. Yiin, S. Lu, S. Keezer, T. Fenton, F. B. Furnari, R. L. Hamilton, K. Vuori, J. N. Sarkaria, M. Nagane, R. Nishikawa, W. K. Cavenee and S. Y. Cheng (2011). "Activation of Rac1 by Src-dependent phosphorylation of Dock180(Y1811) mediates PDGFRα-stimulated glioma tumorigenesis in mice and humans." J Clin Invest **121**(12): 4670-4684.

Feng, H., K. Schorpp, J. Jin, C. E. Yozwiak, B. G. Hoffstrom, A. M. Decker, P. Rajbhandari, M. E. Stokes, H. G. Bender, J. M. Csuka, P. S. Upadhyayula, P. Canoll, K. Uchida, R. K. Soni, K. Hadian and B. R. Stockwell (2020). "Transferrin Receptor Is a Specific Ferroptosis Marker." Cell Rep **30**(10): 3411-3423.e3417.

Ferguson, J., M. Smith, I. Zudaire, C. Wellbrock and I. Arozarena (2017). "Glucose availability controls ATF4-mediated MITF suppression to drive melanoma cell growth." Oncotarget **8**(20): 32946-32959.

Fernández-Medarde, A. and E. Santos (2011). "Ras in cancer and developmental diseases." Genes Cancer **2**(3): 344-358.

Ferro, E., L. Goitre, S. F. Retta and L. Trabalzini (2012). "The Interplay between ROS and Ras GTPases: Physiological and Pathological Implications." J Signal Transduct **2012**: 365769.

Fischer, G. M., Y. N. Vashisht Gopal, J. L. McQuade, W. Peng, R. J. DeBerardinis and M. A. Davies (2018). "Metabolic strategies of melanoma cells: Mechanisms, interactions with the tumor microenvironment, and therapeutic implications." Pigment Cell Melanoma Res **31**(1): 11-30.

Forsea, A. M. (2020). "Melanoma Epidemiology and Early Detection in Europe: Diversity and Disparities." Dermatology Pract Concept **10**(3): e2020033.

Fruehauf, J. P. and F. L. Meyskens, Jr. (2007). "Reactive oxygen species: a breath of life or death?" Clin Cancer Res **13**(3): 789-794.

Gajewski, T. F., A. K. Salama, D. Niedzwiecki, J. Johnson, G. Linette, C. Bucher, M. A. Blaskovich, S. M. Sebti and F. Haluska (2012). "Phase II study of the farnesyltransferase inhibitor R115777 in advanced melanoma (CALGB 500104)." J Transl Med **10**: 246.

Galluzzi, L., I. Vitale, S. A. Aaronson, J. M. Abrams, D. Adam, P. Agostinis, E. S. Alnemri, L. Altucci, I. Amelio, D. W. Andrews, M. Annicchiarico-Petruzzelli, A. V. Antonov, E. Arama, E. H. Baehrecke, N. A. Barlev, N. G. Bazan, F. Bernassola, M. J. M. Bertrand, K. Bianchi, M. V. Blagosklonny, K. Blomgren, C. Borner, P. Boya, C. Brenner, M. Campanella, E. Candi, D. Carmona-Gutierrez, F. Cecconi, F. K. Chan, N. S. Chandel, E. H. Cheng, J. E. Chipuk, J. A. Cidlowski, A. Ciechanover, G. M. Cohen, M. Conrad, J. R. Cubillos-Ruiz, P. E. Czabotar, V. D'Angiolella, T. M. Dawson, V. L. Dawson, V. De Laurenzi, R. De Maria, K. M. Debatin, R. J. DeBerardinis, M. Deshmukh, N. Di Daniele, F. Di Virgilio, V. M. Dixit, S. J. Dixon, C. S. Duckett, B. D. Dynlacht, W. S. El-Deiry, J. W. Elrod, G. M. Fimia, S. Fulda, A. J. García-Sáez, A. D. Garg, C. Garrido, E. Gavathiotis, P. Golstein, E. Gottlieb, D. R. Green, L. A. Greene, H. Gronemeyer, A. Gross, G. Hajnoczky, J. M. Hardwick, I. S. Harris, M. O. Hengartner, C. Hetz, H. Ichijo, M. Jäättelä, B. Joseph, P. J. Jost, P. P. Juin, W. J. Kaiser, M. Karin, T. Kaufmann, O. Kepp, A. Kimchi, R. N. Kitsis, D. J. Klionsky, R. A. Knight, S. Kumar, S. W. Lee, J. J. Lemasters, B. Levine, A. Linkermann, S. A. Lipton, R. A. Lockshin, C. López-Otín, S. W. Lowe, T. Luedde, E. Lugli, M. MacFarlane, F. Madeo, M. Malewicz, W. Malorni, G. Manic, J. C. Marine, S. J. Martin, J. C. Martinou, J. P. Medema, P. Mehlen, P. Meier, S. Melino, E. A. Miao, J. D. Molkentin, U. M. Moll, C. Muñoz-Pinedo, S. Nagata, G. Nuñez, A. Oberst, M. Oren, M. Overholtzer, M. Pagano, T. Panaretakis, M. Pasparakis, J. M. Penninger, D. M. Pereira, S. Pervaiz, M. E. Peter, M. Piacentini, P. Pinton, J. H. M. Prehn, H. Puthalakath, G. A. Rabinovich, M. Rehm, R. Rizzuto, C. M. P. Rodrigues, D. C. Rubinsztein, T. Rudel, K. M. Ryan, E. Sayan, L. Scorrano, F. Shao, Y. Shi, J. Silke, H. U. Simon, A. Sistigu, B. R. Stockwell, A. Strasser, G. Szabadkai, S. W. G. Tait, D. Tang, N. Tavernarakis, A. Thorburn, Y. Tsujimoto, B. Turk, T. Vanden Berghe, P. Vandenabeele, M. G. Vander Heiden, A. Villunger, H. W. Virgin, K. H. Vousden, D. Vucic, E. F. Wagner, H. Walczak, D. Wallach, Y. Wang, J. A. Wells, W. Wood, J. Yuan, Z. Zakeri, B. Zhivotovsky, L. Zitvogel, G. Melino and G. Kroemer (2018). "Molecular mechanisms of cell death: recommendations of the Nomenclature Committee on Cell Death 2018." Cell Death Differ **25**(3): 486-541.

Gao, Y., J. B. Dickerson, F. Guo, J. Zheng and Y. Zheng (2004). "Rational design and characterization of a Rac GTPase-specific small molecule inhibitor." Proc Natl Acad Sci U S A **101**(20): 7618-7623.

Garnett, M. J. and R. Marais (2004). "Guilty as charged: B-RAF is a human oncogene." Cancer Cell **6**(4): 313-319.

Glitza Oliva, I., H. Tawbi and M. A. Davies (2017). "Melanoma Brain Metastases: Current Areas of Investigation and Future Directions." Cancer J **23**(1): 68-74.

Glitza, I. C., A. B. Heimberger, E. P. Sulman and M. A. Davies (2016). "Prognostic Factors for Survival in Melanoma Patients with Brain Metastases." In Brain Metastases from Primary Tumors: Epidemiology, Biology, and Therapy of Melanoma and Other Cancers (Vol. 3, pp. 267-297). Elsevier Inc.

Glitza Oliva, I. C., G. Schvartsman and H. Tawbi (2018). "Advances in the systemic treatment of melanoma brain metastases." Ann Oncol **29**(7): 1509-1520.

Global Coalition for Melanoma Patient Advocacy. https://www.globalmelanoma.org/.

Gordon, R. (2013). "Skin cancer: an overview of epidemiology and risk factors." Semin Oncol Nurs **29**(3): 160-169.

Grzywa, T. M., W. Paskal and P. K. Włodarski (2017). "Intratumor and Intertumor Heterogeneity in Melanoma." Translational oncology **10**(6): 956–975.

Han, Y., D. Liu and L. Li (2020). "PD-1/PD-L1 pathway: current researches in cancer." Am J Cancer Res **10**(3): 727-742.

Hanker, A. B., V. Kaklamani and C. L. Arteaga (2019). "Challenges for the Clinical Development of PI3K Inhibitors: Strategies to Improve Their Impact in Solid Tumors." Cancer Discov **9**(4): 482-491.

Hassannia, B., P. Vandenabeele and T. Vanden Berghe (2019). "Targeting Ferroptosis to Iron Out Cancer." Cancer Cell **35**(6): 830-849.

Haueis, S. A., P. Kränzlin, J. Mangana, P. F. Cheng, M. Urosevic-Maiwald, R. P. Braun, M. P. Levesque, R. Dummer and S. M. Goldinger (2017). "Does the distribution pattern of brain metastases during BRAF inhibitor therapy reflect phenotype switching?" Melanoma Res **27**(3): 231-237.

Hodis, E., I. R. Watson, G. V. Kryukov, S. T. Arold, M. Imielinski, J. P. Theurillat, E. Nickerson, D. Auclair, L. Li, C. Place, D. Dicara, A. H. Ramos, M. S. Lawrence, K. Cibulskis, A. Sivachenko, D. Voet, G. Saksena, N. Stransky, R. C. Onofrio, W. Winckler, K. Ardlie, N. Wagle, J. Wargo, K. Chong, D. L. Morton, K. Stemke-Hale, G. Chen, M. Noble, M. Meyerson, J. E. Ladbury, M. A. Davies, J. E. Gershenwald, S. N. Wagner, D. S. Hoon, D. Schadendorf, E. S. Lander, S. B. Gabriel, G. Getz, L. A. Garraway and L. Chin (2012). "A landscape of driver mutations in melanoma." Cell **150**(2): 251-263.

Hordijk, P. L. (2006). "Regulation of NADPH oxidases: the role of Rac proteins." Circ Res **98**(4): 453-462.

Hoxhaj, G. and B. D. Manning (2020). "The PI3K-AKT network at the interface of oncogenic signalling and cancer metabolism." Nat Rev Cancer **20**(2): 74-88.

Hutchenreuther, J., K. Vincent, C. Norley, M. Racanelli, S. B. Gruber, T. M. Johnson, D. R. Fullen, L. Raskin, B. Perbal, D. W. Holdsworth, L. M. Postovit and A. Leask (2018).

"Activation of cancer-associated fibroblasts is required for tumor neovascularization in a murine model of melanoma." Matrix Biol **74**:52-61.

In, G. K., K. A. Poorman, M. Saul, S. O'Day, J. M. Farma, S. Daveluy, A. J. Olszanski, M. S. Gordon, J. S. Thomas, B. L. Eisenberg, L. E. Flaherty, G. T. Gibney, M. B. Atkins and A. M. Vanderwalde (2019). "Molecular profiling of melanoma brain metastases (MBM) compared to primary cutaneous melanoma (CM)." J Clin Oncol **37**:15_suppl, 9565-9565

Izraely, S., O. Sagi-Assif, A. Klein, T. Meshel, G. Tsarfaty, M. Pasmanik-Chor, C. Nahmias, P. O. Couraud, E. Ateh, J. L. Bryant, D. S. Hoon and I. P. Witz (2011). "The metastatic microenvironment: brain-residing melanoma metastasis and dormant micrometastasis." Int J Cancer **131**(5): 1071-82.

Jebali, A. and N. Dumaz (2018). "The role of RICTOR downstream of receptor tyrosine kinase in cancers." Mol Cancer **17**(1): 39.

Jobe, N. P., D. Rösel, B. Dvořánková, O. Kodet, L. Lacina, R. Mateu, K. Smetana and J. Brábek (2016). "Simultaneous blocking of IL-6 and IL-8 is sufficient to fully inhibit CAF-induced human melanoma cell invasiveness." Histochem Cell Biol **146**(2): 205-217.

Kakadia, S., N. Yarlagadda, R. Awad, M. Kundranda, J. Niu, B. Naraev, L. Mina, T. Dragovich, M. Gimbel and F. Mahmoud (2018). "Mechanisms of resistance to BRAF and MEK inhibitors and clinical update of US Food and Drug Administration-approved targeted therapy in advanced melanoma." Onco Targets Ther **11**: 7095–7107.

Kaneto, N., S. Yokoyama, Y. Hayakawa, S. Kato, H. Sakurai and I. Saiki (2014). "RAC1 inhibition as a therapeutic target for gefitinib-resistant non-small-cell lung cancer." Cancer Sci **105**(7): 788-794.

Kerkar, S. P. and N. P. Restifo (2012). "Cellular constituents of immune escape within the tumor microenvironment." Cancer Res **72**(13): 3125-3130.

Khamis, Z. I., N. Al-Akkary, T. Hua, S. A. Draughon, Y. Li and Q. X. A. Sang (2021). "Clinical investigations of immunotherapy for human primary brain tumors." Neuroimmunol Neuroinflammation **8**: 154-73.

Kienast, Y., L. von Baumgarten, M. Fuhrmann, W. E. Klinkert, R. Goldbrunner, J. Herms and F. Winkler (2010). "Real-time imaging reveals the single steps of brain metastasis formation." Nat Med **16**(1): 116-22.

Kim, L. C., R. S. Cook and J. Chen (2017). "mTORC1 and mTORC2 in cancer and the tumor microenvironment." Oncogene **36**(16): 2191-2201.

Kim, S. J., J. S. Kim, E. S. Park, J. S. Lee, Q. Lin, R. R. Langley, M. Maya, J. He, S. W. Kim, Z. Weihua, K. Balasubramanian, D. Fan, G. B. Mills, M. C. Hung and I. J. Fidler (2011). "Astrocytes upregulate survival genes in tumor cells and induce protection from chemotherapy." Neoplasia **13**(3): 286-298.

Kircher, D. A., K. A. Trombetti, M. R. Silvis, G. L. Parkman, G. M. Fischer, S. N. Angel, C. M. Stehn, S. C. Strain, A. H. Grossmann, K. L. Duffy, K. M. Boucher, M. McMahon, M. A. Davies, M. C. Mendoza, M. W. VanBrocklin and S. L. Holmen (2019). "AKT1(E17K) Activates Focal Adhesion Kinase and Promotes Melanoma Brain Metastasis." Mol Cancer Res **17**(9): 1787-1800.

Klein, A., O. Sagi-Assif, S. Izraely, T. Meshel, M. Pasmanik-Chor, C. Nahmias, P. O. Couraud, N. Erez, D. S. Hoon and I. P. Witz (2012). "The metastatic microenvironment: Brain-derived soluble factors alter the malignant phenotype of cutaneous and brain-metastasizing melanoma cells." Int J Cancer **131**(11): 2509-18.

Knisely, J. P., J. B. Yu, J. Flanigan, M. Sznol, H. M. Kluger and V. L. Chiang (2012). "Radiosurgery for melanoma brain metastases in the ipilimumab era and the possibility of longer survival." J Neurosurg **117**(2): 227-233.

Ko, J. S. (2017). "The Immunology of Melanoma." Clin Lab Med **37**(3): 449-471.

Kodet, O., J. Kučera, K. Strnadová, B. Dvořánková, J. Štork, L. Lacina and K. Smetana, Jr. (2020). "Cutaneous melanoma dissemination is dependent on the malignant cell properties and factors of intercellular crosstalk in the cancer microenvironment (Review)." Int J Oncol **57**(3): 619-630.

Kong, Y., L. Si, Y. Li, X. Wu, X. Xu, J. Dai, H. Tang, M. Ma, Z. Chi, X. Sheng, C. Cui and J. Guo (2016). "Analysis of mTOR Gene Aberrations in Melanoma Patients and Evaluation of Their Sensitivity to PI3K-AKT-mTOR Pathway Inhibitors." Clin Cancer Res **22**(4): 1018-1027.

Krauthammer, M., Y. Kong, B. H. Ha, P. Evans, A. Bacchiocchi, J. P. McCusker, E. Cheng, M. J. Davis, G. Goh, M. Choi, S. Ariyan, D. Narayan, K. Dutton-Regester, A. Capatana, E. C. Holman, M. Bosenberg, M. Sznol, H. M. Kluger, D. E. Brash, D. F. Stern, M. A. Materin, R. S. Lo, S. Mane, S. Ma, K. K. Kidd, N. K. Hayward, R. P. Lifton, J. Schlessinger, T. J. Boggon and R. Halaban (2012). "Exome sequencing identifies recurrent somatic RAC1 mutations in melanoma." Nat Genet **44**(9): 1006-1014.

Kwong, L. N. and M. A. Davies (2013). "Navigating the therapeutic complexity of PI3K pathway inhibition in melanoma." Clin Cancer Res **19**(19): 5310-5319.

Leinhos, L., J. Peters, S. Krull, L. Helbig, M. Vogler, M. Levay, G. J. van Belle, A. J. Ridley, S. Lutz, D. M. Katschinski and A. Zieseniss (2019). "Hypoxia suppresses myofibroblast differentiation by changing RhoA activity." J Cell Sci **132**(5).

Leonardi, G. C., L. Falzone, R. Salemi, A. Zanghì, D. A. Spandidos, J. A. McCubrey, S. Candido and M. Libra (2018). "Cutaneous melanoma: From pathogenesis to therapy (Review)." Int J Oncol **52**(4): 1071-1080.

Li, J., F. Cao, H. L. Yin, Z. J. Huang, Z. T. Lin, N. Mao, B. Sun and G. Wang (2020). "Ferroptosis: past, present and future." Cell Death Dis **11**(2): 88.

Liang, J., L. Oyang, S. Rao, Y. Han, X. Luo, P. Yi, J. Lin, L. Xia, J. Hu, S. Tan, L. Tang, Q. Pan, Y. Tang, Y. Zhou and Q. Liao (2021). "Rac1, A Potential Target for Tumor Therapy." Front Oncol **11**:674426.

Licarete, E., V. F. Rauca, L. Luput, D. Drotar, I. Stejerean, L. Patras, B. Dume, V. A. Toma, A. Porfire, C. Gherman, A. Sesarman and M. Banciu (2020). "Overcoming Intrinsic Doxorubicin Resistance in Melanoma by Anti-Angiogenic and Anti-Metastatic Effects of Liposomal Prednisolone Phosphate on Tumor Microenvironment." Int J Mol Sci **21**(8).

Lionarons, D. A., D. C. Hancock, S. Rana, P. East, C. Moore, M. M. Murillo, J. Carvalho, B. Spencer-Dene, E. Herbert, G. Stamp, D. Damry, D. P. Calado, I. Rosewell, R. Fritsch, R. R. Neubig, M. Molina-Arcas and J. Downward (2019). "RAC1(P29S) Induces a Mesenchymal

Phenotypic Switch via Serum Response Factor to Promote Melanoma Development and Therapy Resistance." Cancer Cell **36**(1): 68-83.e69.

Liu-Smith, F., R. Dellinger and F. L. Meyskens, Jr. (2014). "Updates of reactive oxygen species in melanoma etiology and progression." Arch Biochem Biophys **563**: 51-55.

Long, G. V., J. J. Grob, P. Nathan, A. Ribas, C. Robert, D. Schadendorf, S. R. Lane, C. Mak, P. Legenne, K. T. Flaherty and M. A. Davies (2016). "Factors predictive of response, disease progression, and overall survival after dabrafenib and trametinib combination treatment: a pooled analysis of individual patient data from randomised trials." Lancet Oncol **17**(12): 1743-1754.

Long, G. V., U. Trefzer, M. A. Davies, R. F. Kefford, P. A. Ascierto, P. B. Chapman, I. Puzanov, A. Hauschild, C. Robert, A. Algazi, L. Mortier, H. Tawbi, T. Wilhelm, L. Zimmer, J. Switzky, S. Swann, A. M. Martin, M. Guckert, V. Goodman, M. Streit, J. M. Kirkwood and D. Schadendorf (2012). "Dabrafenib in patients with Val600Glu or Val600Lys BRAF-mutant melanoma metastatic to the brain (BREAK-MB): a multicentre, open-label, phase 2 trial" Lancet Oncol **13**(11): 1087-95.

Lu, H., S. Liu, G. Zhang, B. Wu, Y. Zhu, D. T. Frederick, Y. Hu, W. Zhong, S. Randell, N. Sadek, W. Zhang, G. Chen, C. Cheng, J. Zeng, L. W. Wu, J. Zhang, X. Liu, W. Xu, C. Krepler, K. Sproesser, M. Xiao, B. Miao, J. Liu, C. D. Song, J. Y. Liu, G. C. Karakousis, L. M. Schuchter, Y. Lu, G. Mills, Y. Cong, J. Chernoff, J. Guo, G. M. Boland, R. J. Sullivan, Z. Wei, J. Field, R. K. Amaravadi, K. T. Flaherty, M. Herlyn, X. Xu and W. Guo (2017). "PAK signalling drives acquired drug resistance to MAPK inhibitors in BRAF-mutant melanomas." Nature **550**(7674): 133–136.

Mahmood, T. and P. C. Yang (2012). "Western blot: technique, theory, and trouble shooting." N Am J Med Sci **4**(9): 429-434.

Machesky, L. M. and O. J. Sansom (2012). "Rac1 in the driver's seat for melanoma." Pigment Cell Melanoma Res **25**(6): 762-4.

Maldonado, M. D. M., J. I. Medina, L. Velazquez and S. Dharmawardhane (2020). "Targeting Rac and Cdc42 GEFs in Metastatic Cancer." Front Cell Dev Biol **8**:201.

Martin, K., A. Reimann, R.D. Fritz, H. Ryu, N. L. Jeon and O. Pertz (2016). "Spatio-temporal co-ordination of RhoA, Rac1 and Cdc42 activation during prototypical edge protrusion and retraction dynamics." Sci Rep **6**(1): 21901.

Matallanas, D., M. Birtwistle, D. Romano, A. Zebisch, J. Rauch, A. von Kriegsheim and W. Kolch (2011). "Raf family kinases: old dogs have learned new tricks." Genes Cancer **2**(3): 232-260.

McMaster Pathophysiology Review. http://www.pathophys.org/melanoma/.

Meierjohann, S (2017). "Crosstalk signaling in targeted melanoma therapy." Cancer Metastasis Rev **36**(1): 23-33

Mergenthaler P, U. Lindauer, G.A. Dienel and A. Meisel (2013). "Sugar for the brain: the role of glucose in physiological and pathological brain function." Trends Neurosci **36**(10): 587-597.

McArthur, G. A., M. Maio, A. Arance, P. Nathan, C. Blank, M. F. Avril, C. Garbe, A. Hauschild, D. Schadendorf, O. Hamid, M. Fluck, M. Thebeau, J. Schachter, R. Kefford, M.

Chamberlain, M. Makrutzki, S. Robson, R. Gonzalez and K. Margolin (2017). "Vemurafenib in metastatic melanoma patients with brain metastases: an open-label, single-arm, phase 2, multicentre study." Ann Oncol **28**(3): 634-641.

MD Anderson Center RPPA core facility. https://www.mdanderson.org/research/research-resources/core-facilities/functional-proteomics-rppa-core.html.

Melanoma Research Alliance. https://www.curemelanoma.org/.

Meyskens, F. L., Jr., S. E. McNulty, J. A. Buckmeier, N. B. Tohidian, T. J. Spillane, R. S. Kahlon and R. I. Gonzalez (2001). "Aberrant redox regulation in human metastatic melanoma cells compared to normal melanocytes." Free Radic Biol Med **31**(6): 799-808.

Miyano, K. and H. Sumimoto (2012). "Assessment of the role for Rho family GTPases in NADPH oxidase activation." Methods Mol Biol **827**: 195-212.

Montalvo-Ortiz, B. L., L. Castillo-Pichardo, E. Hernández, T. Humphries-Bickley, A. De la Mota-Peynado, L. A. Cubano, C. P. Vlaar and S. Dharmawardhane (2012). "Characterization of EHop-016, novel small molecule inhibitor of Rac GTPase." J Biol Chem **287**(16): 13228-13238.

Moore, C. B., E. H. Guthrie, M. T. Huang and D. J. Taxman. (2010). "Short hairpin RNA (shRNA): design, delivery, and assessment of gene knockdown." Methods Mol Biol **629**: 141–158.

Murphy, M. P. (2009). "How mitochondria produce reactive oxygen species." Biochem J **417**(1): 1-13.

Neman, J., J. Termini, S. Wilczynski, N. Vaidehi, C. Choy, C. M. Kowolik, H. Li, A. C. Hambrecht, E. Roberts and R. Jandial (2014). "Human breast cancer metastases to the brain display GABAergic properties in the neural niche." Proc Natl Acad Sci U S A **111**(3): 984-989.

Newell, F., I. Pires da Silva, P. A. Johansson, A. M. Menzies, J. S. Wilmott, V. Addala, M. S. Carlino, H. Rizos, K. Nones, J. J. Edwards, V. Lakis, S. H. Kazakoff, P. Mukhopadhyay, P. M. Ferguson, C. Leonard, L. T. Koufariotis, S. Wood, C. U. Blank, J. F. Thompson, A. J. Spillane, R. P. M. Saw, K. F. Shannon, J. V. Pearson, G. J. Mann, N. K. Hayward, R. A. Scolyer, N. Waddell and G. V. Long (2022). "Multiomic profiling of checkpoint inhibitor-treated melanoma: Identifying predictors of response and resistance, and markers of biological discordance." Cancer Cell **40**(1): 88-102.e7

Niessner, H., A. Forschner, B. Klumpp, J. B. Honegger, M. Witte, A. Bornemann, R. Dummer, A. Adam, J. Bauer, G. Tabatabai, K. Flaherty, T. Sinnberg, D. Beck, U. Leiter, C. Mauch, A. Roesch, B. Weide, T. Eigentler, D. Schadendorf, C. Garbe, D. Kulms, L. Quintanilla-Martinez and F. Meier (2013). "Targeting hyperactivation of the AKT survival pathway to overcome therapy resistance of melanoma brain metastases." Cancer Med **2**(1): 76-85.

Noguchi, K., T. A. Dincman, A. C. Dalton, B. V. Howley, B. J. McCall, B. K. Mohanty and P. H. Howe (2018). "Interleukin-like EMT inducer (ILEI) promotes melanoma invasiveness and is transcriptionally up-regulated by upstream stimulatory factor-1 (USF-1)." J Biol Chem **293**(29): 11401-11414.

Norris, W. (1820). "Case of Fungoid Disease." Edinb Med Surg J **16**(65): 562-565.

Qiu, R. G., J. Chen, D. Kirn, F. McCormick and M. Symons (1995). "An essential role for Rac in Ras transformation." Nature **374**(6521): 457-459.

Onesto, C., A. Shutes, V. Picard, F. Schweighoffer and C. J. Der (2008). "Characterization of EHT 1864, a novel small molecule inhibitor of Rac family small GTPases." Methods Enzymol **439**: 111-129.

Ong, C. C., A. M. Jubb, D. Jakubiak, W. Zhou, J. Rudolph, P. M. Haverty, M. Kowanetz, Y. Yan, J. Tremayne, R. Lisle, A. L. Harris, L. S. Friedman, M. Belvin, M. R. Middleton, E. M. Blackwood, H. Koeppen and K. P. Hoeflich (2013). "P21-activated kinase 1 (PAK1) as a therapeutic target in BRAF wild-type melanoma." J Natl Cancer Inst **105**(9): 606-607.

Opazo, F., A. Punge, J. Bückers, P. Hoopmann, L. Kastrup, S. W. Hell and S. O. Rizzoli (2010). "Limited intermixing of synaptic vesicle components upon vesicle recycling." Traffic **11**(6): 800-812.

Ossowski, L., J. A. Aguirre-Ghiso (2010). "Dormancy of metastatic melanoma." Pigment Cell Melanoma Res **23**(1): 41-56.

Quail, D. F. and J. A. Joyce (2017). "The Microenvironmental Landscape of Brain Tumors." Cancer Cell **31**(3): 326-341.

Paget, J. (1853). "Lectures on Surgical Pathology." London: Longman, Brown, Green and Longman; p. 639.

Passarelli, A., F. Mannavola, L. S. Stucci, M. Tucci and F. Silvestris (2017). "Immune system and melanoma biology: a balance between immunosurveillance and immune escape." Oncotarget **8**(62): 106132–106142.

Piskounova, E., M. Agathocleous, M. M. Murphy, Z. Hu, S. E. Huddlestun, Z. Zhao, A. M. Leitch, T. M. Johnson, R. J. DeBerardinis and S. J. Morrison (2015). "Oxidative stress inhibits distant metastasis by human melanoma cells." Nature **527**(7577): 186-191.

Pópulo, H., J. M. Lopes and P. Soares (2012). "The mTOR signalling pathway in human cancer." Int J Mol Sci **13**(2): 1886-1918.

Porta, C., C. Paglino and A. Mosca (2014). "Targeting PI3K/Akt/mTOR Signaling in Cancer." Front Oncol **4**: 64.

Postow, M. A., M. K. Callahan, C. A. Barker, Y. Yamada, J. Yuan, S. Kitano, Z. Mu, T. Rasalan, M. Adamow, E. Ritter, C. Sedrak, A. A. Jungbluth, R. Chua, A. S. Yang, R. A. Roman, S. Rosner, B. Benson, J. P. Allison, A. M. Lesokhin, S. Gnjatic and J. D. Wolchok (2012). "Immunologic correlates of the abscopal effect in a patient with melanoma." N Engl J Med **366**(10): 925-931.

Qin, J. Z., H. Xin and B. J. Nickoloff (2010). "Targeting glutamine metabolism sensitizes melanoma cells to TRAIL-induced death." Biochem Biophys Res Commun **398**(1): 146-52.

Rajendran, L., J. Bali, M. M. Barr, F. A. Court, E. M. Krämer-Albers, F. Picou, G. Raposo, K. E. van der Vos, G. van Niel, J. Wang and X. O. Breakefield (2014). "Emerging roles of extracellular vesicles in the nervous system." J Neurosci **34**(46): 15482-15489.

Randic, T., I. Kozar, C. Margue, J. Utikal and S. Kreis (2021). "NRAS mutant melanoma: Towards better therapies." Cancer Treat Rev **99**: 102238.

Rastrelli, M., S. Tropea, C. R. Rossi and M. Alaibac (2014). "Melanoma: epidemiology, risk factors, pathogenesis, diagnosis and classification." In Vivo **28**(6): 1005-1011.

Raz, L., Q. G. Zhang, C. F. Zhou, D. Han, P. Gulati, L. C. Yang, F. Yang, R. M. Wang and D. W. Brann (2010). "Role of Rac1 GTPase in NADPH oxidase activation and cognitive impairment following cerebral ischemia in the rat." PLoS One **5**(9): e12606.

Rebecca, V. W., R. Somasundaram and M. Herlyn (2020). "Pre-clinical modeling of cutaneous melanoma." Nat Commun **11**(1): 2858.

Rebecca, V. W., V. K. Sondak and K. S. Smalley (2012). "A brief history of melanoma: from mummies to mutations." Melanoma Res **22**(2): 114-122.

Redmer, T. (2018). "Deciphering mechanisms of brain metastasis in melanoma - the gist of the matter." Mol Cancer **17**(1): 106.

Rinaldi, M., M. Caffo, L. Minutoli, H. Marini, R. V. Abbritti, F. Squadrito, V. Trichilo, A. Valenti, V. Barresi, D. Altavilla, M. Passalacqua and G. Caruso (2016). "ROS and Brain Gliomas: An Overview of Potential and Innovative Therapeutic Strategies." Int J Mol Sci **17**(6): 984.

Roesch, A., M. Fukunaga-Kalabis, E. C. Schmidt, S. E. Zabierowski, P. A. Brafford, A. Vultur, D. Basu, P. Gimotty, T. Vogt and M. Herlyn (2010). "A temporarily distinct subpopulation of slow-cycling melanoma cells is required for continuous tumor growth." Cell **141**(4): 583-594.

Roesch, A., A. Vultur, I. Bogeski, H. Wang, K. M. Zimmermann, D. Speicher, C. Körbel, M. W. Laschke, P. A. Gimotty, S. E. Philipp, E. Krause, S. Pätzold, J. Villanueva, C. Krepler, M. Fukunaga-Kalabis, M. Hoth, B. C. Bastian, T. Vogt and M. Herlyn (2013). "Overcoming intrinsic multidrug resistance in melanoma by blocking the mitochondrial respiratory chain of slow-cycling JARID1B(high) cells." Cancer Cell **23**(6): 811-825.

Ross, M. I. and J. E. Gershenwald (2011). "Evidence-based treatment of early-stage melanoma." J Surg Oncol **104**(4): 341-353.

Rowshanravan, B., N. Halliday and D. M. Sansom (2018). "CTLA-4: a moving target in immunotherapy." Blood **131**(1): 58-67.

Ryan, M. B., A. J. Finn, K. H. Pedone, N. E. Thomas, C. J. Der and A. D. Cox (2016). "ERK/MAPK Signaling Drives Overexpression of the Rac-GEF, PREX1, in BRAF- and NRAS-Mutant Melanoma." Mol Cancer Res **14**(10): 1009-1018.

Saci, A., L. C. Cantley and C. L. Carpenter (2011). "Rac1 regulates the activity of mTORC1 and mTORC2 and controls cellular size." Mol Cell **42**(1): 50-61.

Salvati, L., M. Mandalà and D. Massi (2020). "Melanoma brain metastases: review of histopathological features and immune-molecular aspects." Melanoma manag **7**(2): MMT44.

Sample, A., and Y. Y. He (2018). "Mechanisms and prevention of UV-induced melanoma." Photodermatol Photoimmunol Photomed, **34**(1): 13–24.

Satoh, T. and N. Takenaka (2019). "A critical role for the small GTPase Rac1 in insulin signaling that regulates glucose uptake in skeletal muscle." Res Chem Intermed **45**: 5389–5397.

Sayin, V. I., M. X. Ibrahim, E. Larsson, J. A. Nilsson, P. Lindahl and M. O. Bergo (2014). "Antioxidants accelerate lung cancer progression in mice." Sci Transl Med **6**(221): 221ra215.

Schadendorf (2012). "Dabrafenib in patients with Val600Glu or Val600Lys BRAF-mutant melanoma metastatic to the brain (BREAK-MB): a multicentre, open-label, phase 2 trial." Lancet Oncol **13**(11): 1087-1095.

Scott, M. S., S. J. Calafell, D. Y. Thomas and M. T. Hallett (2005). "Refining protein subcellular localization." PLoS Comput Biol **1**(6): e66.

Semenova, G. and J. Chernoff (2017). "Targeting PAK1." Biochem Soc Trans **45**(1): 79–88.

Sensi, M., G. Nicolini, C. Petti, I. Bersani, F. Lozupone, A. Molla, C. Vegetti, D. Nonaka, R. Mortarini, G. Parmiani, S. Fais and A. Anichini (2006). "Mutually exclusive NRASQ61R and BRAFV600E mutations at the single-cell level in the same human melanoma." Oncogene **25**(24): 3357-3364.

Servier Medical Art. https://smart.servier.com/.

Shain, A. H., N. M. Joseph, R. Yu, J. Benhamida, S. Liu, T. Prow, B. Ruben, J. North, L. Pincus, I. Yeh, R. Judson and B. C. Bastian (2018). "Genomic and Transcriptomic Analysis Reveals Incremental Disruption of Key Signaling Pathways during Melanoma Evolution." Cancer Cell **34**(1): 45-55.e44.

Shannan, B., Q. Chen, A. Watters, M. Perego, C. Krepler, R. Thombre, L. Li, G. Rajan, S. Peterson, P. A. Gimotty, M. Wilson, K. L. Nathanson, T. C. Gangadhar, L. M. Schuchter, A. T. Weeraratna, M. Herlyn and A. Vultur (2016). "Enhancing the evaluation of PI3K inhibitors through 3D melanoma models." Pigment Cell Melanoma Res **29**(3): 317-328.

Sharpe, A. H. and K. E. Pauken (2018). "The diverse functions of the PD1 inhibitory pathway." Nat Rev Immunol **18**(3): 153-167.

Shi, Y., S. R. Bollam, S. M. White, S. Z. Laughlin, G. T. Graham, M. Wadhwa, H. Chen, C. Nguyen, J. Vitte, M. Giovannini, J. Toretsky and C. Yi (2016). "Rac1-Mediated DNA Damage and Inflammation Promote Nf2 Tumorigenesis but Also Limit Cell-Cycle Progression." Dev Cell **39(**4): 452-465.

Sies, H., C. Berndt and D. P. Jones (2017). "Oxidative Stress." Annu Rev Biochem **86**: 715-748.

Singer, E, J. Judkins, N. Salomonis, L. Matlaf, P. Soteropoulos, S. McAllister and L. Soroceanu (2015). "Reactive oxygen species-mediated therapeutic response and resistance in glioblastoma." Cell Death Dis **6**(1): e1601.

Smalley, K. S. (2010). "Understanding melanoma signaling networks as the basis for molecular targeted therapy." J Invest Dermatol **130**(1): 28-37.

Smalley, K. S., M. Lioni, K. Noma, N. K. Haass and M. Herlyn (2008). "In vitro three-dimensional tumor microenvironment models for anticancer drug discovery." Expert Opin Drug Discov **3**(1): 1-10.

Stafford, W. C., X. Peng, M. H. Olofsson, X. Zhang, D. K. Luci, L. Lu, Q. Cheng, L. Trésaugues, T. S. Dexheimer, N. P. Coussens, M. Augsten, H. M. Ahlzén, O. Orwar, A. Östman, S. Stone-Elander, D. J. Maloney, A. Jadhav, A. Simeonov, A. Linder and E. S. J. Arnér

(2018). "Irreversible inhibition of cytosolic thioredoxin reductase 1 as a mechanistic basis for anticancer therapy." Sci Transl Med **10**(428): eaaf7444.

Stahl, J. M., M. Cheung, A. Sharma, N. R. Trivedi, S. Shanmugam and G. P. Robertson (2003). "Loss of PTEN promotes tumor development in malignant melanoma." Cancer Res **63**(11): 2881-2890.

Steeg, P. S., K. A. Camphausen and Q. R. Smith (2011). "Brain metastases as preventive and therapeutic targets." Nat Rev Cancer **11**(5): 352-363.

Stockwell, B. R., J. P. Friedmann Angeli, H. Bayir, A. I. Bush, M. Conrad, S. J. Dixon, S. Fulda, S. Gascón, S. K. Hatzios, V. E. Kagan, K. Noel, X. Jiang, A. Linkermann, M. E. Murphy, M. Overholtzer, A. Oyagi, G. C. Pagnussat, J. Park, Q. Ran, C. S. Rosenfeld, K. Salnikow, D. Tang, F. M. Torti, S. V. Torti, S. Toyokuni, K. A. Woerpel and D. D. Zhang (2017). "Ferroptosis: A Regulated Cell Death Nexus Linking Metabolism, Redox Biology, and Disease." Cell **171**(2): 273-285.

Stockwell, B. R., X. Jiang and W. Gu (2020). "Emerging Mechanisms and Disease Relevance of Ferroptosis." Trends Cell Biol **30**(6): 478-490.

Straus, D. S. (1981). "Effects of insulin on cellular growth and proliferation." Life Sci **29**(21): 2131-9.

Suh, J. H., R. Kotecha, S. T. Chao, M. S. Ahluwalia, A. Sahgal and E. L. Chang (2020). "Current approaches to the management of brain metastases." Nat Rev Clin Oncol **17**(5): 279-299.

Sunshine, J. C., P. L. Nguyen, G. J. Kaunitz, T. R. Cottrell, S. Berry, J. Esandrio, H. Xu, A. Ogurtsova, K. B. Bleich, T. C. Cornish, E. J. Lipson, R. A. Anders and J. M. (2017). "PD-L1 Expression in Melanoma: A Quantitative Immunohistochemical Antibody Comparison." Clin Cancer Res **23**(16): 4938-4944.

Superscript™ IV Reverse Transcriptase Kit. http://tools.thermofisher.com/content/sfs/manuals

/SSIV_ Reverse_Transcriptase_UG.pdf.

Talty, R. and M. Bosenberg (2021). "The role of ferroptosis in melanoma." Pigment Cell Melanoma Res Epub ahead of print.

Tawbi, H. A., C. Boutros, D. Kok, C. Robert and G. McArthur (2018). "New Era in the Management of Melanoma Brain Metastases." Am Soc Clin Oncol Educ Book **38**: 741-750.

The Skin Cancer Foundation. https://www.skincancer.org/

Tibes, R., Y. Qiu, Y. Lu, B. Hennessy, M. Andreeff, G. B. Mills and S. M. Kornblau (2006). "Reverse phase protein array: validation of a novel proteomic technology and utility for analysis of primary leukemia specimens and hematopoietic stem cells." Mol Cancer Ther **5**(10): 2512-2521.

Tsao, H., X. Zhang, K. Fowlkes and F. G. Haluska (2000). "Relative reciprocity of NRAS and PTEN/MMAC1 alterations in cutaneous melanoma cell lines." Cancer Res **60**(7): 1800-1804.

Tsoi, J., L. Robert, K. Paraiso, C. Galvan, K. M. Sheu, J. Lay, D. J. L. Wong, M. Atefi, R. Shirazi, X. Wang, D. Braas, C. S. Grasso, N. Palaskas, A. Ribas and T. G. Graeber (2018).

"Multi-stage Differentiation Defines Melanoma Subtypes with Differential Vulnerability to Drug-Induced Iron-Dependent Oxidative Stress." Cancer Cell **33**(5): 890-904.e895.

Tucci, M., A. Passarelli, F. Mannavola, C. Felici, L. S. Stucci, M. Cives and F. Silvestris (2019). "Immune System Evasion as Hallmark of Melanoma Progression: The Role of Dendritic Cells." Front Oncol **9**: 1148.

Ueda, S., S. Kitazawa, K. Ishida, Y. Nishikawa, M. Matsui, H. Matsumoto, T. Aoki, S. Nozaki, T. Takeda, Y. Tamori, A. Aiba, C. R. Kahn, T. Kataoka and T. Satoh (2010). "Crucial role of the small GTPase Rac1 in insulin-stimulated translocation of glucose transporter 4 to the mouse skeletal muscle sarcolemma." FASEB J **24**(7): 2254-61.

Ubellacker, J. M., A. Tasdogan, V. Ramesh, B. Shen, E. C. Mitchell, M. S. Martin-Sandoval, Z. Gu, M. L. McCormick, A. B. Durham, D. R. Spitz, Z. Zhao, T. P. Mathews and S. J. Morrison (2020). "Lymph protects metastasizing melanoma cells from ferroptosis." Nature **585**(7823): 113-118.

Valiente, M., A. C. Obenauf, X. Jin, Q. Chen, X. H. Zhang, D. J. Lee, J. E. Chaft, M. G. Kris, J . T. Huse, E. Brogi and J. Massagué (2014). "Serpins promote cancer cell survival and vascular co-option in brain metastasis." Cell **156**(5): 1002-16.

Valiente, M., A. E. D. Van Swearingen, C. K. Anders, A. Bairoch, A. Boire, P. D. Bos, D. M. Cittelly, N. Erez, G. B. Ferraro, D. Fukumura, B. Gril, M. Herlyn, S. L. Holmen, R. K. Jain, J. A. Joyce, M. Lorger, J. Massague, J. Neman, N. R. Sibson, P. S. Steeg, F. Thorsen, L. S. Young, D. Varešlija, A. Vultur, F. Weis-Garcia and F. Winkler (2020). "Brain Metastasis Cell Lines Panel: A Public Resource of Organotropic Cell Lines." Cancer Res **80**(20): 4314-4323.

Versluis, J. M., G. V. Long and C. U. Blank (2020). "Learning from clinical trials of neoadjuvant checkpoint blockade." Nat Med **26**(4): 475-484.

Villanueva, J., J. R. Infante, C. Krepler, P. Reyes-Uribe, M. Samanta, H. Y. Chen, B. Li, R. K. Swoboda, M. Wilson, A. Vultur, M. Fukunaba-Kalabis, B. Wubbenhorst, T. Y. Chen, Q. Liu, K. Sproesser, D. J. DeMarini, T. M. Gilmer, A. M. Martin, R. Marmorstein, D. C. Schultz, D. W. Speicher, G. C. Karakousis, W. Xu, R. K. Amaravadi, X. Xu, L. M. Schuchter, M. Herlyn and K. L. Nathanson (2013). "Concurrent MEK2 mutation and BRAF amplification confer resistance to BRAF and MEK inhibitors in melanoma." Cell Rep **4**(6): 1090-1099.

Villanueva, J., A. Vultur, J. T. Lee, R. Somasundaram, M. Fukunaga-Kalabis, A. K. Cipolla, B. Wubbenhorst, X. Xu, P. A. Gimotty, D. Kee, A. E. Santiago-Walker, R. Letrero, K. D'Andrea, A. Pushparajan, J. E. Hayden, K. D. Brown, S. Laquerre, G. A. McArthur, J. A. Sosman, K. L. Nathanson and M. Herlyn (2010). "Acquired resistance to BRAF inhibitors mediated by a RAF kinase switch in melanoma can be overcome by cotargeting MEK and IGF-1R/PI3K." Cancer Cell **18**(6): 683-695.

Vu, H. L., S. Rosenbaum, T. J. Purwin, M. A. Davies and A. E. Aplin (2015). "RAC1 P29S regulates PD-L1 expression in melanoma." Pigment Cell Melanoma Res **28**(5): 590-598.

Vultur, A., R. Buettner, C. Kowolik, W. Liang, D. Smith, F. Boschelli and R. Jove (2008). "SKI-606 (bosutinib), a novel Src kinase inhibitor, suppresses migration and invasion of human breast cancer cells." Mol Cancer Ther **7**(5): 1185-1194.

Vultur, A. and M. Herlyn (2013). "SnapShot: melanoma." Cancer Cell **23**(5): 706-706.e701.

Vultur, A., J. Villanueva, C. Krepler, G. Rajan, Q. Chen, M. Xiao, L. Li, P. A. Gimotty, M. Wilson, J. Hayden, F. Keeney, K. L. Nathanson and M. Herlyn (2014). "MEK inhibition affects STAT3 signaling and invasion in human melanoma cell lines." Oncogene **33**(14): 1850-1861.

Watson, I. R., L. Li, P. K. Cabeceiras, M. Mahdavi, T. Gutschner, G. Genovese, G. Wang, Z. Fang, J. M. Tepper, K. Stemke-Hale, K. Y. Tsai, M. A. Davies, G. B. Mills and L. Chin (2014). "The RAC1 P29S hotspot mutation in melanoma confers resistance to pharmacological inhibition of RAF." Cancer Res **74**(17): 4845-4852.

Watson, J. (2013). "Oxidants, antioxidants and the current incurability of metastatic cancers." Open Biol **3**(1): 120144.

Wehner, R., K. Dietze, M. Bachmann and M. Schmitz (2011). "The bidirectional crosstalk between human dendritic cells and natural killer cells." J Innate Immun **3**(3): 258-263.

Wertheimer, E., A. Gutierrez-Uzquiza, C. Rosemblit, C. Lopez-Haber, M. S. Sosa and M. G. Kazanietz (2012). "Rac signaling in breast cancer: a tale of GEFs and GAPs." Cell Signal **24**(2): 353-362.

Westphal, D., I. C. Glitza Oliva and H. Niessner (2017). "Molecular insights into melanoma brain metastases." Cancer **123**(S11): 2163-2175.

Wittgen, H. G. and L. C. van Kempen (2007). "Reactive oxygen species in melanoma and its therapeutic implications." Melanoma Res **17**(6): 400-409.

Wong, D. J. and A. Ribas (2016). "Targeted Therapy for Melanoma." Cancer Treat Res **167**: 251-62.

Wölfle, U., G. Seelinger, G. Bauer, M. C. Meinke, J. Lademann and C. M. Schempp (2014). "Reactive molecule species and antioxidative mechanisms in normal skin and skin aging." Skin Pharmacol Physiol **27**(6): 316-32.

Wright, S. C. E., N. Vasilevski, V. Serra, J. Rodon and P. J. A. Eichhorn (2021). "Mechanisms of Resistance to PI3K Inhibitors in Cancer: Adaptive Responses, Drug Tolerance and Cellular Plasticity." Cancers (Basel) **13**(7): 1538.

Xu, S., Feng, Y., and Zhao, S. (2019). "Proteins with Evolutionarily Hypervariable Domains are Associated with Immune Response and Better Survival of Basal-like Breast Cancer Patients." Comput Struct Biotechnol J **17**: 430–440.

Xu, T., W. Ding, X. Ji, X. Ao, Y. Liu, W. Yu and J. Wang (2019). "Molecular mechanisms of ferroptosis and its role in cancer therapy." J Cell Mol Med **23**(8): 4900-4912.

Yang, J., J. Nie, X. Ma, Y. Wei, Y. Peng and X. Wei (2019). "Targeting PI3K in cancer: mechanisms and advances in clinical trials." Mol Cancer **18**(1): 26.

Yang, W. S. and B. R. Stockwell (2008). "Synthetic lethal screening identifies compounds activating iron-dependent, nonapoptotic cell death in oncogenic-RAS-harboring cancer cells." Chem Biol **15**(3): 234-245.

Ye, Z., W. Liu, Q. Zhuo, Q. Hu, M. Liu, Q. Sun, Z. Zhang, G. Fan, W. Xu, S. Ji, X. Yu, Y. Qin and X. Xu (2020). "Ferroptosis: Final destination for cancer?" Cell Prolif **53**(3): e12761.

Zentrum für Krebsregisterdaten. https://www.krebsdaten.de.

Zhang, L., S. Zhang, J. Yao, F. J. Lowery, Q. Zhang, W. C. Huang, P. Li, M. Li, X. Wang, C. Zhang, H. Wang, K. Ellis, M. Cheerathodi, J. H. McCarty, D. Palmieri, J. Saunus, S. Lakhani, S. Huang, A. A. Sahin, K. D. Aldape, P. S. Steeg and D. Yu (2015). "Microenvironment-induced PTEN loss by exosomal microRNA primes brain metastasis outgrowth." Nature **527**(7576): 100-104.

Zhang, X., C. S. Gibhardt, T. Will, H. Stanisz, C. Körbel, M. Mitkovski, I. Stejerean, S. Cappello, D. Pacheu-Grau, J. Dudek, N. Tahbaz, L. Mina, T. Simmen, M. W. Laschke, M. D. Menger, M. P. Schön, V. Helms, B. A. Niemeyer, P. Rehling, A. Vultur and I. Bogeski (2019). "Redox signals at the ER-mitochondria interface control melanoma progression." Embo J **38**(15): e100871.

Zou, Y., A. Watters, N. Cheng, C. E. Perry, K. Xu, G. M. Alicea, J. L. D. Parris, E. Baraban, P. Ray, A. Nayak, X. Xu, M. Herlyn, M. E. Murphy, A. T. Weeraratna, Z. T. Schug and Q. Chen (2019). "Polyunsaturated Fatty Acids from Astrocytes Activate PPARγ Signaling in Cancer Cells to Promote Brain Metastasis." Cancer Discov **9**(12): 1720-1735.

APPENDICES

Supplemental Table 1. Full RPPA dataset. Normalized log2 median centered expression values are displayed for 297 RPPA targets in three non-MBM (1205Lu, WM3918, WM983B) and three MBM melanoma cell lines (M230, M331, M450). Three independent samples from each cell line were investigated.

Protein/ Cell line	*1205Lu*	*WM3918*	*WM983B*	*M230*	*M331*	*M450*
14-3-3-beta-R-V	0.66017	-0.16836	0.63754	-0.06009	0.04793	0.12611
14-3-3-epsilon-M-C	-0.25334	-0.24665	0.12584	-0.13175	0.20757	0.03027
14-3-3-zeta-R-V	0.29714	-0.12771	-0.00683	0.21024	-0.36176	0.08241
4E-BP1-R-V	-0.23813	0.33474	-0.18943	0.15430	-0.44902	-0.25165
4E-BP1_pS65-R-V	-0.00287	0.00287	0.03678	-0.52957	-0.62190	-0.49751
4E-BP1_pT37_T46-R-V	-0.26110	0.31861	0.04685	-0.15104	-0.77029	-0.46022
53BP1-R-V	0.12733	0.16643	-0.08157	-0.81820	-1.07264	-0.85485
A-Raf-R-V	0.10977	-0.03176	0.07243	0.03167	0.35319	-0.56424
ACC_pS79-R-V	0.49973	0.99793	-1.42199	-0.54129	-1.37180	-1.92546
ACC1-R-C	-0.07202	0.55760	-0.80867	-0.49856	-1.24906	-1.13266
ACVRL1-R-C	0.04874	-0.03984	0.05331	-0.20671	0.13803	-0.01673
ADAR1-M-V	-0.11830	-0.21923	-0.04634	0.21004	0.20580	0.11796
Akt-R-V	-0.13231	-0.55084	-0.19013	0.83090	-0.70854	-1.90587
Akt_pS473-R-V	1.30161	-0.22402	1.72082	0.60418	0.19322	0.06130
Akt_pT308-R-V	2.06650	-0.29679	2.41317	0.92587	0.14851	-0.04376
AMPKa-R-C	-0.08680	-0.29300	0.02938	-0.06612	-0.30341	-0.56019
AMPKa_pT172-R-C	0.80056	0.29692	-1.10789	0.28804	-0.32414	-0.31788
Annexin-I-M-V	-1.45517	1.16928	0.26721	1.04160	-0.00274	0.49673
Annexin-VII-M-V	-0.00905	-0.05427	0.12899	-0.07975	0.33539	0.55373
AR-R-V	-0.24151	-0.05176	-0.24248	0.43163	0.32900	0.42476
ARHI-M-C	-0.04956	-0.09048	-0.01398	0.04367	0.29608	0.14620
ARID1A-R-C	0.43073	0.32846	-0.43323	0.78977	0.13059	0.46716
Atg3-R-V	-0.12208	-0.01918	0.10649	-0.09462	0.07730	-0.05579
Atg7-R-V	0.52582	0.29307	-0.10221	-0.44841	-0.58940	-0.03591
ATM-R-V	-0.22373	0.05653	-0.21659	-0.72730	-1.23344	-0.73037
ATM_pS1981-R-V	-0.14482	0.01713	-0.07369	0.04658	-0.11355	0.11934
ATP5A-M-C	0.04472	-0.09251	-0.18176	0.06928	0.48668	0.10230
Aurora-B-R-V	0.25073	-0.25976	0.72683	-0.92215	-0.06947	-0.28973
Axl-R-V	1.81180	2.97796	0.59741	0.72583	1.81762	2.34648
b-Actin-R-C	0.14238	0.30725	0.27073	0.06137	0.06401	-0.22775
b-Catenin-R-V	-1.58756	0.05462	0.04931	-0.04560	-0.18862	1.14264
b-Catenin_pT41_S45-R-V	-0.07886	0.00754	0.18287	-0.10855	0.08332	0.26500
B-Raf-R-V	-0.37986	0.16119	-0.38890	0.01774	-0.10852	-0.15063
B-Raf_pS445-R-V	0.03872	-0.21946	-0.46405	-0.18976	-1.24176	-1.06426
B7-H3-R-C	-0.40770	0.58731	0.05153	0.23257	0.97028	1.14554
B7-H4-R-C	-0.21909	0.10052	0.36254	-0.03652	0.41032	0.05836
Bad_pS112-R-V	0.33152	-0.12700	-0.01852	0.38137	0.06013	-0.09744
Bak-R-C	0.04797	0.09571	-0.06099	0.03768	0.57031	0.21432
BAP1-M-V	0.12697	-0.00590	-0.06700	-0.05318	-0.09688	-0.63938

Bax-R-V	-0.12270	-0.37819	0.03930	-0.08996	-0.45762	-0.31471
Bcl-xL-R-V	-0.12249	-0.01544	-0.11102	-0.05148	0.05595	0.44048
Bcl2-M-V	-0.37669	0.04104	0.20229	-0.04924	0.51915	0.26161
Bcl2A1-R-V	-0.07352	0.00314	0.10025	-0.20167	0.22590	-0.07538
Beclin-G-C	1.09742	-0.30959	0.86809	-0.14787	0.28417	-0.02435
Bid-R-C	-0.16844	-0.04893	-0.22457	0.04080	-0.02054	-0.15804
Bim-R-V	-0.16528	0.00008	-0.05389	-0.36229	1.28258	1.05361
BRD4-R-V	-0.19245	0.15696	-0.46312	0.21759	0.43981	0.35101
c-Abl-R-V	0.01898	-0.13897	-0.16494	0.37082	0.27224	0.42192
c-Jun_pS73-R-V	0.11072	0.61042	-0.11198	0.84312	0.91334	0.45311
c-Kit-R-V	-0.19045	-0.38172	0.14075	0.03780	1.22326	-0.03313
c-Met-M-Q	-0.32132	-0.06088	0.02408	0.05729	0.14149	-0.14164
c-Met_pY1234_Y1235-R-V	0.01810	-0.13090	-0.08391	-0.02782	-0.09247	-0.06543
c-Myc-R-C	0.03441	0.34355	-0.20894	0.07732	0.11872	0.23323
C-Raf-R-C	0.07507	-0.26063	0.05457	-0.10924	-0.53281	-0.14745
C-Raf_pS338-R-V	-0.20745	-0.03548	-0.03499	0.10146	0.10554	0.09391
Caspase-3-R-C	-0.15416	-0.01258	-0.00935	-0.09366	0.02605	-0.06641
Caspase-7-cleaved-R-C	0.13067	-0.06379	0.10358	-0.15400	0.02071	-0.02577
Caspase-8-M-Q	-0.07743	-0.13957	-0.00283	0.02400	-0.16997	-0.11148
Caveolin-1-R-V	0.30120	1.62092	2.03267	1.99030	0.71655	1.56392
CD171-M-V	0.26037	1.71717	0.00716	-0.67744	2.90504	-0.52551
CD26-R-V	0.09104	-0.07374	-0.01474	0.24127	0.18931	0.26452
CD29-M-V	-0.01763	-0.05800	0.21925	0.16468	0.33966	0.16039
CD31-M-V	-0.14870	0.01769	0.28697	0.01755	0.35840	0.08806
CD44-M-C	0.77993	-0.01307	-0.18772	0.24249	0.46517	-0.00661
CD49b-M-V	-0.03487	0.03429	-0.02286	0.71040	0.51033	0.02592
CDK1-R-C	0.23183	0.58642	-0.10617	-1.19586	-1.03008	-0.50632
Chk1-M-C	0.52761	0.38203	0.08888	-1.01267	-0.72412	-0.39530
Chk1_pS296-R-V	0.26860	-0.03857	0.00350	-0.10396	-0.09449	-0.07936
Chk1_pS345-R-C	0.26927	-0.09321	0.09726	0.04463	-0.61441	-0.28816
Chk2-M-V	-0.34854	0.07995	0.06796	-0.93793	-0.35548	-0.61372
Chk2_pT68-R-C	-0.15761	0.23028	-0.19289	-0.11119	0.03800	-0.03495
Claudin-7-R-V	0.26390	-0.06859	0.26498	0.18840	0.48210	0.30889
COG3-R-V	0.00695	-0.26474	0.03848	-0.21746	-0.30073	-0.20949
Collagen-VI-R-V	0.01937	-0.12438	-0.03335	-0.10422	0.06766	-0.16328
CoMPlex-II-Subunit-M-V	-0.26334	0.04786	-0.23065	-0.15473	0.54300	-0.85691
Connexin-43-R-C	0.30590	0.16427	0.98675	-0.22276	0.04989	-0.29593
Coup-TFII-R-C	0.33122	0.06770	0.16972	-0.01740	-0.02964	-0.21754
Cox-IV-M-C	-0.10321	-0.10311	-0.09369	0.05916	0.26821	0.19658
Cox2-R-C	0.86368	-0.51867	0.59164	2.27226	1.16211	-0.32042
CXCR4-R-C	-0.16465	-0.15416	0.22102	0.18011	0.30273	0.21227
Cyclin-B1-R-V	0.01330	0.89333	-0.31501	-1.14072	-0.70308	0.04943
Cyclin-D1-R-V	-0.14356	-0.28891	0.61645	0.37682	0.24270	0.31513
Cyclin-E1-M-V	-0.08064	-0.25934	-0.11819	0.11276	0.26182	-0.20889
Cyclophilin-F-M-V	-0.62319	1.40216	-0.47672	-0.31411	0.90393	0.55900
D-a-Tubulin-R-V	-0.07149	-0.05791	-0.16062	0.35417	0.35332	0.25414

DJ1-R-V	-0.03370	0.33125	-0.57348	-0.23801	-0.38853	-0.33145
DM-Histone-H3-R-V	-0.02187	-0.16390	0.12635	0.05998	0.02046	-0.03333
DM-K9-Histone-H3-R-C	-0.07403	-0.08992	-0.08113	0.21420	0.05871	0.18609
DUSP4-R-V	-1.49002	-1.38745	0.00392	-0.09276	-1.10967	0.21226
Dvl3-R-V	-0.25208	-0.08027	-0.17784	-0.00988	-0.29984	0.32603
E-Cadherin-R-V	-0.15135	-0.42149	-0.04456	-0.02718	1.80645	1.30334
E2F1-M-V	-0.05350	0.06734	0.07393	0.34627	0.19333	0.25447
eEF2-R-C	0.19221	0.12252	-0.14437	0.05102	-0.85273	-0.18819
eEF2K-R-V	-0.20022	-0.05616	-0.35210	-0.29278	-0.86610	-0.69095
EGFR-R-V	1.87385	0.49461	2.12117	-0.03444	0.53640	1.10290
EGFR_pY1068-R-C	0.11829	0.48611	0.08595	-0.19163	0.11604	0.32420
EGFR_pY1173-R-V	-0.00585	-0.05983	-0.10309	0.17393	0.19827	0.22446
eIF4E-R-V	-0.43884	-0.01967	-0.08254	0.43931	-0.19427	0.14308
eIF4G-R-C	-0.18792	0.29959	-1.67406	0.53834	-0.75610	-0.13226
Elk1_pS383-R-C	0.16427	-0.15281	0.08780	0.44354	-0.03122	0.10114
EMA-M-C	-0.01425	-0.04671	0.06382	0.88627	0.63517	0.25106
ER-R-V	-0.15373	0.02144	-0.24625	-0.06849	0.37945	0.14085
ERCC1-M-V	0.03096	-0.11378	-0.07340	-0.63925	-0.08957	-0.11789
ERCC5-R-C	-0.39363	-0.12479	-0.21468	0.35213	-0.08964	0.00197
Ets-1-R-V	-0.02060	-0.01735	0.04272	-0.05636	0.06597	0.04684
FAK-R-C	0.44688	0.05451	-0.28511	0.57730	-0.08295	0.14632
FAK_pY397-R-V	1.04563	0.35267	-0.27334	-0.97153	-0.29170	-0.49033
FASN-R-V	-0.22936	0.92540	-0.50790	-0.46007	-0.49272	-0.85666
Fibronectin-R-V	-0.08169	-0.09133	-0.18022	1.06345	0.53258	1.16681
FoxM1-R-V	0.34561	0.76390	0.07271	-0.74667	-0.38212	0.03416
FoxO3a-R-C	0.00400	0.08986	0.07749	-0.07069	0.25642	0.03787
FoxO3a_pS318_S321-R-C	-0.00104	-0.09585	0.41238	0.09603	-0.04002	0.11033
FRA-1-R-C	0.04538	0.10960	0.14905	0.73709	-0.03513	0.35310
G6PD-M-V	0.01912	0.03936	-0.01085	-0.08553	0.15372	0.37243
Gab2-R-V	-2.23393	0.28517	-0.06249	0.15952	-0.87677	-0.60749
GAPDH-M-C	0.41329	0.30911	-0.17457	-0.04310	-0.69856	-0.29759
GATA3-M-V	-0.09783	0.03220	0.07970	-0.10183	0.35727	0.03070
GCN5L2-R-V	0.29636	0.34565	-0.41022	0.50691	0.66404	0.21034
Glutamate-D1-2-R-C	-0.30065	-0.07284	0.07630	-0.21183	-0.05418	0.32890
Glutaminase-R-C	-0.01299	-0.33490	-1.78220	0.00917	0.13189	-0.06585
GPBB-R-V	1.27536	1.36758	-1.20960	0.42918	-0.20466	-1.73829
GSK-3a-b-M-V	0.14148	-0.25409	-0.01892	-0.08353	-0.47138	-0.33798
GSK-3a-b_pS21_S9-R-V	0.52370	-0.60219	0.13572	0.02245	-0.44109	-0.79136
Gys-R-V	-0.28116	-0.58455	-0.41236	0.45288	-0.18270	-0.95763
Gys_pS641-R-V	-0.02602	-0.43554	-0.57171	0.68928	-0.43172	-0.09600
H2AX_pS140-M-C	0.02430	-0.01992	0.19350	-0.10084	0.07285	-0.03201
HER2-M-V	-0.02184	0.30274	0.22850	-0.12155	-0.00183	0.12790
HER2_pY1248-R-C	-0.11118	0.81652	0.24812	-0.34967	-0.33623	0.09098
HER3-R-V	-0.36013	-0.02178	-0.08584	0.25903	-0.01537	-0.74002
HER3_pY1289-R-C	-0.01714	0.06353	-0.00749	0.01792	-0.13153	0.02533
Heregulin-R-V	0.37626	-0.14210	0.23937	-0.08903	-0.02220	0.16170

HES1-R-V	0.29739	-0.12004	0.39582	0.20666	-0.09455	-0.08241
Hexokinase-II-R-V	0.20598	0.10417	0.03451	0.58358	0.18635	-0.28203
HIAP-R-C	0.05479	0.22526	-0.46619	0.07530	-0.00627	-0.07129
Hif-1-alpha-M-C	-0.14738	0.28202	0.51353	0.73476	0.02227	0.04494
Histone-H3-R-V	-0.07537	-0.14823	0.03009	-0.10980	-0.06884	0.23152
HSP27-M-C	-0.28655	-0.04251	-0.06715	0.14567	0.07910	-0.13102
HSP27_pS82-R-V	0.21381	0.30634	-0.66416	1.41198	-0.20162	-0.54869
HSP70-R-C	-0.28888	0.09349	0.06655	-0.05414	0.44721	0.22584
IGF1R_pY1135_Y1136-R-V	-0.05896	0.05902	-0.03077	0.14785	0.22627	0.24786
IGFBP2-R-V	1.86897	-1.26125	0.79816	-0.42580	-0.44893	-0.21117
IGFBP5-G-C	0.69251	-0.05898	0.69149	-0.31348	0.14140	0.13108
IGFRb-R-C	-0.35749	-0.39279	-1.36746	-0.03762	0.23154	-0.10509
INPP4b-R-V	-0.52961	-0.42120	0.06126	0.13687	-0.45597	-0.69986
IRF-1-R-C	0.51816	-0.11465	0.69339	0.02979	0.03125	0.38121
IRS1-R-V	0.17739	0.00260	-0.00260	-0.20323	-0.02080	0.20833
JAB1-M-C	0.20148	0.10561	0.13849	-0.12382	-0.01609	-0.01459
Jagged1-R-V	0.04620	-0.38174	-1.52585	-0.23619	0.24218	-0.13197
Jak2-R-V	-0.06492	-0.33888	-0.04713	0.03743	-0.19931	-0.08306
JNK_pT183_Y185-R-V	-0.09074	0.03958	-0.10043	0.11960	0.08590	0.08872
JNK2-R-C	0.08204	0.23323	-0.30771	-0.38474	0.01027	-0.67875
LC3A-B-R-C	-0.10859	0.31871	-0.12525	1.55439	0.57980	0.95668
Lck-R-V	-0.22652	-0.11934	-0.02185	-0.04657	0.29763	0.78076
LDHA-R-C	0.09487	0.34849	-0.12343	-0.00909	-0.30334	-0.54084
MAPK_pT202_Y204-R-V	0.40362	-1.17137	0.31846	0.98849	-0.88044	-0.09281
Mcl-1-R-V	0.15326	-0.20279	-0.21899	0.42599	0.16499	0.38754
MCT4-R-V	0.95243	0.34421	0.71345	-0.32608	0.08156	0.58801
MDM2_pS166-R-V	0.21367	-0.02366	0.34326	0.52339	0.31032	0.55825
MEK1-R-V	-0.33140	0.15527	0.03210	0.16311	-0.62610	-0.55691
MEK1_pS217_S221-R-V	0.59584	-0.46972	0.20300	0.21263	-0.48680	-0.38893
MEK2-R-V	-0.11436	-0.07696	0.09094	0.00187	-0.01411	-0.03849
Merlin-R-C	0.32033	0.11551	-0.32726	-0.20208	-0.24525	-0.20761
MIF-R-C	-0.31210	-0.02148	0.04787	-0.36499	0.03895	-0.32614
MIG6-M-V	0.57162	0.41624	-0.04820	-0.12936	0.14020	0.02215
Mitochondria-M-V	0.14031	0.15810	-0.23556	-0.14227	0.38473	0.57406
MMP2-R-V	-0.01137	-0.02902	-0.05115	0.14188	0.75092	0.43620
MSH2-M-V	-0.03057	0.11033	0.17822	-0.44036	0.18010	0.02546
MSH6-R-C	0.12891	0.18512	-0.75122	-1.03278	-0.72067	-0.25992
mTOR-R-V	-0.36178	0.08745	-0.25161	-0.15520	-0.34927	-0.05818
mTOR_pS2448-R-C	0.06944	-0.05352	-0.14390	-0.10250	0.09840	-0.21325
Myosin-11-R-V	-0.18107	0.08129	-0.02254	-0.37694	-0.39680	-0.32833
Myosin-IIa_pS1943-R-V	0.53140	-1.06661	-0.12276	-0.06276	-1.63997	-0.69204
N-Cadherin-R-V	-0.06560	0.12701	0.46897	0.35361	0.31193	0.24908
N-Ras-M-V	-0.09309	-0.14133	-0.08480	0.25612	0.26746	0.18722
NAPSIN-A-R-C	-0.24771	-0.10042	-0.22854	0.20013	0.07823	0.09684
NDRG1_pT346-R-V	2.79263	-3.59441	1.98227	1.43884	-0.88783	1.14311
NDUFB4-M-V	0.20477	0.00896	-0.04249	-0.13424	0.13487	-0.02139

NF-kB-p65_pS536-R-C	-0.33425	0.11497	0.02831	-1.34219	-1.10934	-1.17160
Notch1-R-V	-0.00423	0.12621	0.29692	1.32483	-0.31440	0.27133
Notch3-R-C	0.03180	0.10531	0.28534	-0.02178	0.36478	0.06113
P-Cadherin-R-C	-0.24195	-0.50707	0.11300	-0.42916	0.43821	-0.23969
p16INK4a-R-V	-0.80198	0.51678	0.20590	-0.83575	-0.06011	0.69511
p21-R-V	-0.14344	-0.46335	0.18884	0.22002	-0.31173	-0.56559
p27-Kip-1-R-V	-0.03802	-0.29471	0.01468	-0.19713	-0.11278	-0.28931
p27_pT157-R-C	0.22606	0.03516	0.12930	0.12845	0.11219	0.12765
p27_pT198-R-V	0.15323	-0.11416	0.07982	0.46297	0.11186	0.11452
p38-R-V	-0.33327	0.00452	-2.57749	-0.09272	-0.30334	-0.39279
p38_pT180_Y182-R-V	-0.07230	0.00704	0.00052	0.54553	0.60383	0.30518
p53-R-C	-0.21763	0.06964	0.09457	0.23543	0.65305	0.00161
p70-S6K_pT389-R-V	1.34661	0.08824	1.27351	-0.54959	-0.28429	-0.20399
p70-S6K1-R-V	-0.08398	0.50215	-0.13176	0.10669	-0.02546	-0.04131
p90RSK_pT573-R-C	0.62481	-0.42760	-0.07229	1.04151	-0.85429	-0.78786
PAI-1-M-V	1.00073	0.03526	-0.28117	0.03252	1.51118	1.93007
PAR-R-C	-0.41479	-0.24097	-0.06332	2.85760	3.06561	2.85203
PARP1-R-V	-0.06743	-0.04935	-0.79262	-1.15682	-0.65123	-0.51271
Paxillin-R-C	-0.05136	-0.41502	-0.07275	-0.19660	-0.50036	-0.70282
PCNA-M-C	-0.02458	0.43437	-0.24603	-0.36791	-0.27473	-0.27583
PD-L1-R-C	-0.07433	0.02303	0.14152	-0.14460	0.57128	0.14626
Pdcd-1L1-G-C	1.24976	-0.15910	1.35562	-0.03646	0.22364	-0.04942
Pdcd4-R-C	0.06455	0.04252	-0.08767	0.52614	-0.63357	-0.98848
PDGFR-b-R-V	2.21434	2.08114	-0.03871	-0.30603	0.20732	2.47056
PDGFR-b_pY579-R-N	-0.26783	-0.14625	-0.17009	0.07625	0.07539	-0.00701
PDGFR-b_pY751-R-N	-0.01002	-0.03576	-0.04366	-0.21290	-0.07107	0.01563
PDGFR-b_pY857-R-N	-0.21361	-0.10396	-0.17179	-0.29861	-0.13043	0.24289
PDGRF-b_pY1009-R-N	0.17111	0.05186	0.38000	-0.17603	-0.00021	0.01072
PDGRF-b_pY1021-R-N	-0.20245	-0.20940	-0.23995	-0.23057	-0.11571	0.10889
PDGRF-b_pY716-R-N	-0.23373	-0.26683	-0.13507	-0.14650	-0.22124	0.13224
PDGRF-b_pY740-R-N	-0.13551	0.01007	-0.10056	-0.00027	0.01617	0.41437
PDGRF-b_pY771-R-N	-0.22867	0.05352	-0.19820	-0.12623	-0.06778	0.12730
PDK1-R-V	0.13245	-0.27595	0.52196	0.31500	0.06976	0.06078
PDK1_pS241-R-V	0.08822	-0.40468	-0.04038	0.22246	-0.45768	-0.44945
PEA-15-R-V	0.18962	-0.11734	0.22261	0.68266	-0.66848	-0.20608
PEA-15_pS116-R-V	0.22251	-0.08157	0.09880	0.10984	0.24919	0.09872
PI3K-p110-a-R-C	-0.01093	0.04019	-0.09192	-0.38578	0.79635	-0.47823
PI3K-p110-b-M-C	-0.13947	-0.09473	0.09286	-0.08205	0.25503	0.03311
PI3K-p85-R-V	-0.55668	0.05922	-0.45180	-0.33761	-0.12236	-0.28874
PKA-a-R-V	0.03657	-0.45012	-0.84976	0.37458	-0.71883	-0.33711
PKC-a-M-V	0.45459	0.76550	-0.04162	-0.05726	-0.14063	0.63605
PKC-a_pS657-R-C	0.45797	0.95487	0.04330	-0.04719	0.35050	0.55229
PKC-b-II_pS660-R-V	0.22693	-0.06445	0.11407	0.50875	-1.16977	-0.39853
PKC-delta_pS664-R-V	0.15550	0.10884	0.29937	-0.40036	-0.04611	0.01487
PKM2-R-C	-0.54280	-0.01933	0.02907	0.26012	-0.30161	0.57524
PLC-gamma2_pY759-R-C	-0.12318	-0.04625	-0.04494	0.11923	0.21118	0.14692

PLK1-R-C	0.59025	0.46154	-0.14424	-1.04147	-0.73202	0.33506
PMS2-R-V	0.04629	0.38332	-0.29572	-0.70361	-0.13873	-0.27775
Porin-M-V	-0.13087	0.07422	-0.07989	0.05627	0.00023	-0.12586
PR-R-V	-0.18666	-0.01312	0.08320	0.06988	0.45008	0.20864
PRAS40-M-C	0.23935	0.20086	0.03505	0.15495	-0.22162	0.08506
PRAS40_pT246-R-V	0.41773	-0.41572	0.19644	0.18846	-0.10122	0.07762
PREX1-R-V	0.80009	0.75715	0.35423	-0.47789	-0.85448	-1.08902
PTEN-R-V	-2.60758	0.27391	-2.42639	-2.38274	-0.08155	-0.31748
Puma-R-C	1.03143	-0.13982	0.86853	-0.55229	1.33897	-0.37531
PYGM-M-C	0.52243	0.52881	-0.08741	0.10270	0.04148	-0.05717
Rab11-R-E	1.42760	-0.27708	1.56221	0.23988	0.28696	0.13703
Rab25-R-V	0.53836	-0.11767	1.45352	0.57713	0.21607	0.03518
Rad50-M-V	0.10110	0.33576	-0.14398	-0.01653	0.47279	0.11815
Rad51-R-V	-0.08471	0.07975	0.21988	0.08501	0.33295	-0.05328
Raptor-R-V	-0.26911	0.11207	-0.24111	-0.29953	-0.46262	-0.00177
Rb-M-Q	-0.00631	0.03445	-0.00431	0.00210	-0.03513	0.05312
Rb_pS807_S811-R-V	0.53063	0.48168	0.25965	-0.70374	-0.53375	-0.00504
RBM15-R-V	-0.13500	0.23957	-0.48085	1.03650	1.25922	0.87437
Rheb-M-C	-0.06418	-0.09100	0.00142	-0.27472	-0.18566	-0.15926
Rictor-R-C	-0.31547	0.45073	0.04018	-0.06302	-0.86861	-0.40500
Rictor_pT1135-R-V	0.65223	0.31459	0.37267	-0.27953	-0.64599	-0.63247
Rock-1-R-C	0.02636	-0.32242	0.11086	0.12753	-0.41576	-0.14331
RPA32-T-C	0.07145	0.09411	0.00862	-0.47110	-0.24015	-0.53559
RPA32_pS4_S8-R-C	0.14148	0.21208	0.06319	0.00596	-0.48862	-0.08476
RSK-R-C	0.16367	0.47772	-0.21592	-0.52713	-0.59504	-0.78718
S6_pS235_S236-R-V	0.83907	0.26216	0.08570	0.78315	-0.30987	0.53497
S6_pS240_S244-R-V	0.54454	0.27252	0.16188	0.54231	-0.42727	0.59997
SCD-M-V	0.12668	-0.11825	0.30009	0.04398	-0.03132	0.79852
SDHA-R-V	-0.43240	0.07137	-0.35065	-0.19921	0.49676	-0.36173
SF2-M-V	-0.41038	-0.11887	0.00456	-0.16501	0.03781	-0.11069
Shc_pY317-R-V	0.15975	-0.20078	0.13745	0.30883	-0.37656	-0.00227
SHP-2_pY542-R-C	0.15881	0.01482	-0.07663	-0.58702	-0.29303	0.00590
SLC1A5-R-C	-0.26892	0.55103	-0.75511	0.07847	-0.21839	2.57365
Smac-M-Q	-0.47797	-0.26638	-0.09082	-0.03227	0.75147	0.45199
Smad1-R-V	-0.12156	-0.07624	-0.29854	0.35205	0.07352	0.05110
Smad3-R-V	0.06366	0.18132	-0.23878	0.26922	0.01358	0.13629
Smad4-M-V	-0.03566	0.17034	0.02500	-0.09854	-0.01204	-0.06404
Snail-M-Q	0.31625	0.25223	0.10695	0.02352	0.03230	-0.00638
SOD2-R-V	-0.57593	0.30864	-2.22029	-0.26560	1.59251	0.48950
Sox2-R-V	0.20493	0.56938	0.53622	0.29092	0.48935	0.55795
Src-M-V	-0.45327	0.04754	0.06806	0.40944	0.20234	0.47874
Src_pY416-R-V	-0.25865	0.02391	0.14321	0.19051	-0.33757	-0.18510
Src_pY527-R-V	-1.10404	0.12038	-0.11572	0.29669	-0.22593	-0.08635
Stat3-R-C	-0.41191	-0.53198	-0.61382	-0.45596	-0.30821	-1.65882
Stat3_pY705-R-V	0.23275	-0.21358	-0.19719	-0.08498	0.38799	0.01857
Stat5a-R-V	-1.95166	-1.69331	0.04749	-0.72614	-0.52010	-0.77886

Stathmin-1-R-V	-0.03464	-0.11717	-0.01245	-0.10391	0.03861	0.10412
Syk-M-V	0.04163	-0.20724	0.18463	-0.28349	0.30834	0.80203
Tau-M-C	-0.15059	-0.24147	-0.08651	0.00096	-0.01566	-0.09534
TAZ-R-V	1.37874	0.06230	0.59663	0.29289	0.30118	0.38311
TFAM-R-V	0.00621	-0.08662	-0.29920	0.20679	1.46345	1.26455
TFRC-R-V	0.21769	0.47059	-0.06324	3.04158	3.64515	3.11273
TIGAR-R-V	-0.06341	-0.25231	0.07704	-0.12317	-0.36771	-0.27424
Transglutaminase-M-V	0.54804	0.07367	0.07065	0.06908	-0.07647	0.08169
TSC1-R-C	0.36136	-0.31348	0.55313	0.23994	-0.03358	-0.26794
Tuberin-R-V	-0.17881	-0.35159	-0.25185	0.06717	-1.03221	-0.14565
Tuberin_pT1462-R-V	0.30853	-0.38661	0.51833	-0.51955	-0.35219	-0.47973
TWIST-M-C	-0.11276	0.01054	0.05161	0.06979	0.14545	0.06165
Tyro3-R-V	0.04942	-0.24311	0.36443	0.39748	-0.17223	0.51665
UBAC1-R-V	-0.16153	0.01140	-0.15837	-0.06265	-0.24289	-0.15538
Ubq-Histone-H2B-M-C	-0.06018	0.05809	0.02863	0.01056	0.28744	0.03346
UGT1A-M-V	-0.07777	-0.12853	-0.01072	0.04375	0.34322	0.08842
VEGFR-2-R-V	0.12339	0.60403	0.26621	0.33572	0.06044	0.42109
VHL-M-E	0.02235	-0.17774	0.07887	0.18297	0.15450	-0.03143
Vimentin-M-C	0.10742	0.11841	-1.73401	0.01994	0.30634	-0.07421
XBP1-G-C	1.56467	-0.15795	1.47229	-0.22191	0.10396	-0.04578
XIAP-R-C	0.74504	-0.09593	0.57230	-0.29858	-0.32836	-0.21390
XPA-M-V	0.18542	0.50889	-0.57215	-0.69122	0.02742	0.12392
XPF-M-C	-0.04805	-0.16396	-0.17849	-0.03363	0.14176	-0.10012
XRCC1-R-C	0.42804	-0.12528	0.06326	-0.35099	-0.15393	0.20425
YAP-R-E	-0.18397	-0.35689	0.06035	0.41862	0.01318	0.14307
YAP_pS127-R-E	0.40306	-0.58499	0.24895	0.79300	-0.73513	-0.70507
YB1-R-V	0.20303	-0.26205	-1.49077	1.42438	-0.47884	0.23076
YB1_pS102-R-V	0.32304	-0.09753	-0.08797	0.93453	-0.04222	0.21063

Supplemental Table 2. Summary of p-values and their indication throughout the presented figures.

Cellular process	Significance	Corresponding figure
Proliferation	***	Figure 31 A
Adhesion	***	Figure 31 B
Migration	*	Figure 31 C
Invasion in Matrigel™	*	Figure 31 D
Invasion in collagen I	ns	Figure 31 E ii

Statistical significance: (*) $p < 0.05$; (**) $p < 0.01$; (***) $p < 0.001$; (ns) not significant.

Acknowledgements

First, I would like to thank Prof. Dr. Ivan Bogeski and Adina Vultur, Ph.D. for giving me the opportunity to carry out my Ph.D. in a friendly and hard-working research group.

I wish to show my gratitude to Manuela Banciu, Ph.D. for convincing me to apply for a Ph.D. position abroad and for her support during the application process.

I am deeply grateful to Prof. Dr. Ivan Bogeski for the valuable scientific advice, support and trust throughout my Ph.D. period. I would not be where I am today without his help.

I would like to express my deepest appreciation to my mentor Adina Vultur, Ph.D. for instructing me at the very beginning of my Ph.D., for starting, driving and believing in this project, for her friendship and her valuable advice.

I am indebt to Meenhard Herlyn, D.V.M., D.Sc. for supporting this project and to Prof. Dr. Blanche Schwappach for allowing unlimited access to the Odyssey® CLx imaging system.

I would like to pay my special regards to my thesis committee members Prof. Dr. Dieter Kube and Prof. Dr. Jörg Wilting for their guidance which helped my project move forward. Moreover, I am grateful to Prof. Dr. Frauke Alves, Prof. Dr. Volker Ellenrieder and Prof. Dr. Michael Schön, who kindly agreed to be part of my examination board.

I would particularly like to thank my colleague Zuriñe Bonilla Del Río for her helpful scientific advice but mostly for her invaluable friendship and emotional support throughout these years. I would like to express my gratitude to all my fellow lab colleagues for their expert assistance, friendship and support during my Ph.D. time, especially to Andrea Paluschkiwitz, Dr. Sabrina Cappello, Dr. Christine Gibhardt and Christian Ickes.

My deepest heartfelt appreciation goes to my family for their unconditional love and support. A very special thanks to my late grandparents who always supported my education. I miss you deeply and I wish you could be here with me in this important career milestone in my life. Many thanks to my parents for always believing in me and for their emotional support throughout my Ph.D. time. I would like to express my deepest appreciation to my husband Bogdan for moving to Germany with me so that I can pursue my dream and for always being there for me; you are my rock! There are not enough words to express my love and appreciation for you all. *Vă iubesc enorm!*

Special thanks to all my friends for their emotional support throughout my Ph.D. time.

I am deeply grateful to the Krämer family for all the help provided at the beginning of my doctoral studies.

And last but not least, I wish to thank all the people who are not listed here whose assistance was a milestone in the completion of this project.